https://lib.uliege.be https://matheo.uliege.be

Master thesis and internship[BR]- Master's thesis : Opto-mechanical design of a four apertures nulling interferometer[BR]- Integration internship

Auteur : Carboni, Claudia
Promoteur(s) : Clermont, Lionel; Dandumont, Colin
Faculté : Faculté des Sciences appliquées
Diplôme : Master en ingénieur civil en aérospatiale, à finalité spécialisée en "aerospace engineering"
Année académique : 2024-2025
URI/URL : http://hdl.handle.net/2268.2/23199

Avertissement à l'attention des usagers :

Tous les documents placés en accès ouvert sur le site le site MatheO sont protégés par le droit d'auteur. Conformément aux principes énoncés par la "Budapest Open Access Initiative"(BOAI, 2002), l'utilisateur du site peut lire, télécharger, copier, transmettre, imprimer, chercher ou faire un lien vers le texte intégral de ces documents, les disséquer pour les indexer, s'en servir de données pour un logiciel, ou s'en servir à toute autre fin légale (ou prévue par la réglementation relative au droit d'auteur). Toute utilisation du document à des fins commerciales est strictement interdite.

Par ailleurs, l'utilisateur s'engage à respecter les droits moraux de l'auteur, principalement le droit à l'intégrité de l'oeuvre et le droit de paternité et ce dans toute utilisation que l'utilisateur entreprend. Ainsi, à titre d'exemple, lorsqu'il reproduira un document par extrait ou dans son intégralité, l'utilisateur citera de manière complète les sources telles que mentionnées ci-dessus. Toute utilisation non explicitement autorisée ci-avant (telle que par exemple, la modification du document ou son résumé) nécessite l'autorisation préalable et expresse des auteurs ou de leurs ayants droit.

University of Liège - School of Engineering and Computer Science

Opto-mechanical design of a four apertures nulling interferometer

---

Master's thesis in order to obtain the degree of Master of Science
in Aerospace Engineering by Carboni Claudia

Supervisor:
Dr. Lionel Clermont

Co-supervisor:
Colin Dandumont

Author:
Claudia Carboni

Academic year: 2024 - 2025

Acknowledgments

I would like to thank the supervisor of this Master's thesis, Dr. Lionel Clermont, who has been a fundamental guide throughout this journey. His expertise contributed in a significant way to every step of this work. I also wish to thank the co-supervisor, Colin Dandumont, for his valuable advice and insightful suggestions. It has been both a pleasure and an honour to work at the Centre Spatial de Liège, in such a stimulating and enriching environment.

A very special thanks to my family, for giving me the possibility, without any hesitation, to pursue my dreams. To my mother, my anchor, my safe harbour, and so much more, who has always believed in me, even when I did not. To my father, who passed on to me his passion for mathematics and physics, and his never-ending curiosity for the unknown. To my brother, another engineer in the family, who offered his advice and is always there to make me laugh.

Last but not least I would like to thank my friends, my second family, who have supported me and have listened to me, even in the most difficult moments.

Contents

Introduction

Exoplanets, form Ancient Greek *exo*, meaning outside, extrasolar, are by definition planets located outside our Solar System. Interest in exoplanet detection has grown significantly in recent decades, driven by the potential to gain insights into planetary system formation and, ultimately, the conditions for life beyond Earth. Furthermore, the existence of exoplanet has proven the theory that planetary formation in strictly related to star formation, therefore being a common by-product of the star creation itself. This growing interest is further motivated by the prospect of identifying habitable zones and biosignatures on distant worlds.

The first confirmed detection of an exoplanet orbiting a main-sequence star occurred in 1995, with the discovery of 51 Pegasi b by Mayor and Queloz. The planet was discovered performing radial velocity measurements over one year and is characterized by a mass greater than or equal to 0.46 Jupiter masses, it orbits at a distance of 0.05 AU, therefore having a significant high surface temperature (1400 K) and has a orbital period of 4.2 days[62],[44]. This characteristics, which are different from the planets present in our Solar System, are similar to most of the exoplanets discovered so far.

The main challenge related to exoplanet detection is linked to the large brightness contrast between the star and its planet and also the restricted angular separation between them. A brief discussion on the existing techniques used to detect exoplanets is presented. Detection techniques can be broadly categorized into indirect and direct methods. Indirect techniques infer the presence of a planet by observing its influence on the host star, while direct methods attempt to detect the planet itself.

Indirect techniques

Astrometry consists of measuring the position and changes of position of objects in the sky and it was used to make the first detection of a star's unseen companion Sirius B[44]. It is the most ancient method used to search extrasolar planets. Astrometry is very sensitive and provides an accurate estimate of a planet's mass[74]. However, it requires a precision that is very difficult to achieve and it is most effective for large mass planets orbiting at some distance from their parent star[59].

The Transit method is the most efficient method implemented so far. This indirect method uses the fact that the light from the host star is attenuated by the transit of a planet across its disk. A minimum of 3 transits, separated by the same time interval, is required in order to confirm the detection of an exoplanet and discard the possibility of a false positive. The main advantages of this method are related to its simplicity, requiring small telescopes and not complex equipment, nonetheless providing several information such as the orbital period, the size of the planet and the size of the orbit. While, the disadvantages are mainly related to the fact that the planet has to be large enough (typically Jupiter's size) to produce a detectable drop of intensity of the starlight when transiting and also a precise alignment is needed[59].

In the context of Radial Velocity methods, one of the most effective indirect techniques is the Doppler method. This approach involves analysing the periodic variations in a star's radial velocity, corresponding to the component of its motion along our line of sight, by measuring shifts in the star's spectral lines due to the Doppler effect. As an orbiting planet exerts a gravitational pull on its host star, it causes the star to move in a small orbit or wobble. These motions produce detectable changes in the wavelength of the star's light: a blueshift as the star moves toward the observer, and a redshift as it moves away. By studying these periodic spectral shifts, astronomers can infer the presence of an exoplanet, estimate its minimum mass, and determine aspects of its orbital characteristics. It is a very precise method which reaches accuracies in Doppler shift measurements of a few meters-per-second[44]. The main disadvantage is again related to the size of the detectable exoplanet, which has to be massive enough to cause variations in the radial velocity of the star. Furthermore, this method needs the observer to be as close as possible to the orbital plane in order to observe a Doppler shift.

Gravitational microlensing is another indirect technique to detect exoplanets. It is based on the concept of general relativity, which states that the presence of matter distort spacetime consequently deflecting the path of the electromagnetic radiation. Under certain alignment conditions, light from a distant star is bent and focused by gravity when a planet transit between the star and the Earth. The advantages of this method are its sensibility to low mass planets and the ability to detect planets ejected from the gravitational potential of their parent star or planet orbiting an unseen star. The limitation of gravitational microlensing are instead linked to the very low probability of having the needed precise alignment between observer-host star-background[59].

Direct techniques

Direct Imaging is directly related to the measurement of the light from the exoplanet itself. In particular, various techniques are being implemented to image exoplanets at the highest angular resolution and contrast: coronography and nulling interferometry are two examples. The aim of the two instruments is to reduce light from the host star. A coronagraph is an instrument placed inside a telescope that uses a mask or an optical device to block the star's bright central light. While, nulling interferometry combines light from two or more telescopes (or beams within a single telescope) in such a way that the light from the central star interferes destructively, effectively cancelling it out. Meanwhile, light from nearby sources at slightly different angles does not get cancelled and can be detected[69]. Direct imaging allows for the most complete characterisation of the photosphere of the sub-stellar companions, making the resolved exoplanet available for spectroscopic observation[69].

Table 1 summarises the described exoplanet detection techniques and the associated number of exoplanet detected so far. Figure 2 shows the exoplanet census based on the latest data from the NASA's Exoplanet Archive for planets with both measured or estimated orbital period and mass[48].

Among the numerous techniques for detecting and characterizing extrasolar planets, it is important to highlight that only gravitational lensing, the occultation method, and space interferometry can identify Earth-like planets. However, space interferometry can also provide a spectrum of their atmosphere[61].

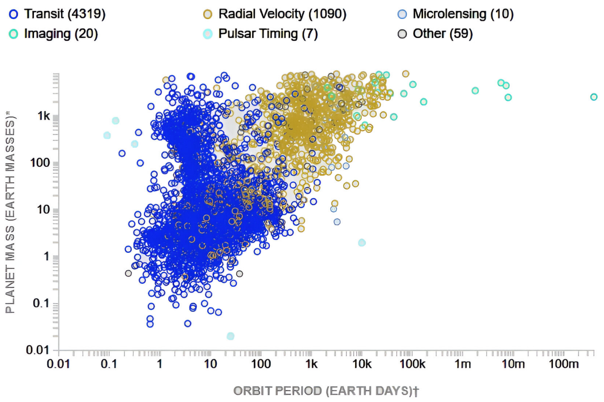

Figure 2: Exoplanet census for planets with both measured or estimated orbital period and mass[48].

Method	Discovered exoplanets
Transit	74.5 %
Radial Velocity	18.9 %
Microlensing	4.0 %
Direct Imaging	1.4 %

Table 1: Percentage of exoplanets discovered by method[48].

Relevance of nulling interferometry and project linkage

Nulling interferometry is a powerful observational technique with the potential to suppress starlight and enable the direct detection of faint exoplanets in close angular proximity to their host stars. It plays a central role in future space-based missions aimed at the detailed characterization of Earth-like exoplanets. In this context, the design work presented in this thesis is closely linked to ongoing research and development activities supported by the European Space Agency (ESA), and contributes to the broader technical groundwork for a future ESA mission[7] based on nulling interferometry for exoplanet detection and characterization.

It is also important to highlight that this thesis builds upon the prior work of L. Viseur[57] who initiated the development of a performance modelling tool for nulling interferometry. While the latter focused primarily on the theoretical and numerical modelling aspects of a two apertures nulling interferometer, the present study extends the effort by addressing the opto-mechanical design of a four apertures nulling interferometer.

Objectives and structure

The primary objective of this Master's thesis is to investigate and develop the opto-mechanical design of a four-aperture nulling interferometer intended for the detection of exoplanets. Nulling interferometry presents both significant scientific promise and substantial engineering challenges and this research aims to address these challenges through a multidisciplinary approach that combines optical modeling, mechanical design, and performance evaluation.

The optical design is carried out using CODE V, a ray-tracing and optimization tool widely used in industry and academia. It is employed to analyse and simulate the behaviour of the optical system, particularly under ideal and perturbed conditions. The mechanical aspects of the system are developed in Siemens NX, focusing on structural configuration, mass estimation, and tolerance analysis. Meanwhile, MATLAB is utilised for statistical evaluations, performance metrics, and to support optimization routines through custom scripts.

The thesis is structured to reflect the progression from theoretical foundations to applied design and validation. Chapter 1 provides an extensive review of nulling interferometry, with particular attention to its historical development, current applications, and future potential. It contextualizes the method within the broader landscape of exoplanet detection and presents a comparative analysis with other techniques, such as coronagraphy.

Chapter 2 delves into the theoretical considerations regarding the optical design of nulling interferometers. It outlines the main components of the system, such as beam collectors, transport optics, delay lines, and beam combiners, and introduces the mathematical framework used to describe optical path differences, phase variations, and intensity response. The limitations of the instrument are also discussed, offering insight into the trade-offs inherent in its design.

Chapter 3 is dedicated to the practical development of the optical system. It begins by defining the design methodology and sizing parameters, followed by validation of the approach through the simulation of a simple lens system. This validated approach is then applied to a single interferometer arm, allowing for a detailed investigation of beam control and phase requirements. An optical delay line is incorporated into the design to compensate for differential path lengths, a critical requirement in maintaining constructive and destructive interference across the instrument's field of view.

Chapter 4 focuses on the mechanical aspects of the interferometer. It begins by establishing the requirements and objectives that guide the mechanical configuration, such as structural stability, weight constraints, and deployability. The complete interferometer is modelled in two configurations: a telescopic setup and a foldable secondary mirror. Mass estimation is then performed to assess feasibility for potential space-based implementations. The mechanical design allows for a detailed tolerance analysis, which identifies the need for a compensator to maintain optical alignment. A survey of actuator technologies is also included, with emphasis on high-precision systems suitable for space applications.

Finally, Chapter 5 evaluates the performance of the complete system, particularly under perturbed conditions that simulate realistic operational challenges. Two compensator strategies are implemented in CODE V: one based on the bisection method and another using optimisation commands. Their effectiveness is assessed through the analysis of interferograms and transmission maps. Additionally, the chapter presents a statistical estimation of the exoplanet yield achievable by the system. Furthermore, comparative analysis of different interferometric array configurations is conducted to determine their robustness against errors.

Collaborative framework

The first and final chapters of this Master's thesis were co-authored with F. De Bortoli. Two distinct yet complementary approaches to nulling interferometry were developed. The present thesis focuses on an opto-mechanical analysis, while De Bortoli's thesis presents the development of an advanced modelling tool for a four-aperture nulling interferometer.

A shared foundation of general knowledge on the topic is provided in the first chapter to support both lines of analysis, introducing the context of nulling interferometry in the search for exoplanets.

After the development of the two approaches, the final chapter reunites the two paths. Here, the objective is to integrate the results of the optical design analysis with the numerical model, in order to assess the validity of the proposed designs and evaluate the impact of the compensator on system performance.

Chapter 1

Review of nulling interferometry for exoplanet detection: between past and future

Note:

This chapter has been co-authored with Francesco De Bortoli with the aim of introducing the context of nulling interferometry for exoplanet detection and providing a shared foundation of general knowledge to support the development of the two analyses.

Abstract: Detecting and characterising extrasolar planets is one of the most challenging and exciting frontiers in astronomy. Among the various techniques available, nulling interferometry stands alone in its ability to directly identify Earth-like exoplanets and analyse their atmospheric composition. This paper begins by exploring the fundamental principles of nulling interferometry and its unparalleled advantages, particularly in isolating an exoplanet's spectral signature while suppressing the light glare of its host star. The study then transitions to a comprehensive overview of ground-based interferometers, followed by a comparative analysis of modern optical/infrared interferometers sets the stage for future innovations. However, the fundamental limitations of ground-based observatories—primarily atmospheric absorption and scintillation—highlight the inevitable shift toward space-based solutions. The second part of this paper delves into the evolution of space-based interferometry, tracing its roots from Bracewell's original concept to refined mission proposals by ESA and NASA. Ultimately, the promising potential of nulling interferometry in exoplanet research is highlighted. As technological advancements continue to bring ambitious space-based concepts closer to reality, a new era of exoplanet discovery may be on the horizon—one that could finally unveil the atmospheres of distant Earth-like worlds.

1.1 Introduction

One of the major milestones in scientific research was reached in 1995 with the discovery of the first exoplanet around a main sequence star by Mayor and Queloz, using an indirect method (the radial velocity method)[22]. Since then, new scientific horizons have gained momentum in trying to answer the next obvious question: is there life outside Earth?

Nowadays, we are still awaiting answers, but besides philosophical considerations that have accompanied mankind throughout its history, technological progress could possibly aid us in this research: in effect, in recent years, missions like Kepler have significantly increased the number of detected exoplanets through the use of indirect methods.

However, simple detection is not enough, and the optical limitations of single apertures greatly reduce the amount of data that can be extracted from smaller exoplanets: while coronagraphy can be employed to image hotter, bigger, more distant (to their host star) exoplanets, the ones that could theoretically harbour life are outside the achievable angular resolution limits. Given the novelty of the topic, as well as the complexity of the matter, at the moment, almost nothing can be said about such planets: how they look like, what features do they present and so on are all open questions. Luckily, the potential of interferometry could change that, thanks to the simulated aperture and the nulling achievable to reduce the star's influence on the data. This work aims to provide a state-of-the-art overview of its current development.

After a brief introduction to the physics behind nulling interferometry, considerations on why this technique is complementary to single-aperture telescopes and motivations on why the mid-infrared region is preferred for research are presented. Ground-based and space-based interferometers of interest are then introduced, along with some considerations on their implementation and development processes. It must be highlighted that, while ground-based interferometry is today a valid instrument (albeit still in development), besides the problematic presence of the atmosphere, none of the studied space-based ones has ever reached a development phase due to the not-yet-mature technologies involved.

The flow of time, however, has brought advancements in the readiness levels of the involved instruments[12],[9]. While important challenges are still considered significant roadblocks in the development of future missions, it is probable that, in the coming years, the full potential of this technology will be realized.

1.2 Advantages of nulling interferometers

Rayleigh's criterion introduces a limitation on a telescope's ability to resolve two closely separated objects. In fact, two objects are distinguished if their angular separation is larger than:

$$\Delta\vartheta \geqslant 1.22\frac{\lambda}{D} \tag{1.1}$$

where λ is the wavelength and D is the diameter of the telescope. This specific value corresponds to the radius of the Airy disc: in order to be resolved, the images of two point sources, being Airy discs, must be such that the centre of one of them is located at the minimum of the other[33].

The linearity (at least to some extent: non-linear optics does not apply to traditional sources, whose flux densities are not high enough to produce a significant non-linear effect[33]) of the fields that constitute light allows for the existence of the superposition principle of the wave nature of light. This principle states that, given two separate waves at the same place, the resulting wave is simply given by the algebraic sum of the two original waves[33], leading to the possibility of interference.

Interference is, in fact, the key factor in the interferometry process, as the two waves can produce both in-phase and out-of-phase interference, meaning they can be reinforced or annihilated, producing visual effects known as fringes.

The principle of nulling interferometry is to combine the light received by a pair (or more) of telescopes in such a way that, when the optical path difference (OPD) between the incoming beams is zero, an achromatic phase shift is applied to create the phase opposition in the line-of-sight of the interferometer and suppress the starlight. However, off-axis sources positioned near constructive fringe maxima can still pass through the system. As a result, while the star is strongly suppressed, planets in favourable locations remain largely unaffected. The key challenge is to design an optical setup that can effectively null starlight across all polarizations and wavelengths within the desired passband[51].

Therefore, in order to detect exoplanets two main problems, among others, have to be solved: the high contrast which require a broad dynamic range and the need for a high angular resolution.

It is assumed that the general angular separation between an Earth-like exoplanet and its star would be below 100 mas[76] and, for example, in the case of Proxima b, being the closest exoplanet, the angular separation is around 37 mas[56]. This requirement is particularly stringent, meaning that currently existing telescopes, as illustrated in Table 1.1, are not able to meet it. Additionally, it is clear that, to reach a sufficient diameter, like that of future telescopes meeting these requirements, the payload size would vastly exceed the fairing of current-generation launchers.

Names	**D [m]**	**λ [µm]**	**R. [mas]**
Spitzer[79]	0.85	3.57	1057
HSO[70]	3.28	363	27850
JWST[29]	6.6	5.6	213.52
GMT[6]	25.4	0.32-25†	2.5937
TMT[66]	30	0.31-28†	2.1314
ELT[24]	39	3-5†	15.866

Table 1.1: Survey of the limit resolutions (R.) for different single-aperture infrared telescopes from their parameters: the diameter and the wavelength. The first three entries are existing telescopes, the remaining ones future ones. †When an interval was provided, the best (smallest) value has been taken.

As explained in Section 1.4, however, ground-based instruments are not a viable solution, as they would not be able to offer full-spectrum observations due to absorption windows. Alternative solutions are therefore needed in the domain of interferometry.

Similarly to how Equation 1.1 has been derived—i.e., by looking at the minimum of the Bessel function describing the Airy disc or the diffraction pattern—it can be shown that the angular resolution limit for an interferometer is given by the ratio of the wavelength to the baseline, which acts as an "effective aperture" of the system:

$$\Delta\vartheta \approx 1.22\frac{\lambda}{B} \tag{1.2}$$

It is easy to see, then, why this technique is superior to single-aperture telescopes for detecting close objects, such as planets within the habitable zone of their host star: if for example VLTI (that will be analysed in Section 1.5.3) is taken into consideration, its 200 m baseline makes it behave like a 200 m classical telescope aperture.

1.3 Comparison with coronagraphy

The last entry in Table 1.1 reports data for the Extremely Large Telescope and one of its instruments, METIS (Mid-infrared ELT Imager and Spectrograph)[24]. This instrument has been developed to be used with the aid of a coronagraph, which has been seen as a viable and easier-to-implement alternative to nulling interferometry.

Born as a technique to study the solar corona (hence the name), coronagraphy is a technique that consists of placing a shade in front of the instrument, located at the position of the undesired source. In the case of the Sun, for example, the shade is designed to block the photospheric emissions while allowing the much fainter signals coming from the corona to reach the detector. In the case of exoplanet detection, based on the same principle, the idea is to place the shade in front of the harbouring star.

For this reason, as will be presented later in Section 1.7.2, coronagraphy has been in competition with nulling interferometry for some missions, including NASA's Terrestrial Planet Finder[50]. However, while this technique has been able to image some exoplanets, it does nothing to improve the angular separation of the instrument, making it unfit for detecting very narrow angular separations.

1.4 Spectrum regions and exoplanets

It is common to subdivide the light spectrum into different regions, following different wavelength or frequency intervals. In modern astronomy, each region of the spectrum carries the same importance, showing different phenomena and contributing to the multi-messenger approach that is currently adopted in the description of important phenomena, some more important than others depending on the application.

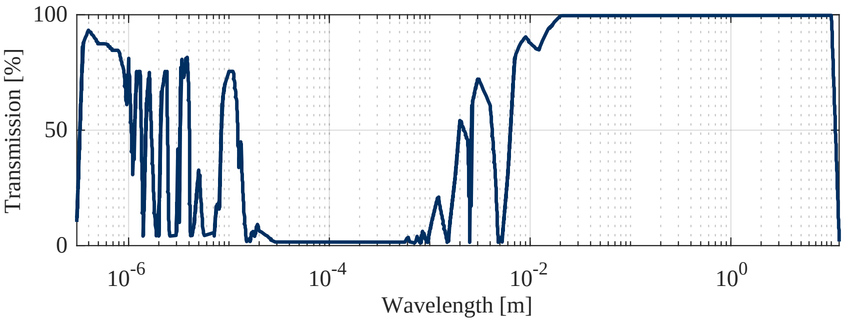

Figure 1.1: Transmission windows of Earth's atmosphere: the main limitation of ground observation is the wide presence of absorption windows due to the composition of the atmosphere. Below 0.3 µm, absorption is complete due to ozone, oxygen, and nitrogen, while above 10 m, scattering of the ionosphere closes that region[39].

Ideally, then, a complete, continuous spectrum is the result of many different actors that emit (as in the case of stars, which act as close as possible to a black body emission), absorb (as for the interstellar medium and dark matter), or modify the spectrum (with contributions from cosmological redshift and the Doppler phenomenon). Exoplanets, too, contribute to the light spectrum reaching the Earth through their emission spectrum (being a function of their effective temperature and emissivity, a normalised parameter which quantifies how far the planet's behaviour deviates from that of a black body) and the reflected light from their host star.

A hyperspectral analysis would allow a deep characterisation of any space region, but many obstacles arise in this type of analysis. On the ground, where space and reliability are less concerning aspects compared to a satellite, the absorption windows, represented in Figure 1.1, originate from the atmospheric composition and simply render some regions completely opaque to external signals. In addition to this, scintillation is a phenomenon that severely diminishes the utility of ground observation with respect to very distant sources[39].

To avoid these severe problems, going to space is the only viable solution: in space, scintillation, which is due to turbulent phenomena in the atmosphere, is completely absent, while absorption is only linked to astronomical effects.

The selection of the wavelength is the next important step. It is important to recall that exoplanets are very faint objects in a bright sky. Indeed, nulling interferometry allows for a certain level of suppression of the light of harbouring stars, but stellar leakage will be present in any case.

Following Planck's and Wien's laws, then, it is easy to verify that, assuming Earth-like planets, the best region for observations is the infrared. In fact, following the latter, planets that have an effective temperature comparable to that of our planet display a peak in the mid-infrared region (specifically, for a body which an Earth's comparable temperature, the peak would be around 10 µm), while stars, depending on their class, usually peak at significantly higher frequencies.

This concept is also displayed in Figure 1.2, which shows the contrast level for different simulated exoplanets (generated by the P-Pop catalogue[38]) both in the infrared and visible region: the emissions at the given wavelengths have been computed using Planck's law (neglecting therefore reflections of stellar light by the exoplanets), deriving the ratio. By adopting the same scale on the ordinate range, it is clear that the infrared region allows for far better ratios than the visible range, at least for some of the considered stars.

Even considering that, however, contrasts of 10^{-7} are not enough[4], and levels of 10^{-6} or higher are deemed necessary to effectively detect exoplanets[61]. It is clear, then, that the number of actually detectable exoplanets is severely limited due to the hostile conditions in which such systems will operate.

Besides practical considerations on limitations in detection, the infrared region is particularly remarkable for scientific observations: the atmosphere and, ideally, the surface of exoplanets mostly exhibit signatures in the infrared region[43]. Detections of elements like carbon dioxide, ozone, methane and waters are of great interest in the characterisations of habitability of the planet, hinting at a possible water cycle, radiation shielding and even biosignatures (methane is in fact

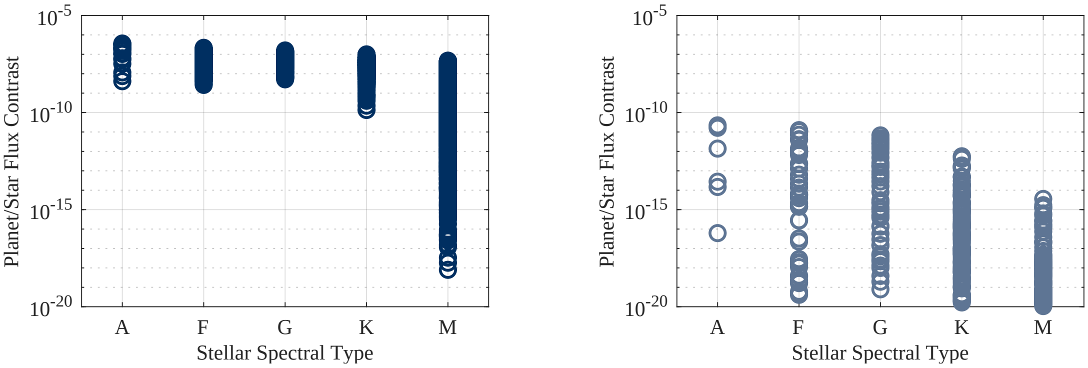

(a) Infrared (10 µm)

(b) Visible (550 nm)

Figure 1.2: Comparison of the achievable flux ratio between the planet and star flux based on the P-Pop exoplanet population at two different wavelengths (left: infrared, 10 µm; right: visible, 550 nm)[38]. The planet flux includes only the thermal emissions, neglecting any reflection.

unstable, as it quickly oxidises, being present on Earth due to bioactivity[12],[45].

1.5 Ground-based Interferometers

As explained in Section 1.2, interferometric arrays give access to angular resolution scales completely out of reach of single telescopes. In fact, such arrays, to some extent, behave as a huge telescope whose aperture is that of the physical extension of the array on the ground. One of the first ground-based interferometer is the Keck Interferometer (KI), located near the summit of Mauna Kea on the island of Hawaii. Other two examples are the Large Binocular Telescope Interferometer (LBTI) on Mount Graham in Arizona, USA and the Very Large Telescope Interferometer (VLTI) on Cerro Paranal in the Atacama Desert of northern Chile. The different locations around the globe allow for a wider coverage of the observable sky.

1.5.1 KI

Figure 1.3: Picture of the Keck Telescope. Credits: NASA[64].

The two 10-meter telescopes of the W. M. Keck Observatory (Figure 1.3) are characterised by a primary mirror comprising 36 hexagonal segments, each 1.8 m across the corners. The maximum diameter of the primary mirror is 10.95 m and its focal length is 17.5 m. The telescope aperture area is equivalent to a circular aperture 9.96 m in diameter. The average optical performance of the segments (in combination with the f/15 secondary and the tertiary mirror) is such as to concentrate 80% of a star image within 400 mas diameter[40].

The mirror segments are maintained in mutual alignment both in angle and in position, using measurements of relative axial positions of neighbouring segments, with capacitive sensors accurate to about 5 nm[40].

KI utilises adaptive optics on both Keck telescopes to correct individual wavefronts and employed active fringe tracking across all modes for path-length control. This included the implementation of co-phasing to enable long coherent integration times. Additionally, KI introduced high-sensitivity fringe-visibility measurements in the H (1.6 µm), K (2.2 µm), and L (3.8 µm) bands, as well as nulling measurements in the N band (10 µmm), facilitating research across a wide array of scientific topics[8].

1.5.2 LBTI

Figure 1.4: Picture of the Large Binocular Telescope Interferometer. Credits: Large Binocular Telescope Observatory[65].

The Large Binocular Telescope Interferometer, shown in Figure 1.4, has a unique design, comprising of the dual apertures on a common elevation-azimuth mount, which enables a broad use of observing modes. It is a high spatial resolution instrument designed for coherent imaging and nulling interferometry operating in thermal infrared and uses a baseline of 14.4 m[34].

The LBTI is characterised by a modular configuration, as shown in Figure 1.5, featuring a universal beam combiner (UBC) that can direct light to three separate camera ports. Funded by NASA, the project aims to study nearby stars that could be prime targets for future direct imaging searches for Earth-like planets. The LBTI is specifically designed for the sensitive detection of exozodiacal dust and the imaging of giant planets. The LBTI's architecture is ideated to support multiple science cameras by utilising adaptive optics and beam combination capabilities[35].

LBTI achieves nulling interferometry by directing each telescope beam through opposite sides of a single-pass, 50% transmissive beam splitter at near-normal incidence. To ensure an achromatic null, a slight difference in the thickness of the zinc selenide substrates (used for both the beam splitter and compensating window) is introduced between the two beams. This is possible since the wavebands considered are restricted, namely N-band (8 – 14 µm — NOMIC camera) and L/M-bands (3 – 5 µm — LMIRCAM camera). Precise beam alignment is achieved through adjustments using two three-axis Piezo-electric transducers (PZT) tip-tilt-piston platforms. In particular the interferometer is adjusted for nulling by tuning the phase sensor setpoint, while measuring the flux at 11 µm[34].

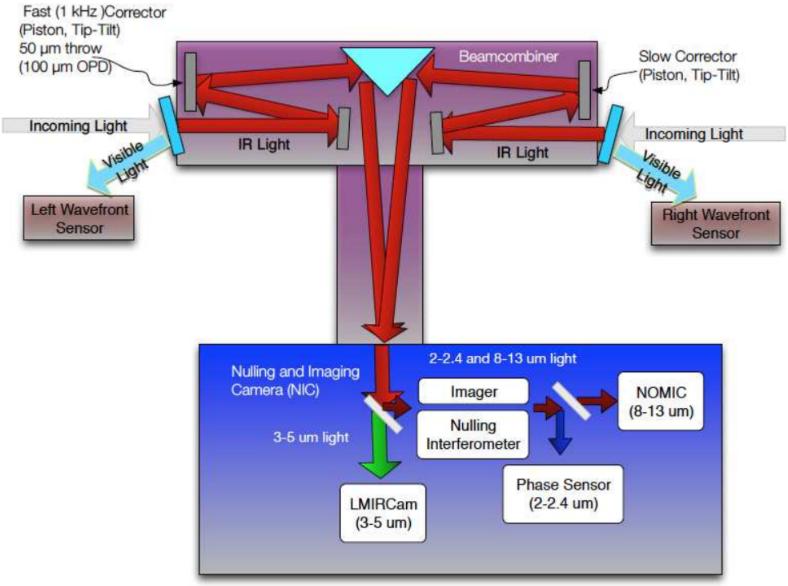

Figure 1.5: Layout of the LBTI and optical path through the beam combiner and the NIC cryostat. Starlight is first reflected by the LBT's primary, secondary, and tertiary mirrors before entering the diagram from the top right and top left. Visible light is reflected off the entrance window for adaptive optics, while infrared light passes into the LBTI, where all subsequent optics operate at cryogenic temperatures. The beam combiner uses steerable mirrors to direct the light and adjust pathlengths for interferometry[15].

1.5.3 VLTI

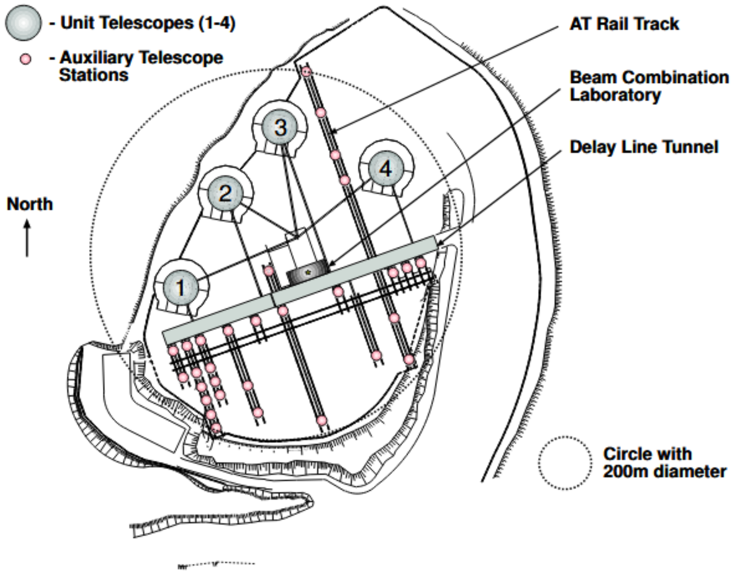

Figure 1.6: Layout of the VLTI. The four 8-meter Unit Telescopes (UTs) and the 30 stations for the 1.8-meter Auxiliary Telescopes (ATs) are represented. The AT stations are linked by rail tracks, enabling the relocation of the ATs. Also depicted are the Delay Line tunnel and the beam combination laboratory. The Delay Line tunnel accommodates eight Delay Lines, allowing the operation of four ATs and providing a total of 28 baselines per exposure. The maximum baseline length between two ATs is 200 meters (represented by a 200m-diameter circle), while the longest baseline between two UTs is 130 meters[32].

The Very Large Telescope Interferometer is composed of four 8.2 m Unit Telescopes (UT), set in a fixed location, and four 1.8 m Auxiliary Telescopes (AT) which can be relocated on more than 10 different stations, as displayed in Figure 1.6. The AT stations are connected by rail tracks on which the ATs can be relocated. After passing through a complex system of mirrors and having their light paths equalized by the delay line system, recombination is carried out by PIONIER and GRAVITY instruments in the near-infrared and by MATISSE instrument in the mid-infrared spectrum. It is unique in offering the possibility to combine a maximum baseline of 130 m, and to combine a maximum of four 1.8 m ATs. The ATs can be moved to the different stations with a maximum baseline of 200 m[32].

Thanks to its unique capabilities, the VLTI has become a valuable tool for studying a wide range of astronomical objects, including young pre-main sequence stars and their protoplanetary disks, mass-losing post-main sequence stars, binary systems and their orbits, solar system asteroids, and extragalactic objects such as active galactic nuclei[23].

1.5.4 Comparison and future ideas

Figure 1.7 shows the footprints of ground-based modern optical interferometers. In particular, the telescopes KI, LBTI, CHARA and VLTI-UT's are fixed, whereas the NPOI and the VLTI-AT's telescopes are mobile and can be repositioned. The only major facility under construction today is the Magdalena Ridge Optical Interferometer, which aims to combining up to ten 1.4 m telescopes over 350 m baselines[19].

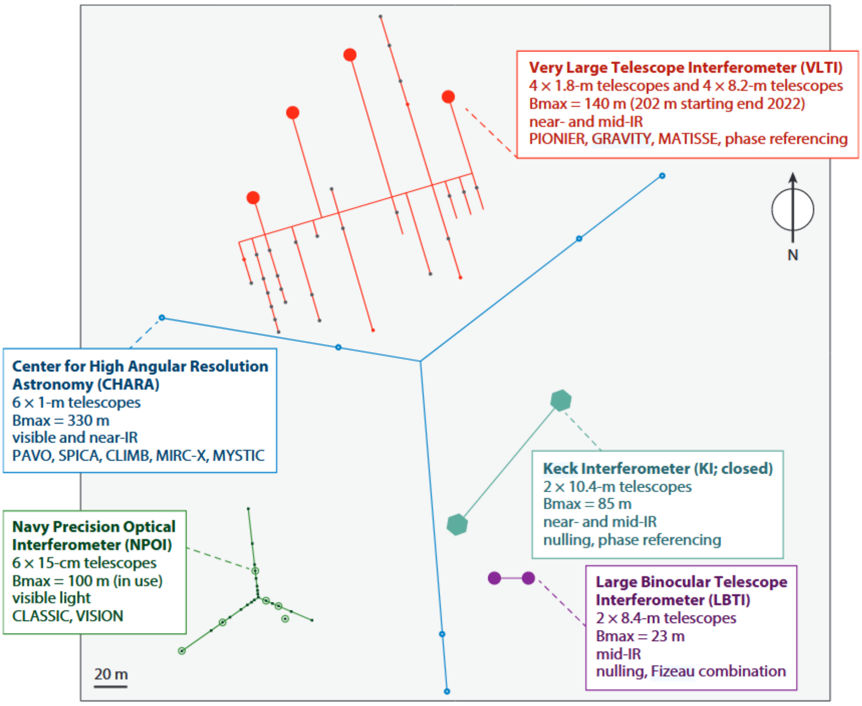

Figure 1.7: Footprints of modern optical interferometers, with telescopes and baselines to scale. The telescopes for KI (teal), LBTI (purple), CHARA (blue), and VLTI-UTs (red large circles) are fixed, whereas the NPOI (green) and VLTI-ATs (red small circles) telescopes are mobile and can be repositioned[19].

Interferometry has made significant advancements in recent years, yet current systems remain far from their fundamental performance limits. Several factors contribute to this shortfall, with some of the most significant being the limitations in adaptive optics (AO) performance, optical throughput inefficiencies, metrology laser background noise, detector noise, and structural vibrations. These challenges hinder the full exploitation of interferometers' potential, restricting sensitivity and observational precision[18].

However, ongoing upgrades and technological innovations aim to address these limitations. A major advancement is the GRAVITY+ upgrade, which incorporates laser guide star (LGS) adaptive optics and a wide-field dual-beam capability[19]. This enhancement is expected to dramatically improve sky coverage, enabling observations of a far greater number of targets than before. Additionally, existing interferometric facilities continue to evolve by broadening their accessible wavelength ranges and serving as platforms for testing emerging technologies, such as nulling interferometry.

While upcoming extremely large telescopes in the 30–40 meter class will vastly outperform current facilities in sensitivity, they will not surpass interferometers in angular resolution. The Very Large Telescope Interferometer (VLTI) and the Center for High Angular Resolution Astronomy (CHARA) will retain their unique advantage in this domain, making them indispensable tools for high-resolution astrophysical studies even in the era of ELTs[19].

An important project involving the VLTI is Asgard/NOTT, a L-band nuller which was officially presented at the VLT 2030 conference in June 2019 by ESO's Scientific Technical Committee (STC) for the visitor focus of the VLTI. Asgard/NOTT follows a series of nulling interferometers that have been deployed over the past three decades on state-of-the-art facilities, both across single telescopes and as separate aperture interferometers[18]. The key innovation is the use of a photonic beam combiner, which has only recently achieved the necessary theoretical raw contrast of 10^{-3} within this spectral range. It enables a more stable and more compact design as well as an easier alignment procedure than with free-space optics[30]. Nulling interferometry observations of exoplanets also demand precise balancing of the four VLTI pupils in terms of intensity, phase, and polarisation. The design of the warm optics and the injection system is guided by the need to optimise beam injection into the combiner while meeting the stringent requirements of nulling interferometry. The optical design of the instrument also includes the cold optics located inside a cryostat and cooled at 90 K. They comprise the injection system, the photonic chip, the spectrograph, and the detector[30]. Asgard/NOTT has the potential to carry out several exoplanet programmes to study young Jupiter-like exoplanets at the most relevant angular separations, and better understand how planets form and evolve[18].

1.6 Bracewell first concept and improvements

Interferometric methods for direct detection of extrasolar planets, which try to overcome the two main difficulties (the high contrast and the high angular resolution), are derived from the initial concept of Bracewell (1978) of a rotating two-telescope interferometer. Since then, a substantial body of work has been published in which a variety of array configurations of interferometers have been proposed for exoplanet detection[11]. Figure 1.8 shows a scheme of the evolution of the preferred nulling architectures until 2007.

1.6.1 Bracewell principle

The space-based interferometer proposed by Bracewell is characterised by two apertures and light recombination in phase opposition. This setup creates a dark fringe along the line of sight, significantly reducing stellar emissions. For an off-axis source, light transmission depends on the baseline length and wavelength, which together determine the interferometer's transmission map. In order to retrieve the planet from all signals and distinguish it from the background, Bracewell proposed to rotate the interferometer around its line-of-sight. As the planet moves, it crosses both bright and dark fringes, causing its flux to be modulated, while the uniformly distributed background remains unaffected[13].

Figure 1.9 shows the monochromatic transmission map, namely the intensity response of a typical nulling Bracewell interferometer. Starting from the computation of the expression of the electrical field produced by a point source of unit flux, it is possible retrieve the interference pattern and define which parts of the field-of-view are transmitted by constructive interference, and which are blocked by destructive interference[17]. The star is positioned at the central dark fringe, while potential planets can appear anywhere in the sky.

By rotating the interferometer around the line of sight, planets pass through different fringes, leading to variations in transmission as shown. To extract the planet's modulated signal, a cross-correlation transform is applied between the expected signals and the actual modulation observed. However, this modulation has a drawback: on average, the detected planetary signal is reduced by 50% in a Bracewell interferometer[13].

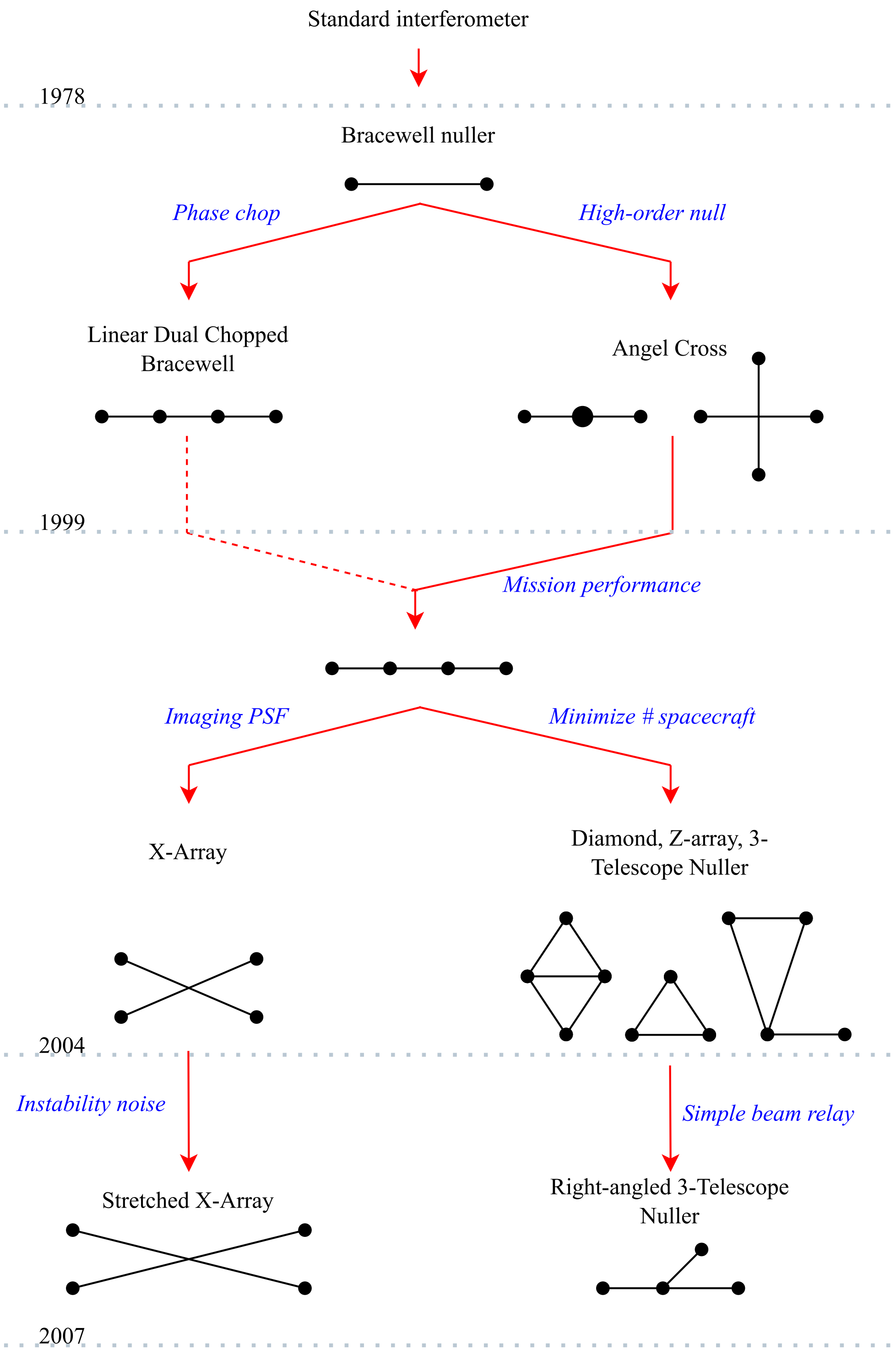

Figure 1.8: Schematic representation of the preferred nulling architecture up to 2007. Readapted from TN2-ESA nulling interferometry[9].

The main disadvantage linked to the single Bracewell configuration is that the response on the sky is symmetric on either side of the star, therefore, the planet position angle has 180° ambiguity meaning that is difficult to separate the planet signal from other sources of emission and it is not possible to perform phase chopping[17]. As a result, improved configurations with more than two collectors have been proposed to overcome these limitations, as the Angel Cross configuration and the Kernel interferometer.

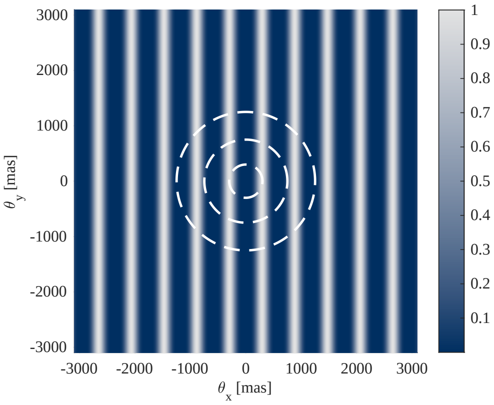

Figure 1.9: Transmission map of a typical Bracewell interferometer. As the interferometer rotates, hypothetical planets (represented by the white line) cross bright and dark fringes.

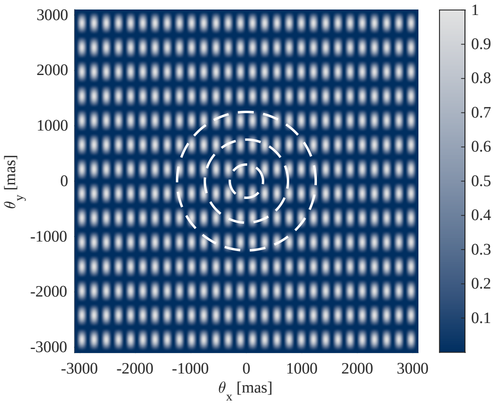

Figure 1.10: Transmission map of a generic X-array interferometer. With respect to the Bracewell interferometer, which produces a mono-dimensional transmission map, if the apertures are on a plane, they will produce a bidimensional transmission map.

1.6.2 Angel Cross and asymmetric configuration

In 1990 Angel proposed a configuration of four telescopes in a square shape, combined with multiple beam-splitter for transmission varying as $\sin^4\theta$ instead of $\sin^2\theta$ and named Angel Cross. It is indeed a double Bracewell interferometer, where the two outputs are recombined with no additional phase shift. This configuration allows to overcome the strict constraint on the pointing accuracy[3].

Furthermore, in order to detect Earth-like planets despite the fact that the bright exo-zodiacal light is modulated at the same frequency as the planetary signal, the solution is to design an interferometer with an asymmetric transmission map, so that every planetary system can be treated in the same way, independently of their inclination. In 1996, Léger et al.[54] proposed an asymmetric array, made up of five telescopes, regularly located on a circle. Subsequently, Mennesson and Mariotti[61] proposed an improvement of the circular array, based on an elliptical configuration. The elliptical configuration produces an irregular transmission map, allowing precise localization of the planet. Additionally, when the array rotates around its centre, azimuthal holes are eliminated, ensuring that all angular separations maintain a strong modulation amplitude. As a result, a variable baseline is no longer necessary.

In general, transmission map will change depending on the number and the position of the apertures, as shown in Figure 1.10, which represents the transmission map of a generic X-array interferometer. While the Bracewell interferometer produces a mono-dimensional map, considering in-line apertures, in this case a bi-dimensional transmission map is observable.

However, this setup introduces a new challenge: because the telescopes are positioned at varying distances from the central recombining hub, continuously adjustable long delay lines are required to equalize the optical path lengths of the incoming beams[1].

1.6.3 The importance of phase chopping

In order to modulate the desired signal in presence of varying backgrounds and detector shifts, the phase chopping technique is necessary. If the desired signal can be intentionally modulated (chopped) at a frequency that is unlikely to be mimicked by other signals, the chopped planetary signal will average to a stable value, while drifts will tend to cancel out. In practice, the chopping frequency is determined by the detector's minimum readout time, ensuring that readout noise remains significantly lower than the detected photon flux. As a result, typical chopping frequencies range between 0.1 and 0.01 Hz. This approach also significantly reduces constraints on the interferometer's rotation frequency. In particular, regarding nulling interferometry, the principle is to use two or more subsets of nulling interferometers, and combine them is such a way that the point-like planetary signal is strongly modulated whereas the extended background sources are not[1].

1.6.4 Kernel improved interferometer

To address the limitation related to the extreme sensitivity of the instrumental response to tiny optical path differences between apertures, the Kernel-nuller architecture has been proposed. In particular, the idea is to alleviate this effect with an integrated combiner design that allows the generation of observables that are inherently resistant to residual optical path differences[49].

The architecture and methodology of the Kernel-nulling interferometry concept enables simultaneous advantages: leveraging the high-contrast enhancement of the nuller while preserving the ability to detect the otherwise degenerate effects of varying observing conditions. This allows for the construction of observables that remain resilient to such spurious influences. Much like closure-phase, the kernel-nulled outputs also resolve the symmetry degeneracy inherent in a classical nuller's output, with the signs of different kernels indicating the location of asymmetric structures within the field of view[58].

1.7 Space-based Interferometers

For the reasons presented in Section 1.4, in past years there has been a strong interest in developing a space-based interferometry mission. Absorption- and scintillation-free missions would fully unlock the potential of this technology, but the novelty of the technology on one hand and the high technical difficulties and costs on the other have prevented the practical realisation of a real mission.

That being said, over the years, there have been many proposals from both the two largest space agencies, ESA and NASA, which followed two different approaches: either simplifying the design and reducing the number of involved spacecraft for the former or increasing the imaging properties of the system for the latter[9].

1.7.1 Darwin

Darwin was a proposed four-aperture space-based interferometer formed by a constellation of five satellites, with the main objective of studying exoplanets and advancing specific topics of ESA's Cosmic Vision project[54], such as planet formation and habitability.

Its design was based on the need for high angular resolution, equivalent to 100 m class telescopes in the mid-infrared range, to target habitable zones between 10 and 100 mas[54]. However, the design underwent multiple revisions over time: for example, until 2004, a six-free-flying 1.5 m telescope configuration arranged in a hexagonal pattern, launched by a single Ariane 5 vehicle, was considered[27],[10], as well as a three-telescope nuller configuration[10]. The final array configuration, adopted around the possible merging with TPF-I, called the "Emma X-Array" after Charles Darwin's wife, utilised four collectors in a planar configuration, followed by a collector that was out of plane, increasing sky coverage and reducing design complexity[54].

Clearly, the main drawback of having such a large baseline is linked to the necessity of formation flying, which significantly increases the likelihood of failures and risks: if any of the spacecraft, for any reason, is unable to sustain its role, the mission is lost. In addition to this fundamental aspect, the precision and stability required for formation flying are considered a major challenge[54],[27],[28].

A minimum null depth requirement of 10^{-5} was established, enabling a search strategy targeting more than 200 stars (with a focus on F, G, K, and M-type stars), leading to the characterisation of 25 to 50 exoplanetary atmospheres and biosignatures over a five-year baseline mission[54],[27].

In conclusion, Darwin was the subject of many development papers[1], which led to a deep understanding of its behaviour and were extensively used in future missions like LISA. However, due to technical and budgetary constraints, as well as a shift in the strategy for exoplanet searches and immaturity of the technologies[10], the mission was indefinitely shelved in 2007[21].

Nowadays, if the mission were to be recovered, it would indicate as possible precursors, inheriting their knowledges and developments, missions like COROT (CNES), Kepler (NASA), PRISMA (SSC), PROBA-3 (ESA), and Pegase (CNES), which all introduced some progress in the research[54].

1.7.2 Terrestrial Planet Finder Interferometer

NASA's development of a mission for terrestrial planet finding followed a similarly long development phase to Darwin, where both a coronagraph (the TPF-C version) and an interferometer (TPF-I version) were considered in the initial phases. The former had advantages in requiring smaller apertures and no cooling in the visible domain[75].

Similarly to the European project, TPF-I involved (at least in one version - since a structurally connected interferometer with a truss structure was also considered, but this choice led to lower achievable baselines[75] -) formation flying with spacecraft separated by up to 100 m (in a proposed X-Array[50]) for the survey of 150 stars in the F, G, and K classes and the characterisation of detected exoplanets in the mid-infrared region[75].

The four subsystems that required intensive testing were summarised by the COST acronym: controls, optical, structural, and thermal. Each of them proved particularly complex, with tight control and strong thermal modelling requirements (below 40 K for the optical surfaces[78]). The flight formation interferometer was conceptualised with over 100 optical elements and primary mirrors exceeding 4 metres in diameter[78].

Starting in 2007, a common architecture was defined in collaboration with ESA, significantly simplifying the design and increasing the coverage in space[50] by exploiting the Emma X-Array. During the following decade, plans were proposed to increase the TRLs of both formation flying and nulling interferometry to acceptable thresholds, with the aim of initiating a possible Phase A around 2020[50].

This project, however, was indefinitely deferred, likely for reasons similar to those that led to the shelving of Darwin, although other investments in space interferometry have continued[50]. Again, precursors missions to a new, possible return, were the COROT and Kepler missions[68].

1.7.3 Large Interferometer For Exoplanets

The LIFE mission, proposed by a Swiss team at ETH Zürich, is a more recent evolution of the previously discussed missions, dating from 2017[71]. It is based on the same principle as the Emma X-Array in a formation flying configuration[31].

Ongoing research is assessing the feasibility of the mission[71],[14], evaluating its feasibility and signal sensitivity, and proposing the mission for ESA's Voyage 2050 programme[31].

Similarly to Darwin and TPF-I, LIFE aims to characterise around 30 rocky planets with an extended baseline of approximately 600 m for imaging in a Double Bracewell configuration[31]. Challenges have again arisen regarding formation flying, which will be addressed by ESA's PROBA-3 mission (launched in December 2024) and NASA's STARLING mission (launched in 2023), as well as interferometric fringe tracking and nulling performance at cryogenic temperatures[31].

1.7.4 Comparison

Table 1.2 presents an overview of key parameters for the considered missions (at least in one of their iterations). The similarities in the presented values illustrate how all of them converge towards an optimised design.

Similarly, Figure 1.11 displays the ideal number of detectable exoplanets based on the simplified computation of the inner and outer working angles for the three presented interferometers. Although the numbers are only indicative due to the simplified analysis, this graph clearly shows that the dominant parameter in the analysis, as expected and as declared, is the baseline: the outer working angle, which in turn is affected by the diameter, has little consequence on the design (provided that it is large enough), and even if the TPF-I had double the diameter of Darwin (at least during one of the iterations), its yield is far smaller than the other two proposed missions.

It is clear, then, what the appeal of a formation flying interferometer is: even with the use of deployable surfaces, results like those reported in Table 1.2 will not be achievable, significantly

Name	**λ** [µm]	**Δt** [yr]	**B** [m]	**D** [m]
Darwin[54]	6-20	5	500	2
TPF-I[50]	6-18	5	100	4
LIFE[31]	6-16	5	600	4

Table 1.2: Comparison of the bandwidth, mission duration, maximum baseline, and aperture diameter of the three presented space interferometers.

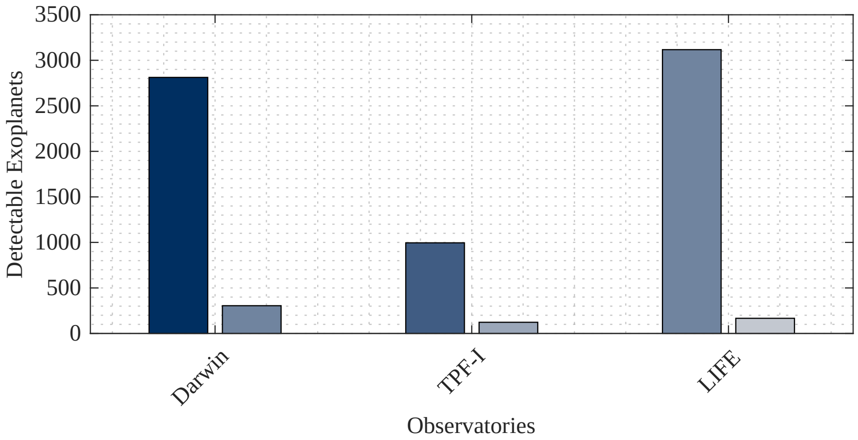

Figure 1.11: Comparison of the ideal (maximum) yield of exoplanets based (left series) and the yield of exoplanets with a cut-off around 10^{-7} contrast ratio (right series), based on the data from Table 1.2 and the exoplanet catalogue generated by P-Pop[38].

reducing the number of detectable exoplanets.

On the same figure, however, if the sensitivity cut-off is applied (that being the fact that some contrast ratios are too faint for their detections), the situation significantly changes and as it can be seen, the three observatories becomes effectively comparable. That being said, quality is usually preferred over quantity, and given the fact that prolonged observation times are needed to fully characterise the exoplanets[54],[68], during the baseline mission duration, only a limited number of targets will be studied.

1.8 Conclusions

Nulling interferometry represents one of the most promising techniques for the direct detection and characterization of exoplanets. This work has provided a comprehensive overview of its principles, advantages, and applications, examining both ground-based and space-based implementations. While ground-based interferometers such as LBTI and VLTI have demonstrated the capabilities of this technique, their effectiveness, especially in desired mid-infrared region, is constrained by atmospheric interference and limited wavelength coverage.

Space-based interferometry can therefore be the definitive solution: originally introduced by Bracewell, it has evolved in multiple configurations, like the Angel Cross and Kernel-nulling interferometers, which mitigate phase and alignment challenges. Despite proposals from both ESA and NASA, technological and budgetary constraints have so far prevented their realization. However, ongoing developments suggest that the feasibility of a dedicated space-based nulling interferometer is steadily increasing.

Through our analysis, we have highlighted the challenges that must be addressed: achieving sufficient null depth, improving formation-flying precision, and developing high-sensitivity detectors that can operate in extreme space environments. The maturation of these technologies, supported by precursor missions like PROBA-3 and STARLING, will likely enable the next generation of exoplanet studies.

Ultimately, nulling interferometry remains at the forefront of the quest to answer one of the most profound scientific questions: are we alone in the universe? As advancements continue, this technique holds the potential to revolutionise our understanding of planetary systems and the search for biosignatures beyond our solar system.

Chapter 2

Nulling interferometer optical design considerations

In order to properly perform the opto-mechanical design, some design consideration have to be introduced. This chapter presents the general design principles and characteristics of a stellar interferometer. While Viseur's work[57] specifically focused on a two-aperture configuration, the presented discussion extends this foundation by addressing the design of a four-aperture nulling interferometer, thereby contributing to a more complex and realistic system architecture for future space missions[7]. Starting from a description of the main components and their functions, the analysis continues with the introduction of the optical parameters of interest, namely the optical path difference and the relative phase distribution. Finally, the concept of intensity response is presented, followed by an overview of the instrument limitations.

2.1 Optical components of a stellar interferometer

The fundamental functions of an optical interferometer can be categorized into four primary components, namely the beam collection, the beam transport, the beam combination and the detection. The basic layout of a four apertures interferometer is shown in Figure 2.1. While, Figure 2.2 illustrates the block diagram of the optical path and components of a generic four apertures interferometric system, highlighting the control mechanism of the optical path lengths and phases of the individual beams.

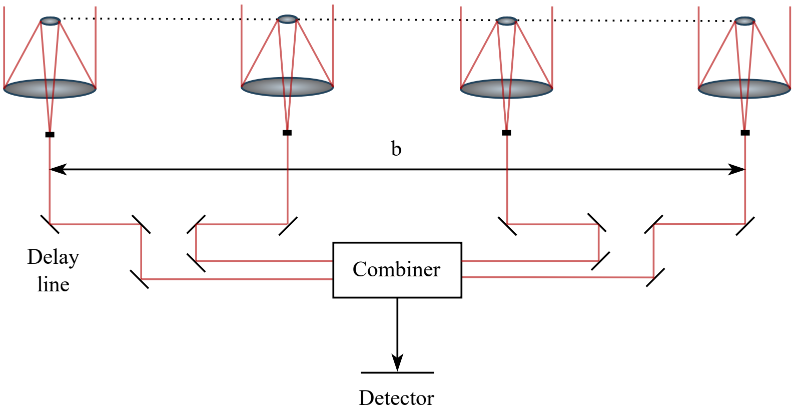

Figure 2.1: Basic layout of a generic four apertures interferometer. Light is sent through a tilt correction system, an optical path length equalizer, and finally to a central location where fringes are formed; b represents the baseline of the interferometer; the Optical Delay Line (ODL), the beam combiner and the detector are also represented.

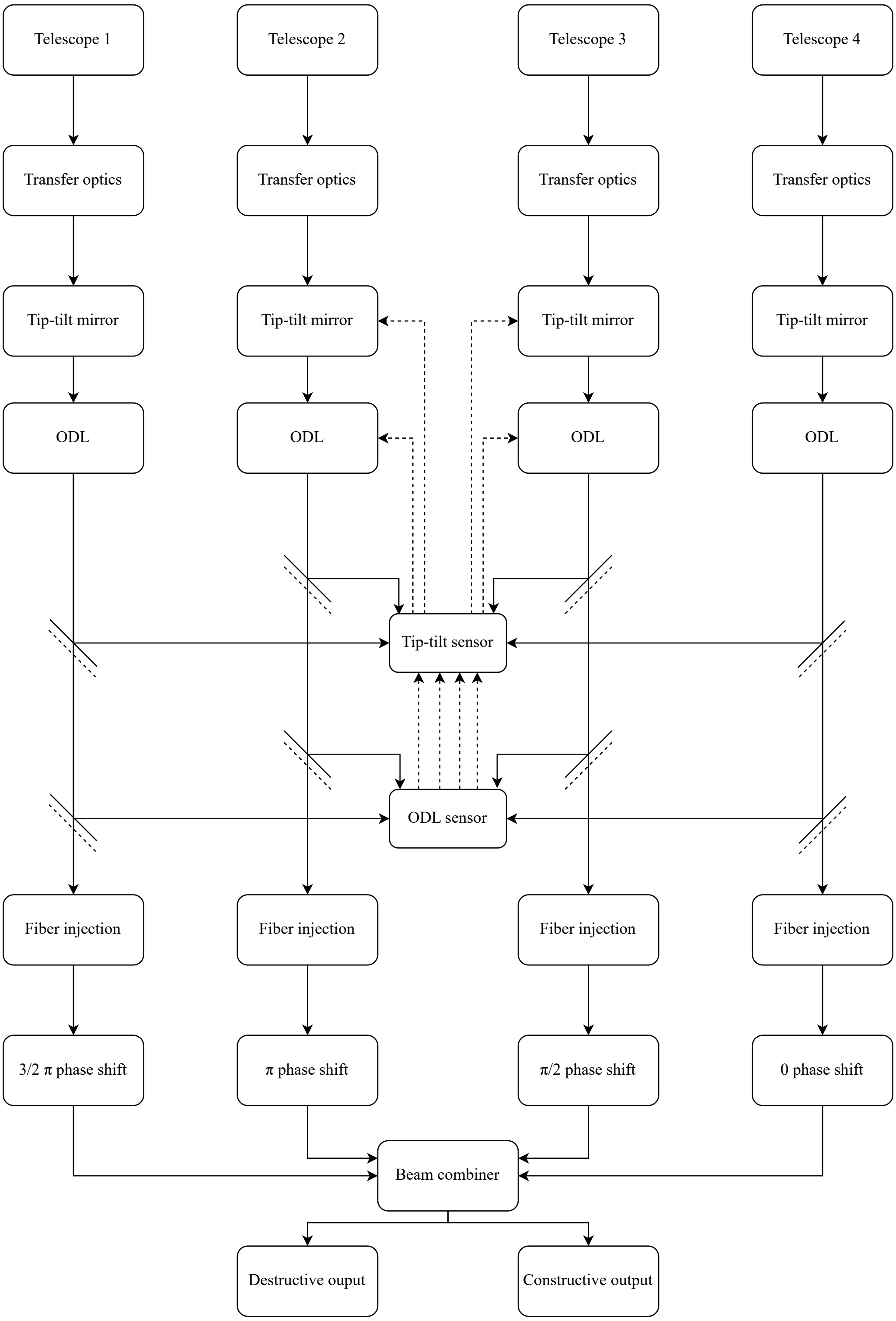

Figure 2.2: Block diagram of a generic four aperture nulling interferometer.

2.1.1 Beam collection

Beam collection of the light coming from the astronomical source can be performed by classical telescopes, or siderostats. While classical telescopes are characterised by a large collecting area and can be composed of multiple apertures and therefore, high degree of complexity, siderostats are flat mirrors directly sending light to the interferometer or to a fixed telescope acting as a beam compressor. Therefore, the design of siderostats is simpler but characterised by a limited field of view and requiring a larger secondary mirror due to the large beam gathered. However, since nulling interferometers only point at stars, this is not really an issue.

2.1.2 Beam transport

The beam transport is carried out by an optical train, used to propagate the light beams from the collection to the combination site. In order to preserve the relative polarisation of the beams, the mirror geometry and the coating have to carefully been considered[2]. Beam correction is thus crucial in order to ensure coherence and maintain high quality interference patterns and can be performed with tip/tilt mirrors, adjusting the incoming beam and deformable mirrors, addressing wavefront errors by adjusting their shape. In particular, tip/tilt mirrors allow for precise alignments between the beams from the different collecting telescopes before interference occurs. While deformable mirrors introduce controlled phase shifts across the aperture to achieve the desired interference pattern, correcting the wavefront[57]. Both types of mirrors function within a closed-loop system with feedback. The control system processes sensor measurements of the light and then adjusts the mirror's shape or orientation accordingly, ensuring continuous correction and monitoring to preserve interferometry quality[57].

Furthermore, Optical Delay Lines (ODL) are also present in order to compensate for optical path length differences between telescopes in the optical trains (internal delays) or to counteract for the delay due to the geometric arrangement of the apertures (geometric path delays). As the geometric delays change constantly while the observed star moves across the sky, it has to be compensated with high frequency during the observation. In fact, the waves from the individual telescopes must experience the same delay before they can be recombined[46].

Optical delay lines can be categorized according to factors such as design, operating principle, and adjustability. For example, free-space delay lines adjust the optical path length by extending the physical distance a light beam travels through free space. This is typically accomplished using mirrors, prisms, or beam splitters. To maintain beam quality, a collimated beam with a sufficiently large radius is essential, ensuring the Rayleigh length surpasses the path length and preventing significant beam expansion. These delay lines can be classified into two types: fixed and variable[60], which setup is displayed in Figure 2.3. Another example is fibre optic delay lines which create a controlled delay in light signal propagation by utilizing optical fibre. This is achieved by extending the optical path, similar to free-space delay lines, while also slowing the light's transmission through a high-refractive-index core. Fixed optical path delay lines are preferred for interferometry applications, providing a simple design, low cost and widely availability and a stable and predictable delay over time[60].

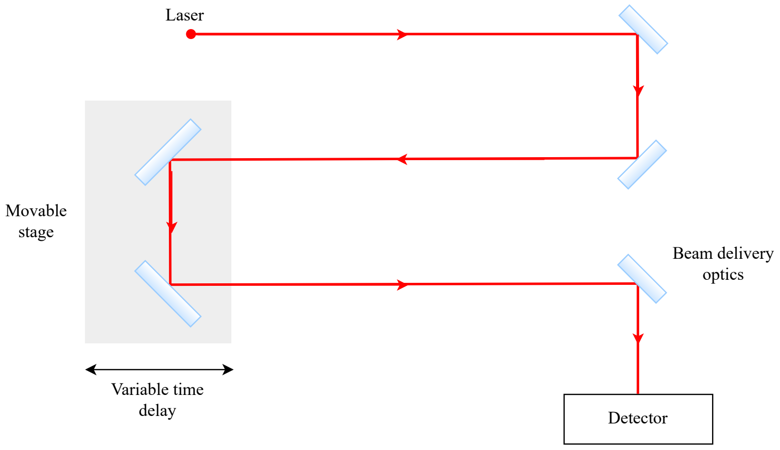

Figure 2.3: Setup of a variable free-space optical delay line[60].

Fringe and angle trackers are also very important in order to achieve high-quality results. The objective is in fact to monitor the interference patter, detecting any deviation in position or intensity, which may arise from vibrations or other perturbations. The fringe or angle tracker's control system takes corrective actions to restore the fringes or mirrors angles to their original position and intensity by adjusting the optical interfaces of the design[77].

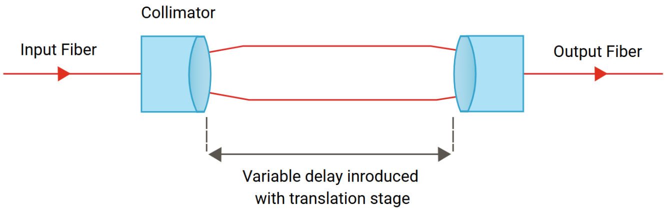

Figure 2.4: The Variable fibre optic delay line operates by controlling the delay through the device by varying the distance the light travels between the input and the output fibre collimator[60].

2.1.3 Beam combination

The beam combination can be co-axial or multi-axial[41], as shown in Figure 2.5. Co-axial beam combination involves pairwise combinations using beam splitters while in multi-axial beam combination the beams are sent to a single imaging optical system[2].

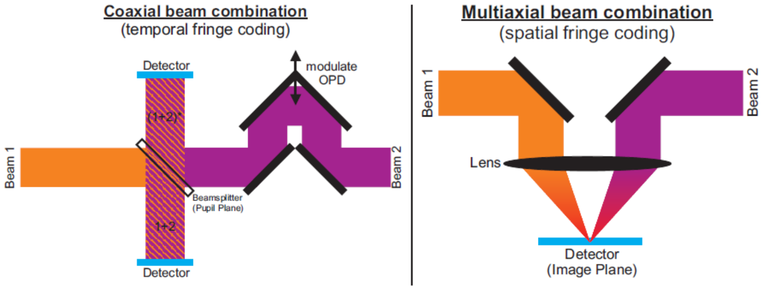

Figure 2.5: Basic principles of beam combination[46].

Modal filtering can be applied after the coherent recombination of beams using a single waveguide instead of positioning a waveguide at each telescope focus. This approach prevents any additional phase corruption after filtering and eliminates differential effects caused by variations between individual waveguides[47]. Furthermore, modal filtering base on the implementation of single-mode waveguides presents a clear advantage for nulling interferometry. Single-mode waveguides are preferred to pinholes since they are efficient for high-order and low-order defects, while the latter devices are efficient just for the small-scale defects[47].

2.1.4 Beam detection

Finally, the fringe detection depends on the beam combination mode, in particular for the co-axial mode a pupil plane is used, while for the multi-axial mode an image planed is preferred. In the case of a pupil plane, fringes are temporally encoded using two single-pixel detectors positioned at each output of the beam splitter, achieved by modulating the optical path of one beam with a dither mirror. On the other hand, regarding the image plane, fringes are spatially encoded on a focal plane array, appearing as intensity modulation within a classical Airy pattern due to variations in beam delay across the focal plane[2].

2.2 Optical parameters of interest

In order to analyse the performance of optical interferometers, two important optical parameters of interest are the optical path difference and the relative phase distribution. In particular, the goal is to have an optical path difference as low as possible considering each arm of the interferometer, meaning that, even if the system is subjected to any perturbation the correct functioning is guaranteed.

2.2.1 Optical path difference

The optical path length (OPL) is the distance in vacuum equivalent to the distance traversed in the medium of index n[33]. Considering an inhomogeneous medium, where the refractive index n is a function of position, the OPL is given by

$$OPL = \int_S^P n(s)\, ds, \tag{2.1}$$

where S and P correspond respectively to the initial and final position of the ray. In particular, the optical path difference (OPD) is the difference between two optical path lengths and it is computed taking into account the nominal configuration and the perturbed one, resulting in

$$OPD = OPL_{nominal} - OPL_{perturbed}. \tag{2.2}$$

As already mentioned, in order to have a good system, the OPD must be as low as possible.

2.2.2 Relative phase distribution and phase difference

The optical path distribution is strictly related to the phase distribution by the following relation[33]:

$$\phi = 2\pi \frac{OPL}{\lambda}. \tag{2.3}$$

Therefore, the resulting phase difference between the nominal and the perturbed configuration is given by

$$\Delta\phi = 2\pi \frac{OPD}{\lambda}. \tag{2.4}$$

2.3 Intensity response

While the primary focus of this thesis is the opto-mechanical design of a four-aperture nulling interferometer, a basic understanding of the system's optical response is essential to contextualize the performance requirements and the design constraints. In particular, the ability of the interferometer to suppress on-axis starlight and transmit off-axis planetary signals depends on the spatial interference pattern it produces — the so-called intensity response or transmission map.

This section provides a brief mathematical description of the intensity response of a multi-aperture nulling interferometer. The purpose is not to derive the equations in full detail, but rather to introduce the fundamental relationships that underpin the analytical modelling presented in Chapter 5. These expressions form the basis for evaluating the performance of different interferometric configurations and help clarify the optical principles guiding the mechanical layout developed in this work.

Figure 2.6 represent a generic configuration of a nulling interferometer and the target system. At the output of the interferometer, the total detected photon rate can be written as

$$N = \int_\theta \int_\alpha B_{sky}(\mathbf{s}) R(\mathbf{s}) P(\mathbf{s}) \theta \, d\theta \, d\alpha, \tag{2.5}$$

where B_{sky} is the brightness distribution on the sky for a spectral channel centred on wavelength λ and a bandwidth $\Delta\lambda << 1$, $\mathbf{s}$ is a unit vector whose direction represents the position in the sky, $P(\mathbf{s})$ is a field-of-view taper function resulting from the size of a collecting aperture and the input response of the single-mode spatial filter and $R(\mathbf{s})$ is the intensity response of the interferometer in the sky corresponding to the transmission map[17], introduced in Section 1.6.1.

In order to retrieve the transmission map, the first step is to compute the expression for the electric field generated by a point source with unit flux at position $\mathbf{s}$. Given the linearity of Maxwell's equations, the result is obtained by summing the contributions from each collector[17]:

$$r(\mathbf{s}) = \sum_j A_j \exp\left[i \left(\phi'_j + \frac{2\pi}{\lambda} \mathbf{x_j} \cdot \mathbf{s} \right) \right], \tag{2.6}$$

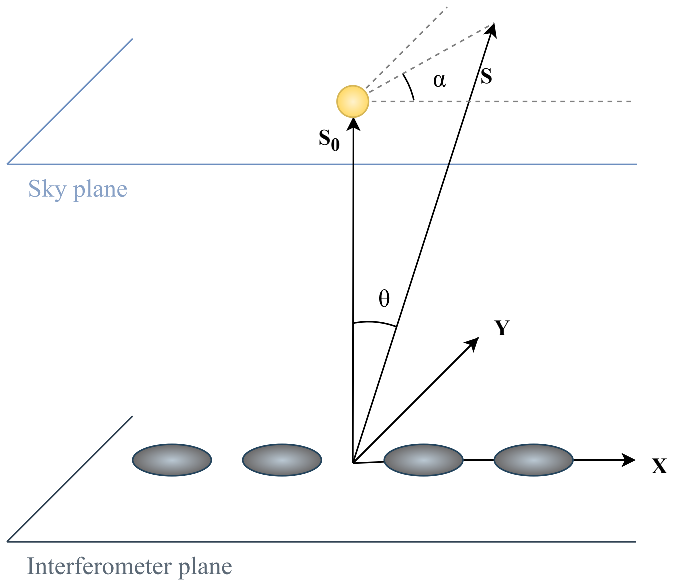

Figure 2.6: Schematic of a generic nulling interferometer and target system. The two angular coordinates (θ, α) denote the position in the sky plane.

where j is the index identifying the collector, i is the imaginary unit, A_j is the electric field amplitude response for the collector j, scaled such that A_j^2 represents the detected photon rate from a source with a flux of 1 photon/m^2, $\phi_j^{'}$ is the relative phase shift for the collector j and x_j the vector position fro the centre of collector j. Therefore, the transmission map is given by

$$R(\mathbf{s}) = r(\mathbf{s})r^*(\mathbf{s}) = \left\{\sum_j A_j \exp\left[i\left({\phi^{'}}_j + \frac{2\pi}{\lambda}\mathbf{x_j}\cdot\mathbf{s}\right)\right]\right\}\left\{\sum_k A_k \exp\left[-i\left({\phi^{'}}_k + \frac{2\pi}{\lambda}\mathbf{x_k}\cdot\mathbf{s}\right)\right]\right\} \tag{2.7}$$

$$= \sum_j\sum_k A_j A_k \cos\left({\phi^{'}}_j - \phi_k^{'} + \frac{2\pi}{\lambda}\mathbf{x_j} - \mathbf{x_k}\cdot\mathbf{s}\right). \tag{2.8}$$

This expression describes the interference pattern, determining which regions of the field of view are transmitted through constructive interference and which are obstructed by destructive interference[17].

It is now possible to substitute the expression of the transmission map (Equation 2.8) in Equation 2.5, resulting in[17]

$$N = \sum_j\sum_k A_j A_k \Bigg[\cos(\phi_j - \phi_k)\int_\theta\int_\alpha B_{\text{sky,sym}}(\theta,\alpha)P(\theta)\cos\left(\frac{2\pi}{\lambda}b_{jk}\cos\alpha\right)\theta\, d\theta\, d\alpha$$
$$- \sin(\phi_j - \phi_k)\int_\theta\int_\alpha B_{\text{sky,asym}}(\theta,\alpha)P(\theta)\sin\left(\frac{2\pi}{\lambda}b_{jk}\cos\alpha\right)\theta\, d\theta\, d\alpha\Bigg], \tag{2.9}$$

where $b_{jk} = (x_{jk}^2 + y_{jk}^2)$ is the length of the projected baseline between collectors j and k and $B_{sky,sym}$ in the symmetric and, respectively, $B_{sky,asym}$ in the asymmetric are the brightness distribution on the sky for a spectral channel centred on wavelength λ. In order to simplify the expression, since the double integrals are two-dimensional Fourier transforms of the sky brightness distribution, it is possible to write[17]

$$N = \sum_j\sum_k A_j A_k[\cos(\phi_j - \phi_k)\bar{B}_{sky,jk,sym} - \sin(\phi_j - \phi_k)\bar{B}_{sky,jk,asym}\, d\theta\, d\alpha]. \tag{2.10}$$

One can observe that if a baseline has a phase difference of 0, $\pm\pi$ or $\pm 2\pi$, its contribution to the photon rate arises solely from the symmetric brightness distribution, whereas a baseline with a phase difference that is an integer multiple of $\pi/2$ interacts exclusively with the asymmetric brightness distribution (similar to a planet).

2.4 Limitations of the instrument

A fundamental requirement for a nulling interferometer is to achieve a deep central null, effectively reducing stellar light by a factor of approximately 10^7. Mennesson and Mariotti (1997)[61] demonstrated that, for the target stars and interferometric baselines considered in this study, this condition can only be met if the interferometer's central transmission scales as θ^4 (or higher power). Such configuration are denoted as high-rejection configuration[2].

Also other disturbances, mainly related to the thermal emission of the zodiacal and exozodiacal dust, and to the instrument itself, have to be taken into account and suppressed. Figure 2.7 shows a schematic representation of 4-apertures interferometer, represented with the main noise sources, namely the local zodiacal disk, the exozodiacal dust disk and the instrument thermal emission.

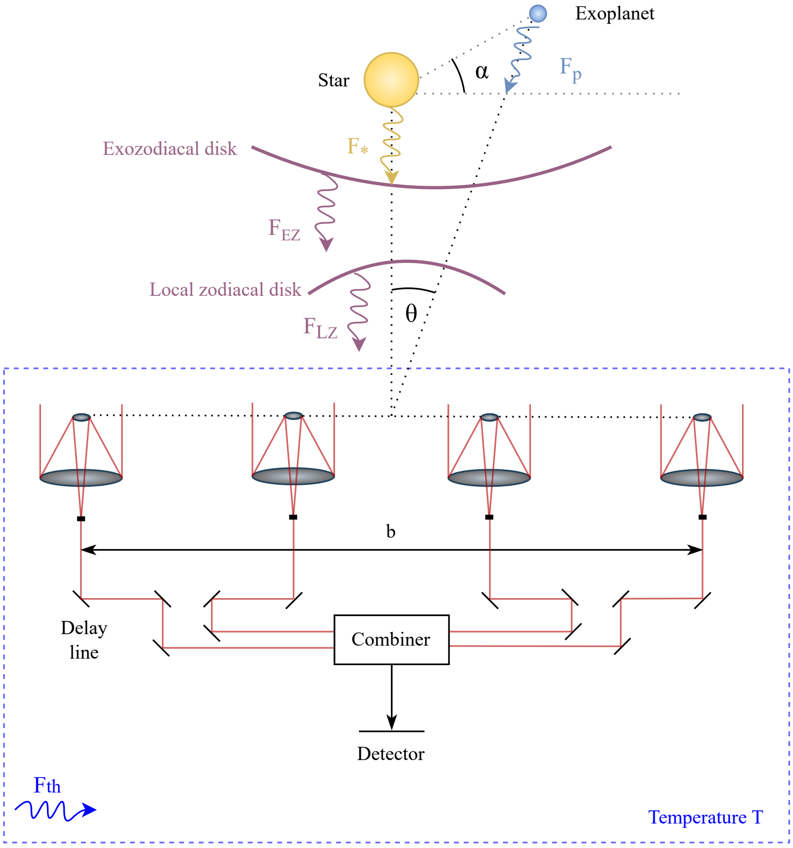

Figure 2.7: Schematic representation of 4-apertures interferometer with the main noise sources: F_* is the stellar flux; F_p is the planetary flux; F_{EZ} is the exozodiacal flux; F_{LZ} is the local zodiacal flux; F_{Th} is the thermal flux of the instrument at temperature T. Readapted from the PhD thesis of C. Dandumont[12].

The local zodiacal disk is a diffuse structure surrounding the Sun, composed of dust from active comets and colliding asteroids. Heated to approximately 265 K at 1 AU, it significantly contributes to the infrared background observed by Darwin. In fact, the total zodiacal flux collected by 1-meter-class telescopes is about 1000 times stronger than the flux from an Earth-like exoplanet at 10 µm. Since this signal remains unaffected by the array's rotation, it can be mitigated through signal processing. However, the main challenge arises from its associated shot noise and potential long-term brightness variations, which could be mistaken for the planet's slowly modulated flux unless rapid signal chopping is employed[2].

The exozodiacal dust disk potentially surrounds the target star and considering its similarity to the Solar System's zodiacal disk, its total flux would be approximately 300 times stronger than the emission of an Earth-like planet at 10 µm. The primary challenge with the exozodiacal disk is that its emission is also modulated by the array's rotation (unless viewed face-on), which can make it difficult to distinguish from a planet's signal[2].

Finally, the instrument's thermal emission is modelled as grey body emission, meaning it is a black-body emission scaled by a constant emissivity factor that depends on the optical system. The average value of the instrumental background can be eliminated using the three inclined observations, leaving only the fluctuations. To avoid causing significant variations in the background emission, high thermal stability is essential. To detect an Earth-like planet at 20 pc with a signal-to-noise ratio (SNR) of 5 at 10 µm, the thermal stability must be maintained at or below 0.1 K rms for an instrument cooled down to 45 K[17].

Therefore, the total photon rate can be written as a sum over all possible pairs of collectors, containing all the contributions from the planet N_{planet}, the star N_*, the exo-zodiacal cloud N_{EZ}, the local zodiacal cloud N_{LZ}, the stray light N_{stray}, and instrumental thermal emission $N_{thermal}$. Equation 2.10 can be written as[17]

$$N = N_{planet} + N_* + N_{EZ} + N_{LZ} + N_{thermal} = N_o + \delta N, \tag{2.11}$$

where N_0 represents the sum of the photon rate for an ideal instrument without perturbation, while δN is the additional photon rate due to the presence of perturbations, also called the perturbation leakage.

In particular, the expression of the difference noise sources are presented as follows[17][52]:

- contribution from the planet:

$$N_{planet} = F_p \sum_j \sum_k A_j A_k \Bigg[\cos(\phi_j - \phi_k) \cos\left(\frac{2\pi}{\lambda} b_{jk}\theta_p \cos\alpha_p\right) \tag{2.12}$$

$$- \sin(\phi_j - \phi_k) \sin\left(\frac{2\pi}{\lambda} b_{jk}\theta_p \cos\alpha_p\right) \Bigg], \tag{2.13}$$

  where F_p is the flux from the planet;

- contribution from the star:

$$N_* \approx \sum_j \sum_k A_j A_k \cos(\phi_j - \phi_k) \bar{B}_{*jk}, \tag{2.14}$$

  and if the star brightness is distributed over a uniform circular disk

$$\bar{B}_{*jk} = 2F_* J_1 \left(\frac{2\pi b_{jk}\theta_*}{\lambda}\right) \Big/ \frac{2\pi b_{jk}\theta_*}{\lambda}, \tag{2.15}$$

  where F_* is the stellar flux corresponding to wavelength $\Delta\lambda$, J_1 is the first kind of Bessel function and θ_* is the stellar angular diameter;

- contribution from the exo-zodiacal dust emission

$$N_{EZ} \approx \sum_j \sum_k A_j A_k \cos(\phi_j - \phi_k) \bar{B}_{EZjk}; \tag{2.16}$$

- contribution from the local zodiacal dust:

$$N_{LZ} = B_{LZ} \sum_j A_j^2 \Delta\Omega_j, \tag{2.17}$$

  where Ω_j is the effective solid angle of the collector beam pattern. The above expression indicates that the local zodiacal dust is a uniform and incoherent foreground source of photon, only depending on the amplitudes.

It is also possible to define the geometrical leakage N_g as the refers to the portion of the sky brightness distribution that "escapes" through the ideal instrument, excluding the planetary signal N_p[17]:

$$N_g = N_o - N_p = \sum_j \sum_k A_j A_k \cos(\phi_j - \phi_k)(\bar{B}_{*jk} + \bar{B}_{EZjk}) + B_{LZ} \sum_j A_j^2 \Delta\Omega_j \tag{2.18}$$

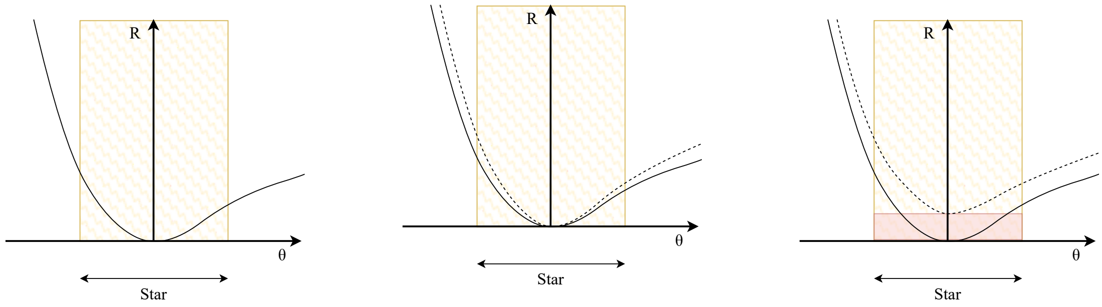

(a) Geometric leakage

(b) Geom. leakage perturbations

(c) Null floor perturbations

Figure 2.8: Schematic illustration of different contributions to the photon rate. R is the response of the interferometer and θ represents the angular coordinate (Figure 2.6). The yellow shading corresponds to the diameter of the target star.

Figure 2.8 shows a schematic representation of the various contributions to the detected photon rate at the output of a nulling interferometer[52]. In Figure 2.8a the enclosed area under the curve shows the geometric leakage of the star through the interferometer. Figure 2.8b shows the first-order fluctuation (dashed line) in phase, amplitude, and collector separation which preserve the on-axis null but lead to perturbations in the geometric leakage. Figure 2.8c shows the second-order fluctuations (dashed line) which give rise to perturbations in the null floor.

Another key parameter for characterizing a nulling interferometer is the geometric nulling ratio G, and its associated rejection factor ρ_g, defined as the inverse of the nulling ratio[17]:

$$G = \frac{N_g}{2F_* A^2} \qquad \rho_g = \frac{1}{G} = \frac{2F_* A^2}{N_g} \tag{2.19}$$

The nulling ratio represents the ratio of transmitted flux to the initial flux at the beam-combiner input (accounting for flux from both telescopes).

Chapter 3

Optical design

In this chapter the optical design of one arm of the nulling interferometer is presented. First of all, the main aspect of the methodology used for the design and analysis are introduced. It follows the sizing of the instrument components and the optical design performed with CODE V software for one branch of the nulling interferometer. Nominal and perturbed conditions are analysed, implementing a Monte Carlo simulation to apply the tolerances to the system. Finally the optical delay line is added in order to obtain the desired phase shift.

3.1 Methodology

Figure 3.1 shows the methodology adopted for the optical design.

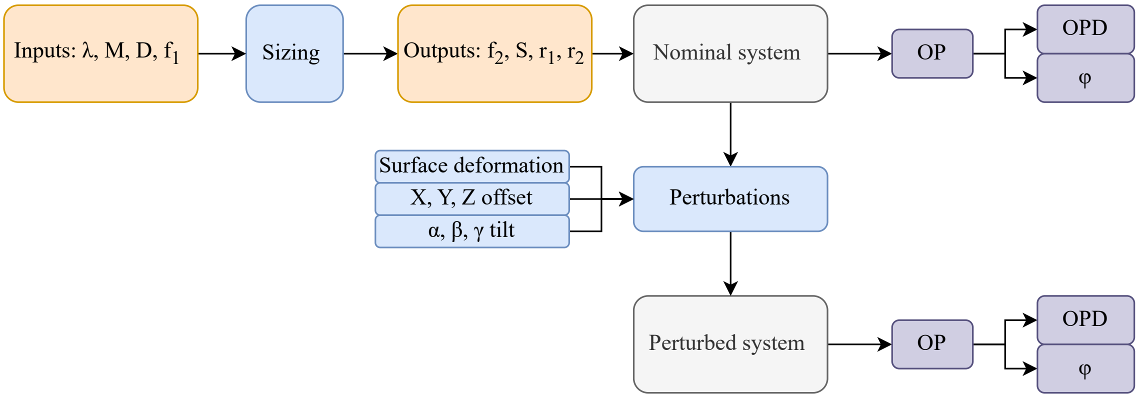

Figure 3.1: Block diagram of the methodology adopted for the optical design of one branch of the nulling interferometer.

The top-left part of the diagram establishes the starting point, the baseline configuration of the system without any imperfections. From the inputs listed, namely the wavelength λ, the magnification M, the aperture diameter D and the focal length of the primary mirror f_1, it is possible to retrieve the outputs for the optical design. These are fundamental parameters that define how the optical system is expected to behave in its ideal state, the nominal configuration.

Throughout the discussion, in order to better present the following steps, a simple configuration is considered where the optical system is a perfect flat lens. After the validation of the presented methodology for the simple system, the whole procedure can be applied to a single arm of the nulling interferometer.

Then, the diagram transitions into the perturbed system. Here, a set of perturbations is introduced to the nominal model, simulating real-world imperfections and misalignments. These are categorized primarily into:

- Surface deformation, which refers to any warping or structural imperfection in the optical surfaces (lenses, mirrors, etc.).

- Positional offsets in X, Y, and Z directions (translating components along the three spatial dimensions).
- Tilts in angular orientations, designated as α, β, γ corresponding to rotations around the respective axes.

These perturbations reflect what typically happens during assembly, handling, or operational use of an optical system. In fact no system is ever perfectly aligned or manufactured. The diagram shows these as feeding into the system, affecting the performance and causing deviations in optical parameters.

On the right of the diagram, it is possible to see three critical parameters: OP (Optical Path), OPD (Optical Path Difference), and φ (phase). These are key diagnostic quantities in optical analysis.

- OP is the length a light beam travels through the system and it is sensitive to physical and geometrical variations.
- OPD measures the deviation in this path relative to the nominal path, which is particularly important in interferometry and wavefront sensing.
- φ, the phase, captures changes in the light's phase front due to the combined effects of all the above perturbations.

A comparative analysis between nominal and perturbed systems is therefore performed. By examining how these parameters differ between the two conditions, one can infer the system's sensitivity to specific perturbations. In particular, a Monte Carlo simulation is used to apply the tolerances to the system.

3.2 Sizing

Considering a confocal system, as represented in Figure 3.2, the sizing of one arm of the interferometer is performed taking as inputs the values presented in Table 3.1. In particular, the value of the wavelength is set to 10 µm, since the region of interest is the infrared domain. The chosen value for the magnification is 20, which results from a trade-off between several design factors[16]. The other two inputs, namely the aperture diameter and the focal length of the primary mirror are compatible with the new ESA mission proposition[7].

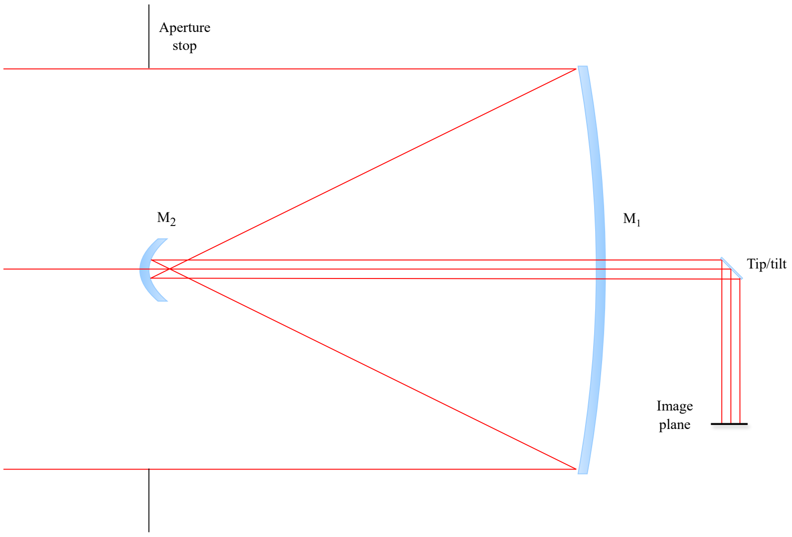

Figure 3.2: Schematic illustration of the confocal system representing one arm of the interferometer. The main represented components of the simplified system are the aperture stop, the primary mirror M_1, the secondary mirror M_2, the tip/tilti mirror and the image plane.

Inputs	$\boldsymbol{\lambda}$ [µm]	**M**	**D** [cm]	$\boldsymbol{f_1}$ [cm]
Value	10	20	250	300

Table 3.1: Inputs for the sizing, namely the wavelength λ, the magnification M, the diameter D and the focal length of the primary mirror f_1.

The relation linking the presented inputs to the outputs are as follows[80]:

$$M = \frac{f_2}{f_1} \qquad S = f_1 + f_2 \qquad f_i = \frac{r_i}{2}, \tag{3.1}$$

where $i = 1, 2$ represent the index related to the mirror, respectively primary or secondary mirror. The results are presented in Table 3.2.

Outputs	$\boldsymbol{f_2}$ [cm]	$\boldsymbol{S}$ [cm]	$\boldsymbol{r_1}$ [cm]	$\boldsymbol{r_2}$ [cm]
Value	15	315	600	30

Table 3.2: Output of the sizing, namely the focal length of the secondary mirror f_2, the size of the optical system S, the radii of curvature of both the primary and secondary mirror r_1 and r_2.

Figure 3.3 shows the variation of the size of the optical system S, or confocal optic size, with respect to the focal length of the primary mirror. A trade off is necessary in order to have a compact yet well performant system.

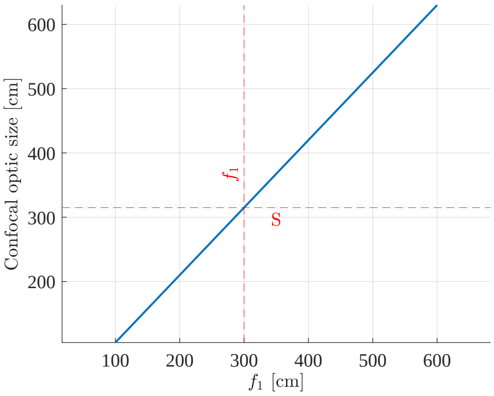

Figure 3.3: Linear variation of the confocal optic size with respect to the focal length of the primary mirror. The red dashed lines represent the values S and f_1 of the chosen system.

3.3 Tool validation

In order to validate the methodology, the procedure is first applied to a simple system, composed of the aperture stop, the optical system and the image plane. Subsequently, the procedure is applied to the interferometer arm system. A macro-PLUS program has been developed and then implemented in CODE V software with the aim to retrieve the optical path and the X and Y position of the rays. The output are then elaborated with MATLAB software.

3.3.1 Simple lens system

A grid of equidistant points has been created in MATLAB in order to form a circle of radius 1.25 m, equal to the aperture diameter of the considered telescope. These points correspond to the rays in a plane perpendicular to the wavefront at the aperture stop. The distance between the points has been set at 1.5 cm resulting in 21804 rays considered, each having an X and Y coordinate.

The grid is then used in a macro-PLUS program implemented in CODE V in order to retrieve the optical path for each ray in the image plane. The code is detailed in Appendix A.1. The optical path difference is then computed using Equation 2.2.

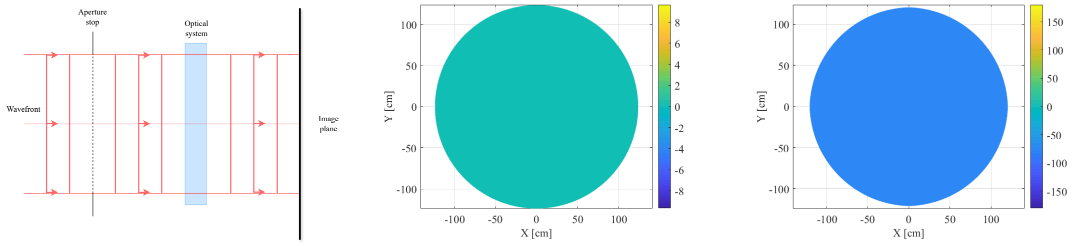

(a) Wavefront flat lens (b) OPD flat lens (c) Phase flat lens

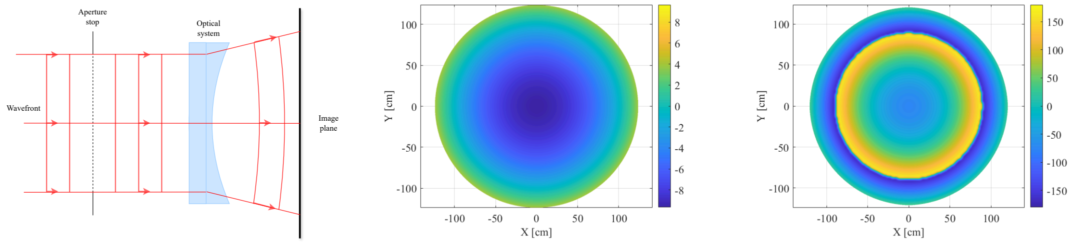

(d) Wavefront concave lens (e) OPD concave lens (f) Phase concave lens

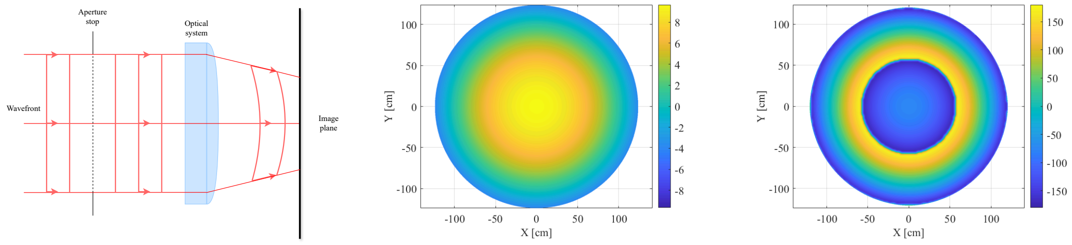

(g) Wavefront convex lens (h) OPD convex lens (i) Phase convex lens

Figure 3.4: Wavefronts representation, optical path difference in µm and phase distribution deg of the nominal configuration (Figure 3.4a, 3.4b and 3.4c) and the perturbed configuration considering a concave lens (Figure 3.4d, 3.4e and 3.4f) and a convex lens (Figure 3.4g, 3.4h and 3.4i). In the first case the optical system in this simple case is represented by a simple perfect lens without any curvature.

Considering a nominal configuration where no perturbation is applied, the wavefronts remain perfectly parallel to each other and to the image plane, as shown in Figure 3.4a. In particular, Figure 3.4b illustrates the measured optical path difference, which is zero everywhere, as expected.

However, taking into account a perturbed configuration, as can be seen in Figure 3.4d, the wavefronts are no longer parallel, resulting in a difference in the optical path, as shown in Figure 3.4e. The more external rays have in fact a greater optical path difference with respect to the central rays, since the curved lens deviates their paths. Similar considerations can be made for the case of a convex lens, as shown in Figure 3.4g and 3.4h. In this case, the more external rays are characterised by a shorter optical path difference with respect to the central rays.

Figures 3.4c 3.4f and 3.4i show the phase distribution, which is line with the behaviour of the optical path, since the two quantities are strictly related, as already pointed out in Equation 2.4.

3.3.2 Interferometer arm system

Optimisation

Starting from the confocal system, presented in Figure 3.2 an optimisation is performed using CODE V software. The optimisation aims to improve the optical design minimising aberrations, maximising performance and meeting mechanical constraints by automatically adjusting system parameters.After setting up the optical system, the variables are defined, namely the parameters which CODE V is allowed to change in order to optimise the system. Then, a macro-PLUS program has been implemented in order to perform the optimisation, which is based on the command `aut;go` predefined in the software and defined constraints to ensure design feasibility. Since the system is symmetric, the optimisation does not change the configuration, as expected.

In order to obtain more precise results, the distance between the points has been set at 1 cm resulting in a number of rays of 49077. The map of the optical path difference of the nominal configuration is presented in Figure 3.5a. As it can be seen, following the same reasoning presented for the nominal configuration of the simple system, the optical path difference is zero everywhere.

Surface deformation

In the first case the perturbation derive from a surface deformation applied to the system. The goal is to have the minium optical path difference considering the perturbations, in order to guarantee the right functioning of the optical system.

Figure 3.5b shows the perturbed configuration with a surface deformation of $\lambda/10$ applied to the system. In particular, the interested surfaces are the primary mirror and the tip/tilt mirror This value represent a realistic assumption considering the application. A gradient effect is visible in the image which is the result of a perturbed wavefront.

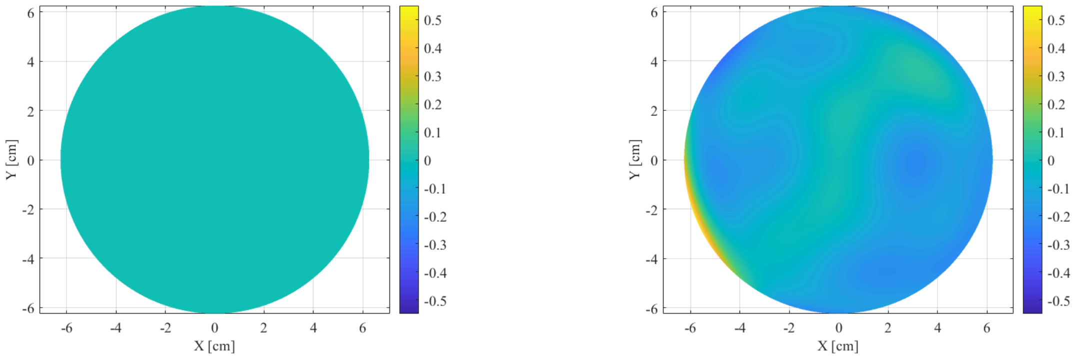

(a) Nominal

(b) Perturbed by surf. def.

Figure 3.5: Optical path difference in µm of the nominal configuration and perturbed configuration by a surface deformation of $\lambda/10$.

Offset and tip/tilt

In this case, the perturbation are represented by tolerances applied to the system which cause an optical path difference to be detected. In order to study the behaviour of the perturbed system, a Monte Carlo simulation has been performed.

In particular, a normal distribution of 100000 values, with standard deviation equal to 0.3 and mean value equal to 0, has been obtained using a MATLAB script and then used to apply the tolerances to the system. The assumed distribution for applying tolerances in this analysis is normal (Gaussian), which reflects typical manufacturing variations. A macro-PLUS program has been implemented to impose the tolerances to the system, in particular to the distance between the mirrors, to the radius of curvature, to the X, Y, Z position and to the tilt angles of the mirrors. Then, an iterative process is implemented, in which the methodology used to apply the tolerances is summarised by the following formula:

$$p = n + vt \tag{3.2}$$

where p is the parameter to vary, n is its value in the nominal configuration, v is a randomly picked value from the previously defined nominal distribution and t is the tolerance applied. A more detailed explanation of the macro-PLUS program can be found in Appendix A.2.

The values of t selected are realistic and in line with the application in order to validate the methodology presented, more precise values will derive from the mechanical design of the nulling interferometer described in the following Chapter. In particular, the chosen values of t are reported in Table 3.3.

Surface	**THI** [µm]	**RDY** [µm]	**XDE** [µm]	**YDE** [µm]	**ZDE** [µm]	**ADE** [arcmin]	**BDE** [arcmin]	**CDE** [arcmin]
M$_1$	± 0.5	± 0.5	± 0.5	± 0.5	± 0.5	± 0.003	± 0.003	± 0.003
M$_2$	± 0.5	± 0.5	± 0.5	± 0.5	± 0.5	± 0.003	± 0.003	± 0.003
Tip/Tilt	± 0.5	± 0.5	± 0.5	± 0.5	± 0.5	± 0.003	± 0.003	± 0.003

Table 3.3: Values of the tolerances applied to each surface of the optical system. RDY is the radius of curvature with respect to Y axis; XDE, YDE, ZDE are the decentres with the respect to X, Y and Z axis; ADE, BDE, CDE are the tilt angles with respect to X, Y and Z axis.

Figure 3.6 shows the optical path difference of the nominal and perturbed system. The colorbar has been readapted in order to better compare the configurations. In particular, Figure 3.6c shows the optical path difference of the maximum perturbed configuration with a maximum OPD of 2.11 µm. The difference in the optical path is significantly higher than the previous cases, presented in Figure 3.5.

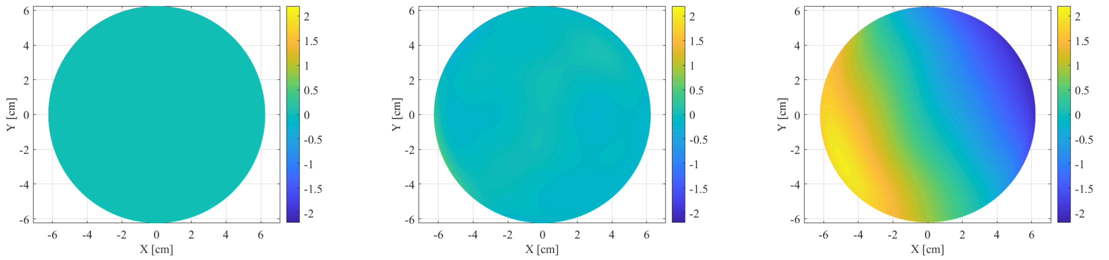

(a) Nominal (b) Perturbed by surf. def. (c) Max perturbed by dec./tilt

Figure 3.6: Optical path difference in µm of the nominal, perturbed by surface deformation and maximum perturbed by decentre or tilt over 50 iterations of one arm of the interferometer.

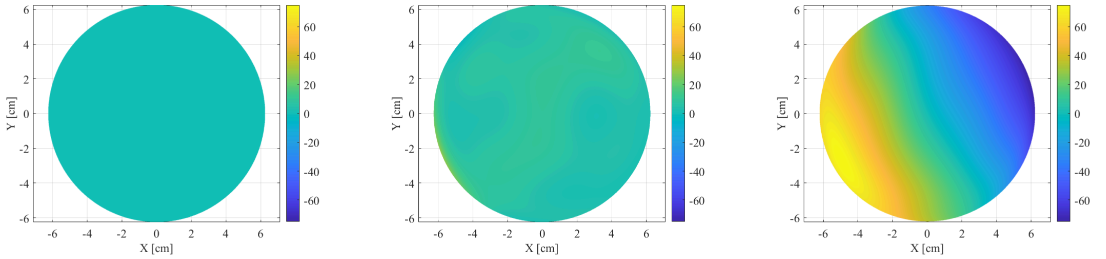

(a) Nominal (b) Perturbed by surf. def. (c) Max perturbed by dec./tilt

Figure 3.7: Phase distribution in deg of the nominal, perturbed by surface deformation and maximum perturbed by decentre or tilt configuration over 50 iterations of one arm of the interferometer.

Furthermore, following the same procedure as in Section 3.3.1, the phase distribution has also been computed. The nominal, perturbed by surface deformation and maximum perturbed configurations are shown in Figure 3.7. It is possible to notice that, since the phase distribution is strictly related to the optical path, the plots are similar to the one presented in Figure 3.6.

Figure 3.8 and 3.9 display the optical path difference and the phase distribution for 15 randomly picked simulations where different values of tolerances are applied.

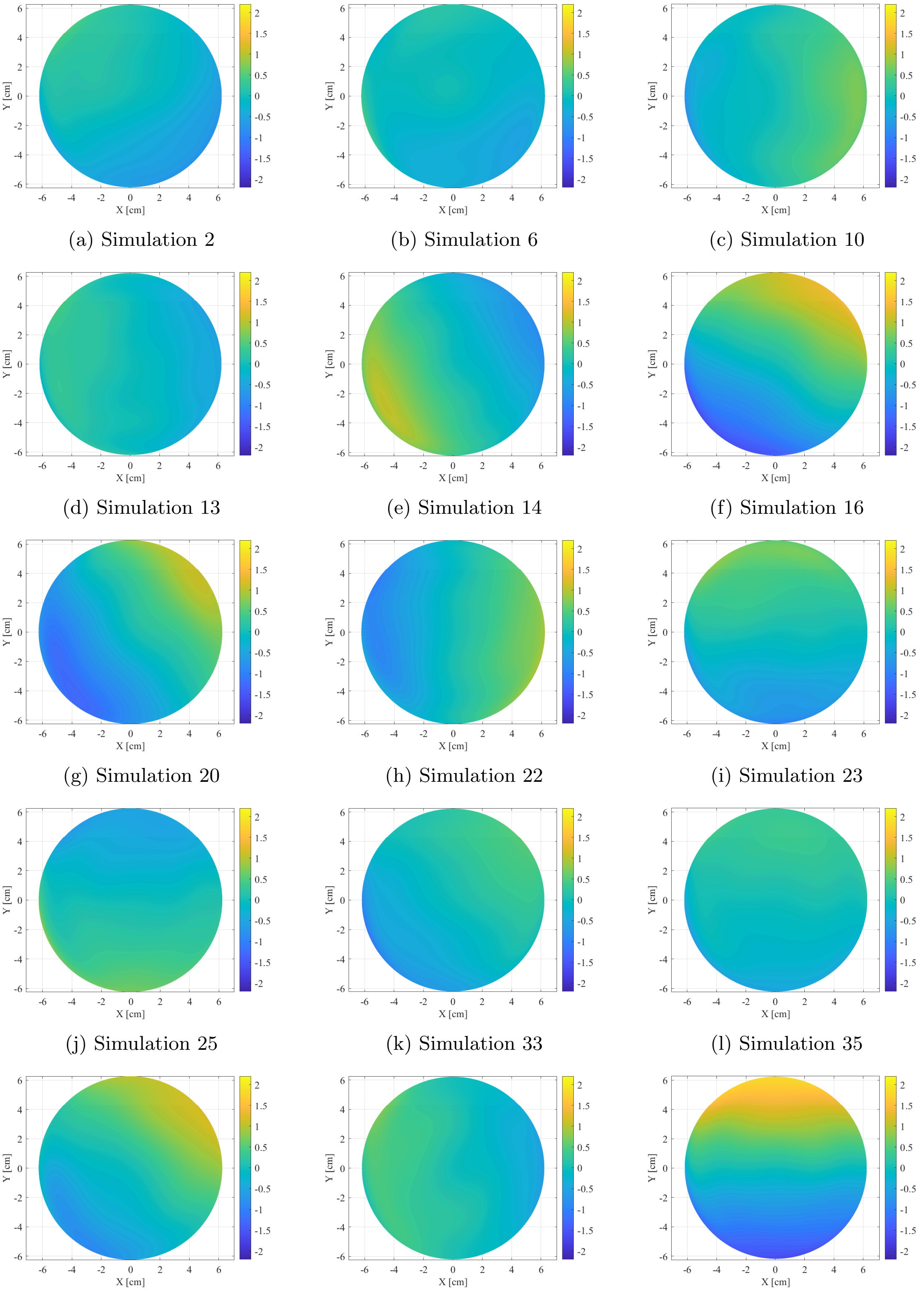

(a) Simulation 2 (b) Simulation 6 (c) Simulation 10

(d) Simulation 13 (e) Simulation 14 (f) Simulation 16

(g) Simulation 20 (h) Simulation 22 (i) Simulation 23

(j) Simulation 25 (k) Simulation 33 (l) Simulation 35

(m) Simulation 39 (n) Simulation 40 (o) Simulation 48

Figure 3.8: Optical path difference in µm for 15 randomly picked simulations over 50 total simulations.

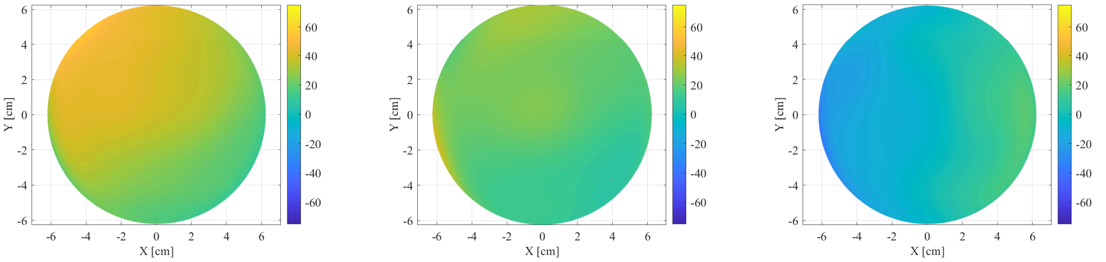

(a) Simulation 2 (b) Simulation 6 (c) Simulation 10

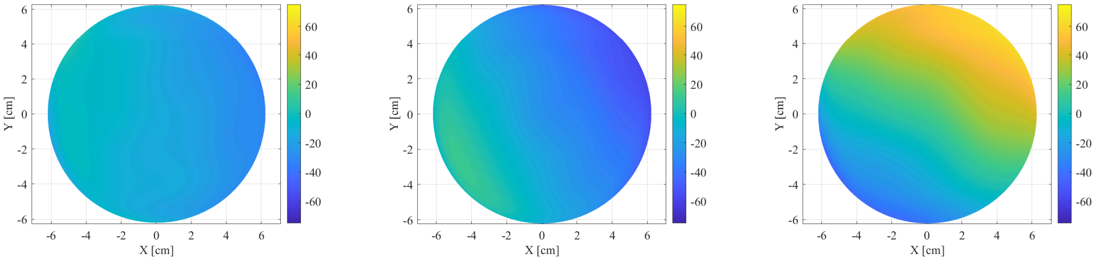

(d) Simulation 13 (e) Simulation 14 (f) Simulation 16

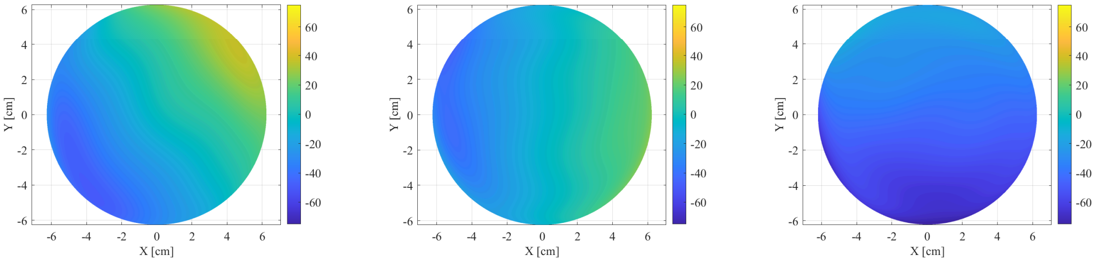

(g) Simulation 20 (h) Simulation 22 (i) Simulation 23

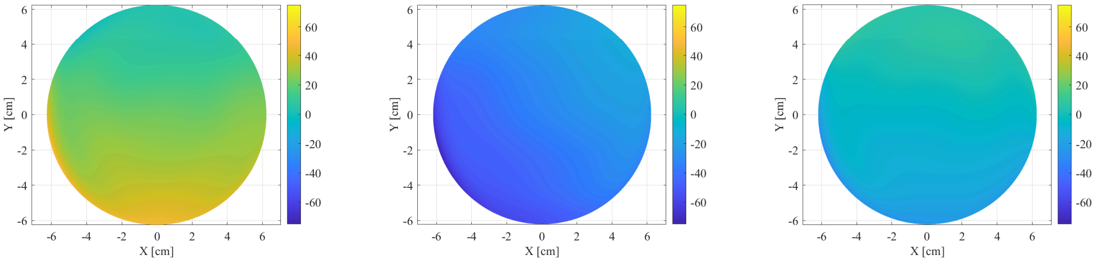

(j) Simulation 25 (k) Simulation 33 (l) Simulation 35

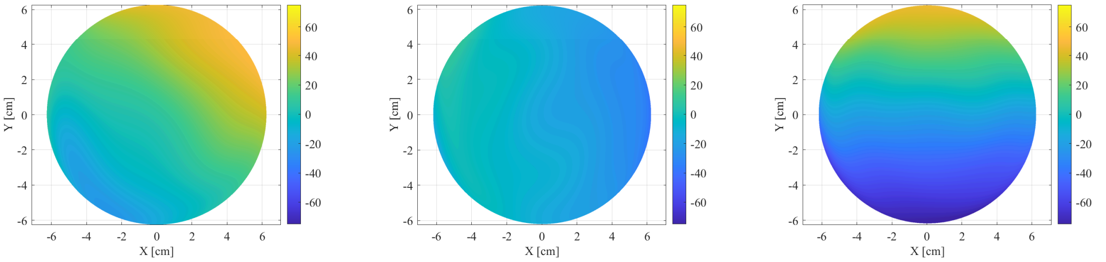

(m) Simulation 39 (n) Simulation 40 (o) Simulation 48

Figure 3.9: Relative phase distribution in deg for 15 randomly picked simulations over 50 total simulations.

3.3.3 Statistical analysis

In order to evaluate the robustness of the optical design under real-world variability a statistical analysis has also been performed. The results are analysed through key statistical measures, such as the mean deviation, standard deviation and root mean square error (RMSE).

Figure 3.10a shows the mean of the optical path difference over 50 simulated tolerance configurations. The values fluctuate around zero, ranging from approximately -1.2 to +1.2 µm. The system is well-centred, meaning it is likely robust against systematic drifts. The maximum value reached is 1.225 µm.

The standard deviation of the OPD is represented in Figure 3.10b, showing how the OPD values are spread out within each simulation configuration. Most configurations have standard deviations between 0.2 - 1.2 µm. There is notable variability in standard deviation across simulations, suggesting some tolerance combinations lead to more unstable or less uniform wavefronts. The maximum value reached is 1.0714 µm.

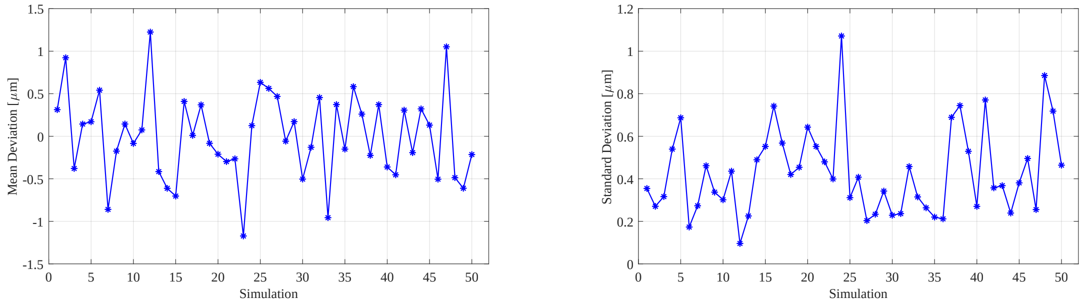

(a) Mean deviation

(b) Standard deviation

Figure 3.10: Mean and standard deviation of the computed OPD over 50 iterations.

Furthermore, the Root Mean Square Error (RMSE) of the X and Y position of the rays in the image plane has been computed and the results are presented in Figure 3.11. Both X and Y coordinate RMSE values show fluctuations across the 50 simulations. This indicates that the precision of the system's output coordinates varies considerably depending on the specific combination of tolerances applied in each simulation run. The X coordinate RMSE (red line) generally exhibits higher values and more pronounced peaks compared to the Y coordinate RMSE (blue line). This suggests that the X coordinate is more sensitive to the applied tolerances, leading to larger errors, or that the system's design or alignment is more susceptible to variations in the X-direction.

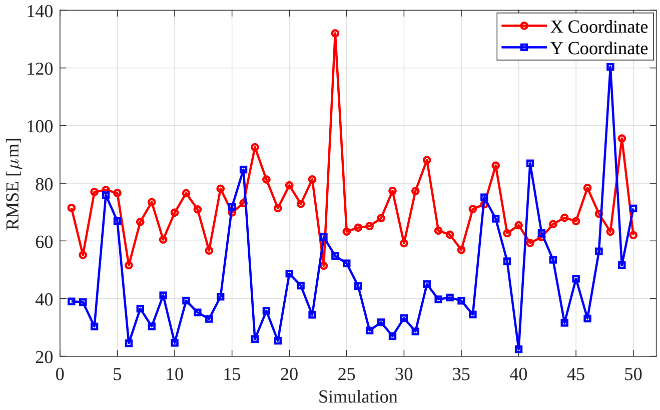

Figure 3.11: Root Mean Square Error (RMSE) of the X (red line) and Y (blue line) position of the rays in the image plane over 50 iterations.

Figure 3.12 displays the distribution of optical path difference for each iteration of the simulation. For most iterations, the median OPD is consistently negative, indicating that under the randomly applied tolerances, the optical system exhibits a negative OPD. The range of values of the OPD represented by the box itself shows the spread of the middle 50 % of the data, and it appears relatively consistent across many iterations, suggesting a similar level of variability in OPD within those iterations. Several iterations, particularly around simulation 1, 10, 13, 27, 30, and 33,

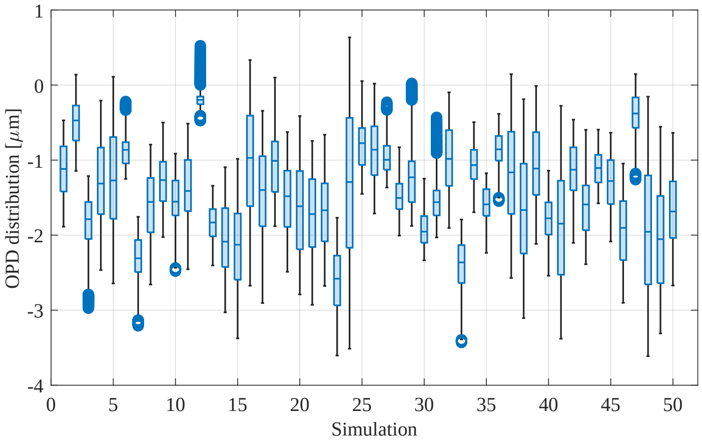

Figure 3.12: Boxplot representation of OPD across 50 iterations. The central line in each box represents the median, the box edges indicate the interquartile range (25th to 75th percentile), and the whiskers extend to the most extreme data points not considered outliers.

show prominent outliers (individual points beyond the whiskers). These outliers, especially the ones near zero or positive OPD values, suggest that in some simulation runs, the optical system deviates significantly from the typical negative OPD distribution. This could indicate specific tolerance combinations leading to unusual OPD behaviour.

3.4 Optical Delay Line

The previously defined methodology is valid for each branch of the four apertures nulling interferometer. Moreover, in order to have the desired results in terms of phase shift, as mentioned in Chapter 2, an achromatic phase shifter is necessary. However, in order to perform the preliminary mechanical design, delay lines have been added to the system in order to obtain the desired phase at the beam combiner. It is important to highlight that the following discussion is valid for a single wavelength and not for a range of wavelengths.

A MATLAB script has been implemented in order to compute the required optical path length adjustments for the four-arm interferometric system. The code simulates the calibration or design steps where physical path lengths are tuned to produce desired relative phases, ensuring coherence and interference accuracy in the optical setup. The main objective is to determine the additional path length x_i that must be added to each optical arm so that the total optical path corresponds to a target phase ϕ_i, while also ensuring that the total path length exceeds a specified minimum optical path. The phase shift is introduced by adjusting the optical path according to the relation between physical distance and optical phase.

The interferometric system consists of four optical paths or arms. Each arm has a base optical path length a_i, derived from mechanical design considerations. For each arm i, the code performs the following steps:

- Compute phase-equivalent optical path: the phase ϕ_i is first converted into a physical path length using:

  $$OP_{\phi_i} = \frac{\lambda \phi_i}{2\pi} \tag{3.3}$$

  this quantity represents the fraction of a wavelength that corresponds to the desired phase shift.

- Ensure minimum total optical path: to satisfy both the phase condition and a minimum total optical path constraint OP_{min}, the number of full wavelengths n_i that must be added is calculated as:

  $$n_i = f_i \left[\frac{OP_{min} - OP_{\phi_i}}{\lambda} \right] \tag{3.4}$$

where f_i is a scaling factor, used to fine-tune or account for additional real-word fabrication tolerances or dispersion effects. This ensures that the total optical path after adjustment is:

$$OP_{tot_i} = OP_{\phi_i} + n_i\lambda \tag{3.5}$$

- Determine path length adjustment: the required extension x_i to the physical length of arm i is then simply:

$$x_i = OP_{tot_i} - a_i \tag{3.6}$$

- Phase verification: to verify that the andjustment leas to the correct phase, the code calculates:

$$\phi_{actual_i} = \left(\frac{a_i + x_i}{\lambda} 2\pi\right) \mod 2\pi \tag{3.7}$$

  this checks that the resulting optical phase is equivalent (modulo 2π) to the target ϕ_i, validating the accuracy of the compensation.

In this case the chosen baseline is of 10.50 m, which is compatible with the internal dimensions of the Ariane 6 fairing[5]. Therefore, due to optical and mechanical design considerations, the minimum total optical path constraint has been set to 12 m.

Table 3.4 summarises the final values of the total optical path and the target phase shifts deduced from the mathematical modelling of F. De Bortoli[26].

	Total optical path [m]	**Phase** [deg]	$\tilde{n}$
Arm 1	14.2200007500	270	0.2200007500
Arm 2	14.6400005000	180	0.6400005000
Arm 3	14.6400002500	90	0.6400002500
Arm 4	14.2200000000	0	0.2200000000

Table 3.4: Total optical path and desired phase values[26] for each arm of the nulling interferometer; $\tilde{n}$ represents the number of full wavelength subtracted by the integer 14.

Chapter 4

Mechanical design

Once the optical design has been performed and the presented results are satisfying, the mechanical design can be addressed. The aim of this chapter is to introduce the requirements of the instruments, mainly related to the launcher and the objectives of the mission for which the instrument should be used. The CAD model is then addressed, for the two configurations, namely the telescopic and foldable secondary mirror configuration, highlighting possible advantages and disadvantages for the two solutions. The mass estimation of the instrument is also performed for the two presented configuration. Subsequently, the tolerances are retrieved and applied to the system, resulting in the need for a compensator which will be further addressed in the following chapter. Finally an overview of actuators for space applications is presented.

4.1 Requirements and objectives

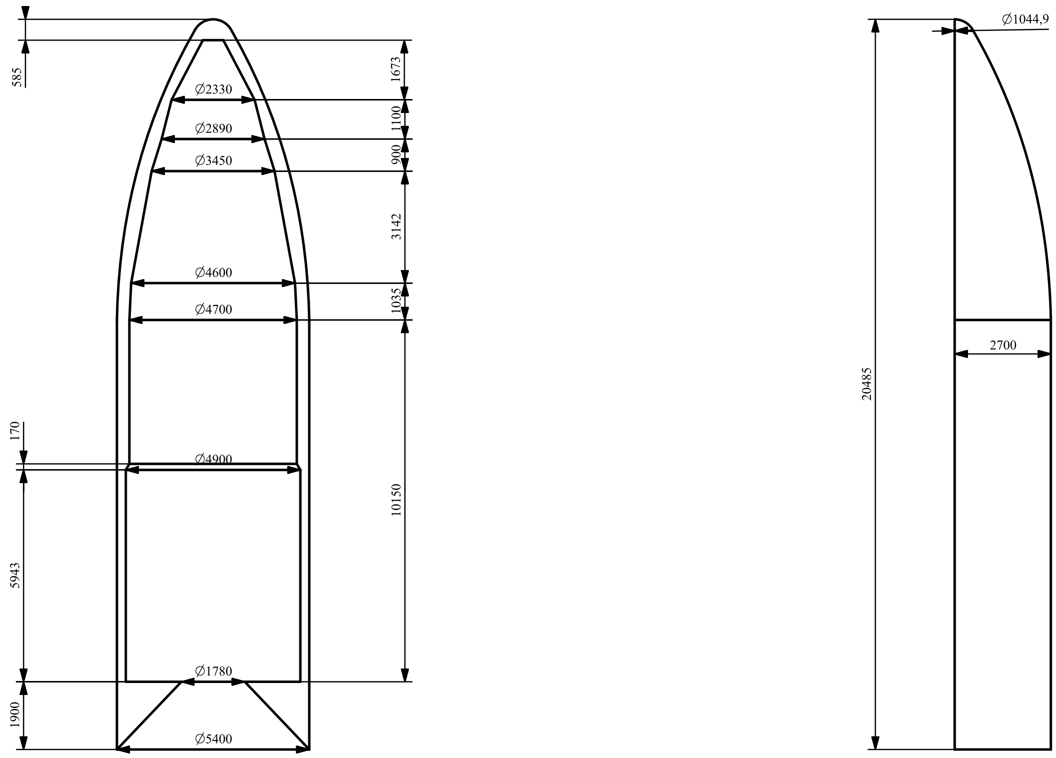

Figure 4.1: Dimensions in mm of the Ariane 6[5] fairing.

Following the new propositions of ESA, regarding the simplification of the number of the involved spacecraft[7], the aim is to design an interferometer compatible with the payload with an Ariane

6 launch. The main limiting factors of a nulling interferometer to constrain the geometry of the payload are the baseline, the number of telescopes (which in this case is fixed to 4), and their sizes.

As already pointed out in Chapter 1, different configurations are possible, depending on the number of the apertures and their positions. A linear array was believed to be the best configuration in this case, in terms of deployment and arrangement inside the launcher. Figure 4.1 shows the dimension of the Ariane 6 fairing. The nulling interferometer size must be compatible with the presented dimensions, giving constraints on the baseline and making deployment the only solution possible.

4.2 Complete nulling interferometer configuration

This section presents the CAD model of the four apertures nulling interferometer. The optical design from CODE V software has been converted in a `.step` file and exported to NX software in order to perform the mechanical design. Four apertures have been designed, with the corresponding holding structure. Two possible deployment configuration will be described: the first one in based on a telescopic structure, while the second one is realised with a foldable secondary mirror.

4.2.1 Telescopic configuration

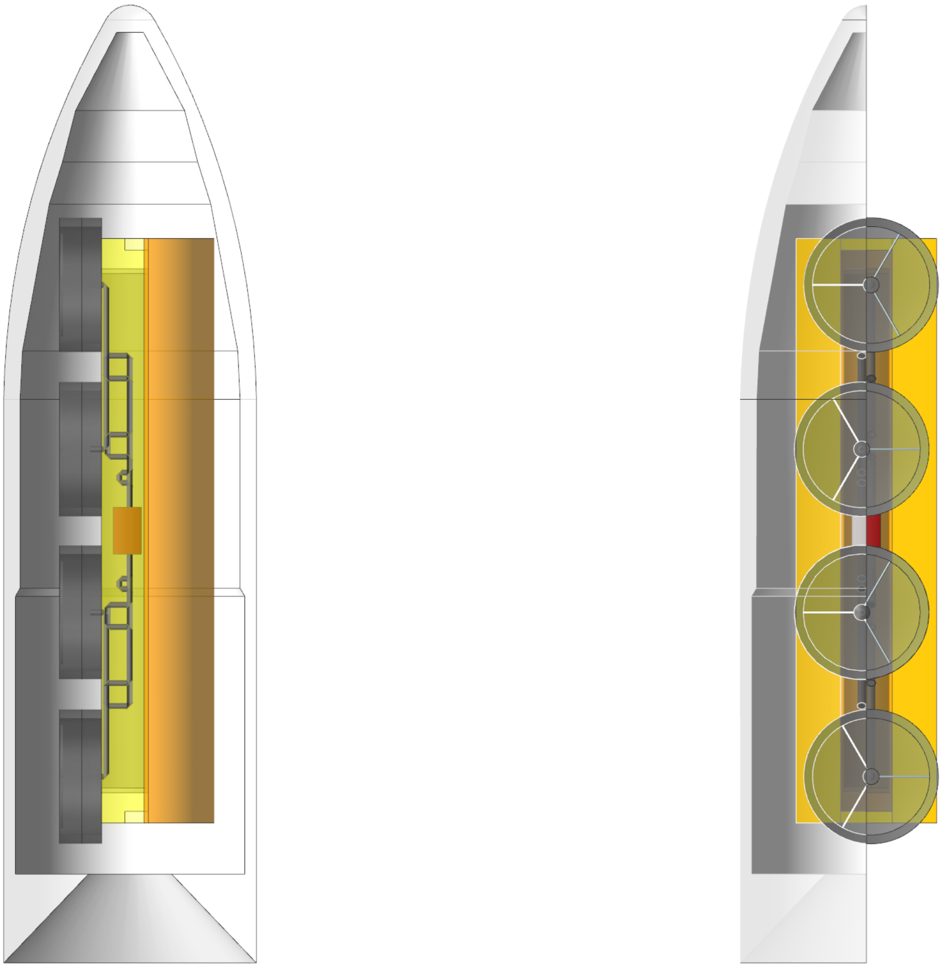

(a) Front view

(b) Top view

Figure 4.2: Front and top view of the CAD model of the undeployed configuration of the telescopic structure placed inside the Ariane 6 fairing.

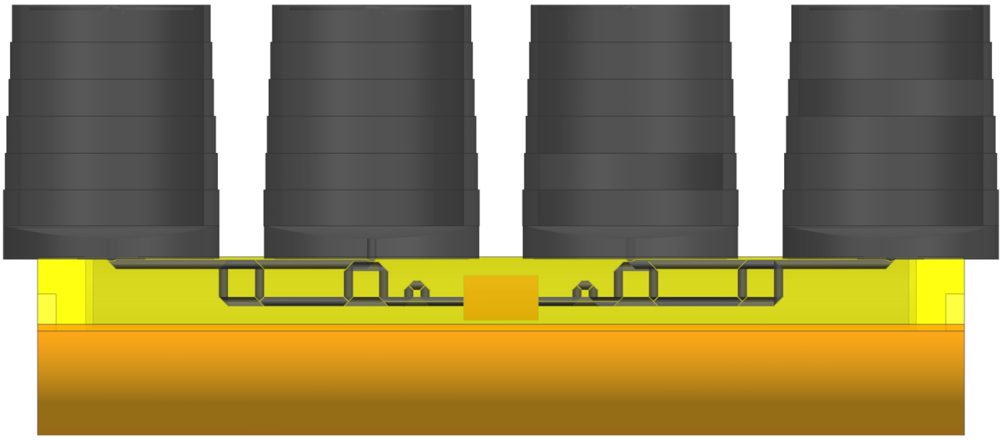

Figure 4.3: Front view of the deployed configuration of the telescopic strcture.

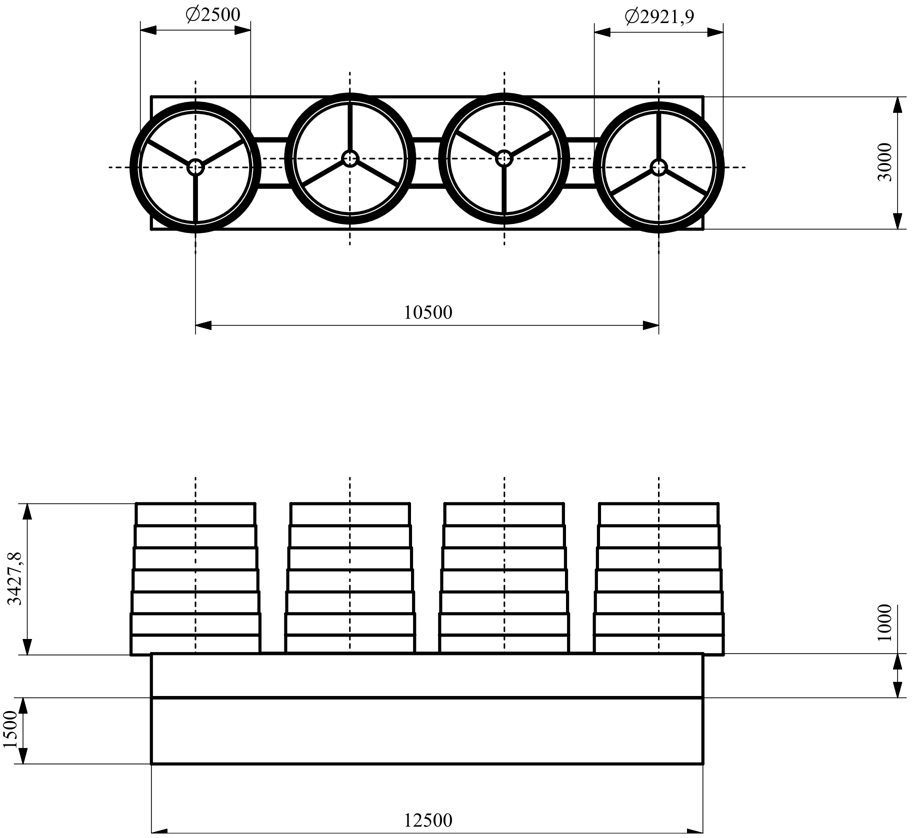

Figure 4.4: Draft of the CAD model of the deployed configuration of the telescopic structure. Dimensions in mm.

Figure 4.2 shows the front and top view of the CAD model related to the undeployed configuration of the telescopic structure. As is can be observed the design of the undeployed configuration respects the previously defined constraints, making it a valid possible solution. Figure 4.3 shows instead the deployed configuration, while Figure 4.4 presents the dimensions in mm.

4.2.2 Foldable secondary mirror

The second configuration presented is realised considering a foldable secondary mirror, following a similar principle as the James Webb Telescope[36]. Figure 4.5 shows the front and top view of the CAD model of the undeployed configuration. As before, the constraints are met and the configuration is considered valid.

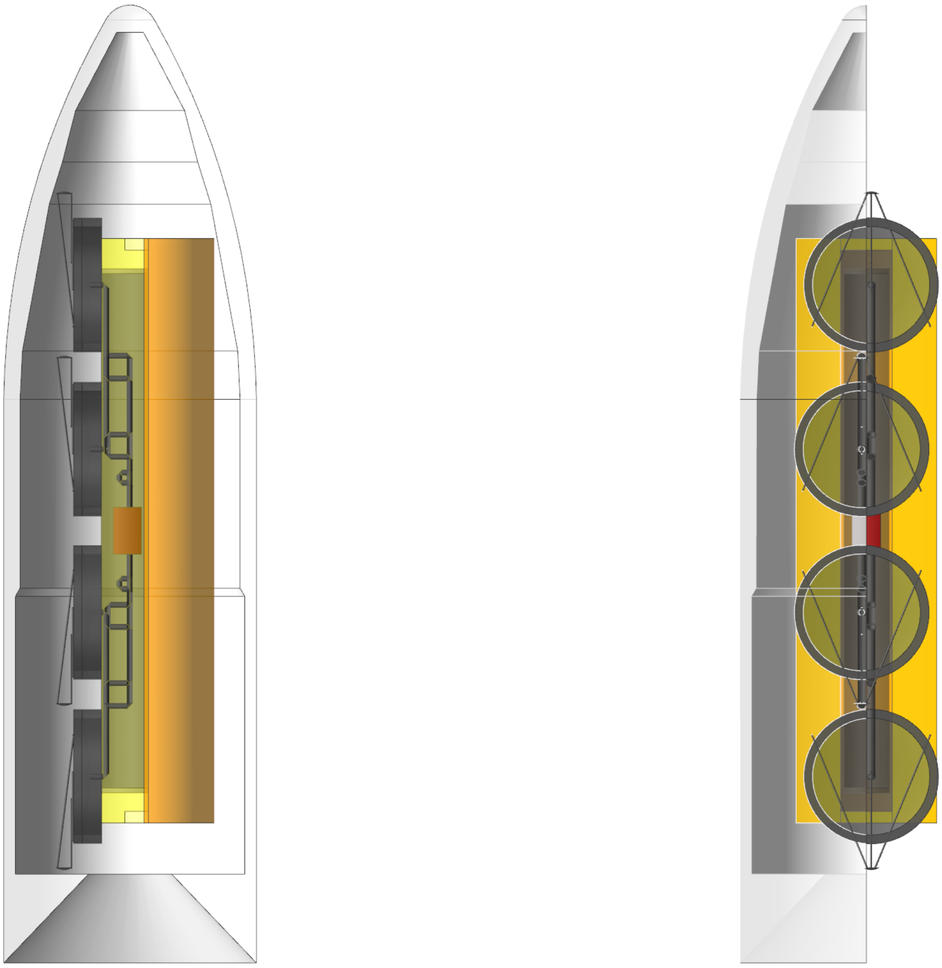

(a) Front view

(b) Top view

Figure 4.5: Front and top view of the CAD model of the undeployed configuration of the foldable mirror structure.

The deployed configuration is presented in Figure 4.7 and the dimension in mm are shown in Figure 4.7.

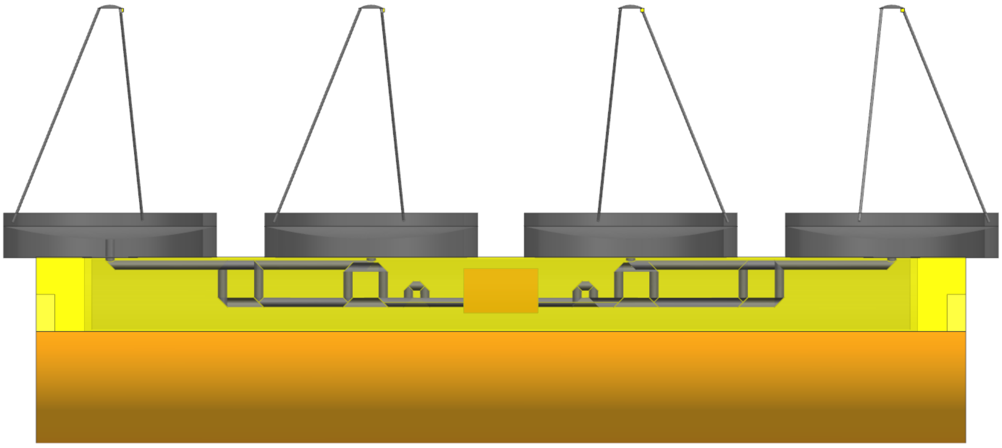

Figure 4.6: Front view of the CAD model of the deployed configuration of the foldable mirror structure.

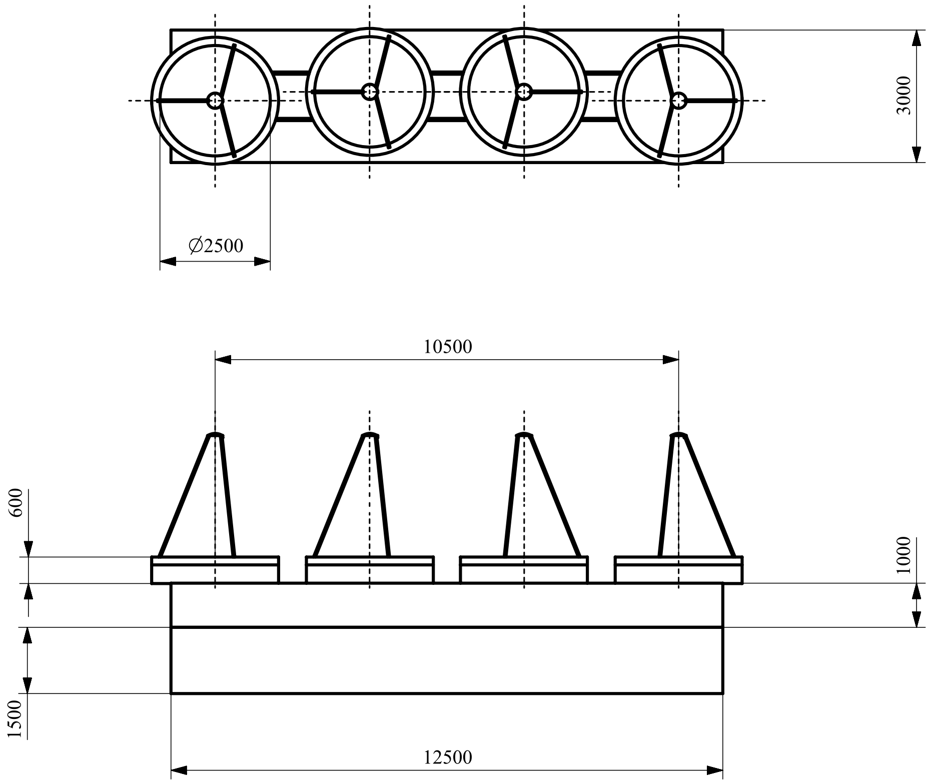

Figure 4.7: Draft of the CAD model of the deployed configuration of the foldable mirror structure. Dimensions in mm.

4.2.3 Comparison between the configurations

From Figures 4.2 and 4.5 the main components of the nulling interferometer are visible. Both configurations are represented with the respective delay lines and beam combiner and can visibly fit inside the Ariane 6 fairing. The telescopes are modelled with their respective holding structure, which differs only for the deployment mechanism. Since both configurations are valid, a trade off needs to be carried out considering the mass of the structure and potential advantages and disadvantages of both solutions.

Figure 4.8 shows the deployment mechanism for both the telescopic and the foldable secondary mirror configuration. It can be noticed that the deployment of the latter is more complex, since more mechanism are involved in the deployment increasing the risk and therefore the probability of failure.

However, Table 4.1 shows a comparison between the presented configurations, underling that each has unique features and the choice depends on mission goals, structural constraints, and risk tolerance.

In general, it can be stated that a telescopic structure is used to prioritise structural simplicity and stability, and the optical path can be accommodated. While a foldable secondary mirror is the best choice if there is the need to maximise optical performance in a compact stowed configuration but are willing to accept more deployment risk and complexity.

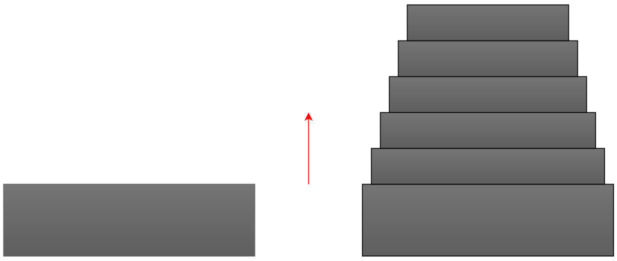

(a) Telescopic structure

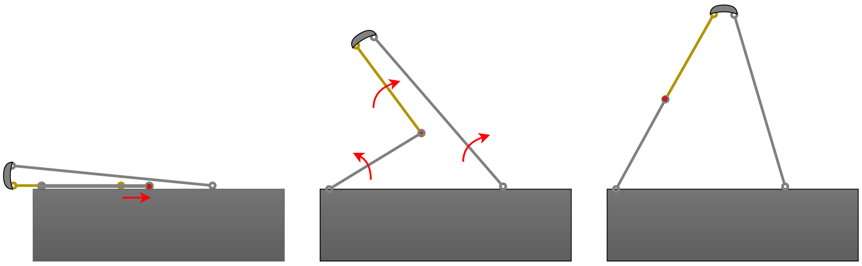

(b) Foldable mirror

Figure 4.8: Schematic representation of the two deployment mechanism both for the telescopic and the foldable mirror structure.

Feature	**Telescopic config.**	**Foldable mirror config.**
Stowage volume	Compact for structure	Very compact for optics
Complexity	Moderate	High
Alignment precision needed	Medium	Very high
Thermal stability risk	Moderate	High
Optical flexibility	Limited	High (longer focal lengths)
Reliability	Higher	Lower

Table 4.1: Comparison between the telescopic and foldable mirror configuration.

4.3 Mass estimation

The material selection for the structure of the telescope plays an important role in mass reduction. The main objectives are the mass minimization and the design of a structure able to survive the space environment as well as guarantee a high level of reliability. In fact, since cost minimization is an important aspect to take into account, the system must be tested before launch in order to prove the integrity of the structure during every phase of the flight, especially considering the mechanical vibrations, the wide range of temperatures and radiations that will characterize the instrument life.

Table 4.2 presents the chosen materials, their density as well as the volume and the resultant mass for the different components of the interferometer[72],[37]. It is important to underline that the latter represents an estimation of the mass. Several components have not be taken into account, such as the actuators and the sensors since they do not affect significantly the final result.

While, Table 4.3 shows the mass of the single telescope and of the four apertures interferometer for both configurations. It is possible to observe that the foldable mirror configuration presents a significantly lower mass.

Considering the presented application, in order to maximise the optical performance and minimise the mass of the nulling interferometer, the chosen solution is the foldable mirror configuration.

Component	**Material**	**Density** [kg/m^3]	**Volume** [m^3]	**Mass** [kg]
M$_1$	Zerodure	2500	0.054	135.5
M$_2$	Aluminum	2700	0.006	15
Other optics	Aluminum	2700	0.067	180.12
Telescopic structure	CFRP	1600	1.359	2175.5
Foldable mirror structure	CFRP	1600	0.954	1525.78

Table 4.2: Material, density, volume and mass estimation of the primary mirror M$_1$, the secondary mirror M$_2$ and other optical elements (such as the tip-tilt and the delay line mirrors) as well as the structure of the telescopic and foldable mirror configuration[72],[37].

Configuration	**Single telescope mass** [kg]	**Total mass** [kg]
Telescopic	2506.1	10024.5
Foldable mirror	1856.4	7425.6

Table 4.3: Mass estimation of the single telescope and of the 4 apertures interferometer for the telescopic and foldable mirror configuration.

4.4 Tolerances on the system

Tolerances defines the acceptable range of variation in dimensions, material characteristics, and alignment of components within an opto-mechanical system. Rather then simply being allowances for manufacturing imperfections, they play a crucial role in translating idealised designs into practical, functioning systems.

In particular, in opto-mechanical assemblies, such deviations can stem from numerous factors, such as machining errors, material flow, mounting-induced stresses or thermal expansion, all of which can contribute to optical aberrations and diminished system performance.

From the mechanical design and from thermal variations considerations it is possible to retrieve the real tolerances to apply to the system. Since the structure is made of CFRP, then thermal expansion will be much smaller than metals like aluminium, but directionally dependent due to anisotropy.

A perturbation of 1 µm µm was applied to the system to simulate realistic optical path fluctuations and assess the sensitivity of the nulling performance. This scale is appropriate given that it is comparable to the operational wavelength range and typical tolerances in nulling interferometry. It also reflects the mechanical precision of common actuators and helps characterize the system's robustness to minor alignment errors. While, regarding the tip/tilt, the choices have been taken following the work of S. Loiseau and S. Shaklan[55]. Table 4.4 shows the final values.

These perturbations combined with a surface deformation of $\lambda/10$, lead to a maximum optical path difference of 1.4 µm, which is significantly high for the considered application. Therefore, in order to minimize the optical path difference, guaranteeing the correct functioning of the instrument, a compensator is needed.

Surface	**THI** [µm]	**RDY** [µm]	**XDE** [µm]	**YDE** [µm]	**ZDE** [µm]	**ADE** [arcmin]	**BDE** [arcmin]	**CDE** [arcmin]
M$_1$	± 1	± 1	± 1	± 1	± 1	± 0.00093	± 0.00093	± 0.00093
M$_2$	± 1	± 1	± 1	± 1	± 1	± 0.0022	± 0.0022	± 0.0022
Tip/Tilt	± 1	± 1	± 1	± 1	± 1	± 0.0022	± 0.0022	± 0.0022

Table 4.4: Values of the tolerances applied to each surface of the optical system. RDY is the radius of curvature with respect to Y axis; XDE, YDE, ZDE are the offsets with the respect to X, Y and Z axis; ADE, BDE, CDE are the tilt angles with respect to X, Y and Z axis[55],[42].

The next chapter will address the impact of the compensator on the system, underling the improvements of the results.

4.5 Overview of actuators

An overview of actuators is presented in this section, with the aim of underlying their importance and define the ones compatible with the discussed application.

Actuators are crucial subsystems in space applications, operating various satellite platform and payload device. They must withstand challenging environmental conditions like extreme temperatures and vacuum, while meeting increasingly demanding performance requirements. Failure in actuators can have severe consequences for spacecraft operations.

They can be categorised into two main types: the conventional technologies (electric motors) and the new technologies (smart materials)[20].

- Conventional technologies (electric motors): the most common and mature technology for space actuators due to their heritage, performance and reliability. They are widely used for deploying spacecraft appendages (like solar arrays and antennas) and for pointing, scanning and optical adjustments in instruments. They include stepper motors (for deployment, pointing), brushless motors (for high speed), and brushed motors (if pressurised).
- New technologies (smart materials): increasingly being considered for future spacecraft applications that demand high precision, low mass, and long operational life. However, their widespread adoption faces challenges related to compatibility with existing spacecraft systems, radiation and contamination requirements, and the need for dedicated multidisciplinary design efforts for preliminary project phases. These new technologies include piezoelectric actuators, shape memory alloys and piezoelectric motors.

For high-precision optical applications in space, piezoelectric actuators are a mature and highly suitable technology[20].

A general block diagram regarding a single interferometer arm is presented in Figure 4.9, where the position of the different sensors and actuators are reported. In particular, in this analysis the OPD sensor and actuator will be chosen.

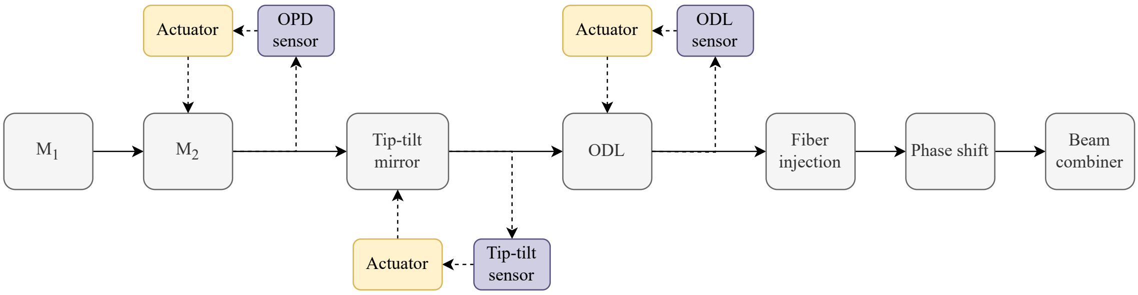

Figure 4.9: Block diagram of one telescope showing the position of the needed actuators and sensors.

Considering the application, an actuator of the precision of nanometers must be taken into account. The P-753 LISA (Linear Stage Actuators)[67] can be a good fit for the application of interest. Also the flexure-guided, lever-amplified PiezoMove P-601 actuators can be used, which are characterised by a highly precise, frictionless flexure guidance, a very high stiffness and excellent straightness of motion[25]. Table 4.5 shows their characteristic.

Finally, Figure 4.10 shows the block diagram of the methodology adopted so far in the discussion, presenting the various step covered and the anticipation of the compensator role. Two different compensators will be implemented, namely one based on the bisection method and one based on CODE V optimisation commands. Their impact on the performances of the system will be discussed in the next Chapter.

Actuator	Material	Int. sensor	Res.[nm]	Mass[kg]
P-601 PiezoMove Z-Actuator	Stainless steel	SGS	0.2-0.4	0.05-0.11
P-753 LISA Linear Actuator	Stainless steel	Capacitive	0.05-0.2	0.15-0.26

Table 4.5: Technical characteristics of the P-601 PiezoMove Z-Actuator and the P-753 LISA Linear Actuator Stage. In particular the material, the integrated sensor, the resolution and the mass are specified[25],[67].

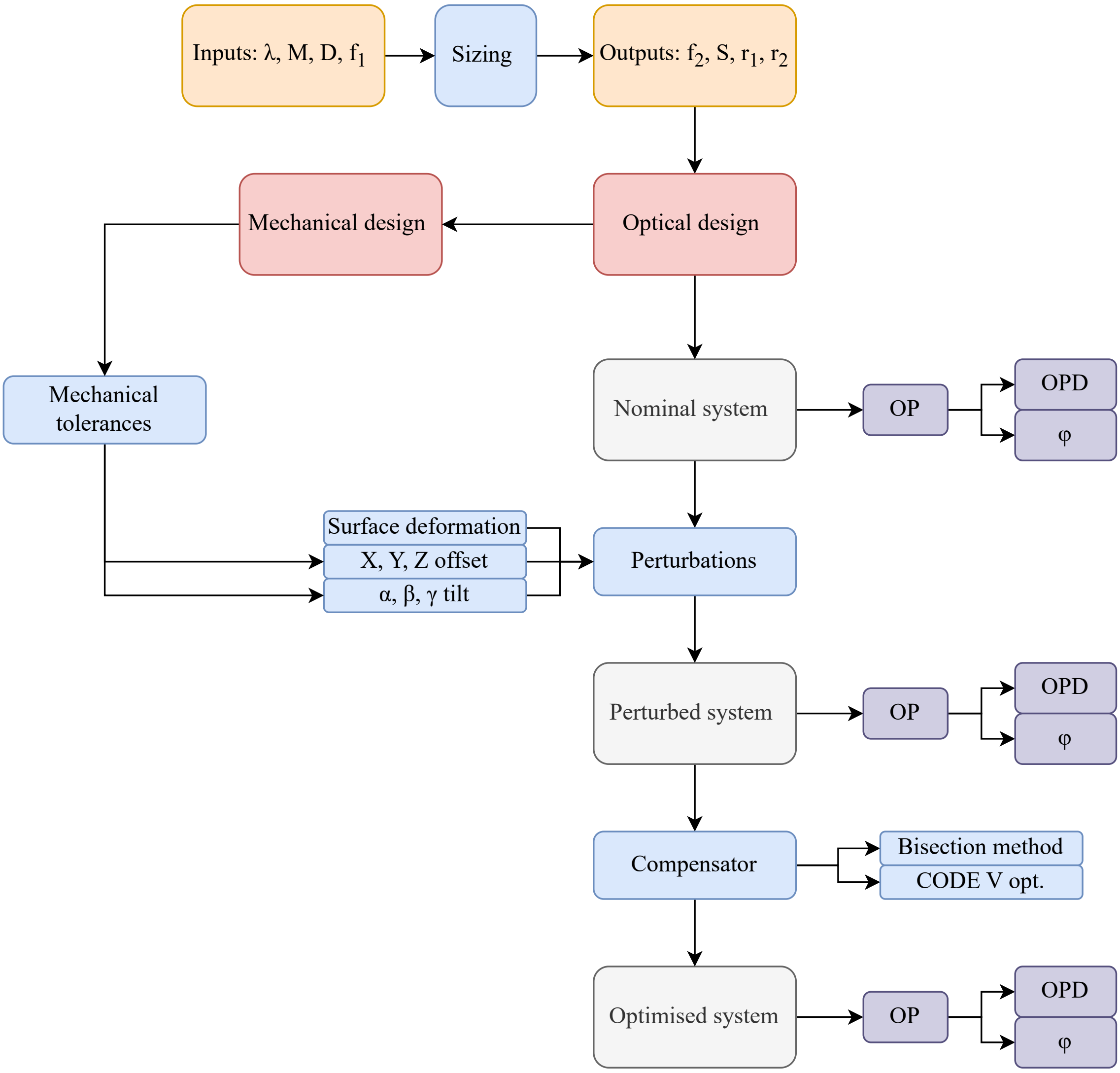

Figure 4.10: Block diagram of the methodology adopted involving both the optical and mechanical design of the four apertures nulling interferometer.

Chapter 5

Compensator impact on performances

Note:

This chapter has been co-authored with Francesco De Bortoli with the goal of combining the optical design analysis results with the numerical model in order to evaluate the validity of the proposed design and the improvements that the compensator provides to the system using simpler evaluation metrics.

The aim of this chapter is to show the compensator impact on the performances of the analysed four apertures nulling interferometer. The first section focuses on the logic and design of the compensator, implemented in CODE V software. In particular, the practical implementation of the compensator is presented, describing two possible tools, one based on the bisection method and one on CODE V optimisation commands. Subsequently, a comparison between the two compensators and their effect on the results are outlined.

Furthermore, a detailed interferogram analysis in presented, showing the results for a single and then multiple branch perturbation. It follows an overview of statistical analysis including the transmission maps and the potential exoplanet yields using the statistical tool P-POP[38].

Finally, a perturbed comparison for multiple arrays is presented. The difference with the nominal analysis is highlighted, in particular regarding the non-significant resistance to the errors by the considered arrays, making the choice of the array driven by external parameters.

5.1 Compensator logic and design

The aim of a compensator is to optimise the perturbed system in order to be as close as possible in terms of performances to the nominal configuration, guaranteeing the correct functioning of the system. In certain cases, the degradation resulting from the perturbations is minimal, however, for large telescope optics, some type of active compensation or adjustment, even if applied intermittently, is essential[73].

In reality, the compensator is represented by actuators, which compensate the perturbations by translating or rotating a target mirror and by wavefront sensors, which measure the shape or distortion of a light wavefront as it passes through or reflects from an optical system. Therefore, the final goal is to obtain an OPD as low as possible by adjusting the position of the target mirror, which in most cases is the secondary mirror[81], considering that its size is significantly smaller than the primary mirror, therefore more easily adjusted.

To complete system compensation, it is first necessary to determine the correction (or adjusting) values. Several alignment algorithms have been explored for this purpose, including the Sensitivity Table Method (STM), Merit Function Regression (MFR), and Nodal Aberration Theory (NAT). Among these, STM is the most commonly used. It relies on the sensitivity of wavefront aberrations to perturbation parameters and includes approaches such as Zernike coefficient sensitivity, RMS wavefront error sensitivity, and MTF sensitivity[81].

5.1.1 Practical implementation of the compensator

Considering the optical design presented in the previous Chapters, two possible different compensator have been developed and implemented. The first one uses the bisection method, while the second one is based on CODE V optimisation commands.

Bisection method

The block diagram presented in Figure 5.1 shows the iterative optimization process used to implement a bisecting algorithm to minimize OPD by adjusting four actuators: XDE, YDE, BDE, and ADE, respectively decentres with the respect to X, Y and tilt angles with respect to X, Y.

Firstly, the OPD is measured through a sensor in order to obtain a baseline. The process iteratively tunes a set of actuators and each actuator is perturbed independently. The actuator is displaced by a predetermined step in the current direction and the new OPD is measured after the perturbation. If the OPD measured is smaller than the initial OPD, the direction of the movement is retained, otherwise the step is halved and the movement direction is flipped.

After one complete iteration over all actuators, the algorithm checks if the step size for all actuators is less than a predefined resolution threshold and if so, the optimisation converges, otherwise the process restarts from the top. The measurement of the OPD is performed using specific sensors which provide real-time measurements of system performance. More details on the macro-PLUS code can be found in Appendix A.3.1.

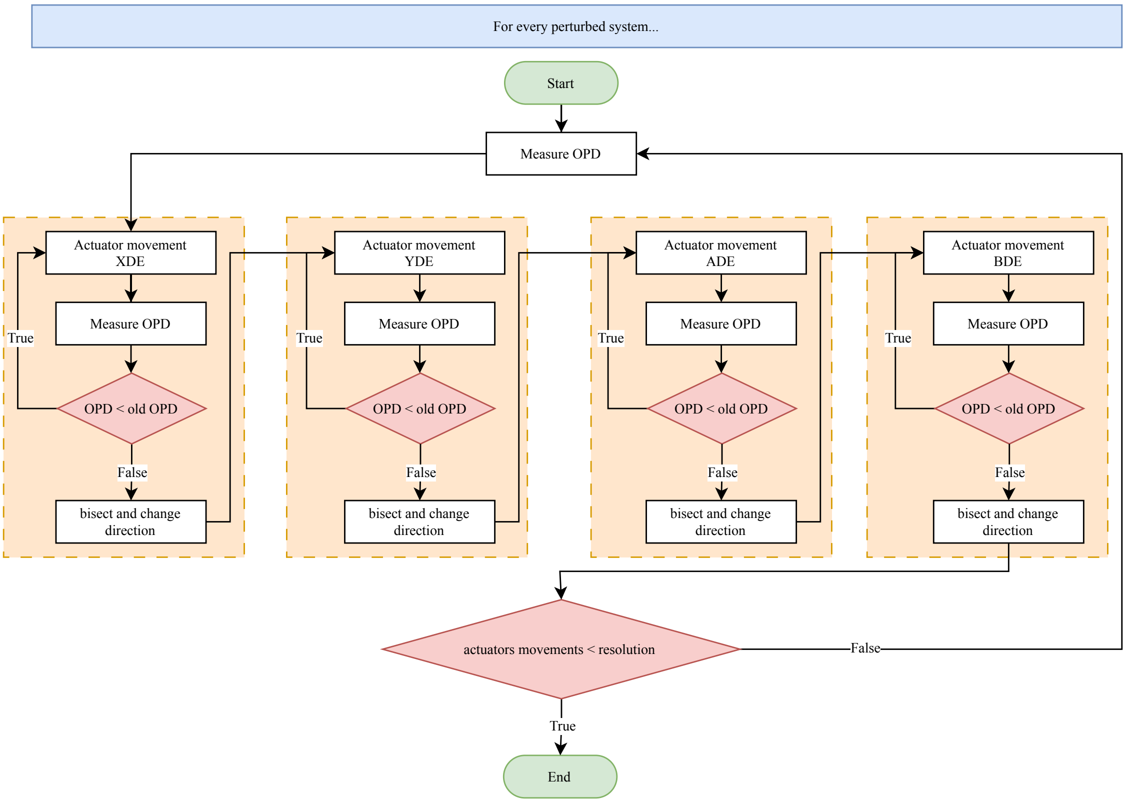

Figure 5.1: Block diagram of the closed loop feedback used to implement the compensator with the bisection method.

CODE V optimisation

Figure 5.2 represents an iterative optimisation procedure for aligning an optical system, in particular taking into account mechanical tolerancing of the secondary mirror.

The process begins with initialising the system where all the optical surfaces without associated actuators are mechanically fixed, meaning their position and orientation remain constant during the optimisation. The secondary mirror is granted of 6 degrees of freedom (DOFs) which are active variables in the optimisation cycle. The internal merit function optimisation loop in CODE V is executed. This adjusts the (DOFs) of M_2 to minimise the OPD. An afocal constraint is also applied, indicating that the system should maintain a collimated beam.

Then, constraints are applied to the optimisation variables, in order to obtain real values for existing actuators[63]. In particular nanometric limits on translations, which ensures extremely fine control over mirror positioning, and arcminute limits on rotations, which restricts angular misalignment within a few arcminutes. These constraints are essential for ensuring that the solution remains physically realisable and within the capabilities of actual mechanical actuators.

After the optimisation, the final adjustments are checked against actuator resolution, ensuring the proposed movements are within the control precision of available actuators.

The optimisation terminates once all constraints are met and the system achieves desired performance. More details on the macro-PLUS code can be found in Appendix A.3.2.

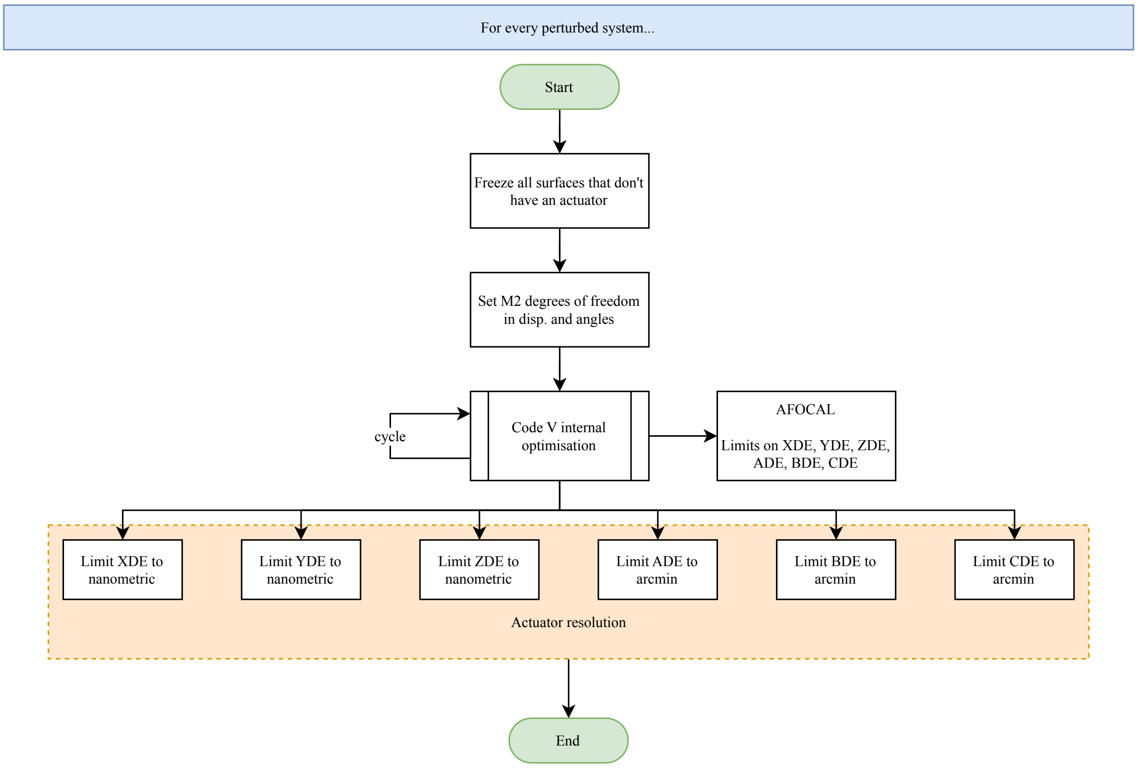

Figure 5.2: Block diagram used to implement the compensator with CODE V optimisation.

5.2 Comparison of improved results with compensator

The actual potential of the two compensators has been tested on the system using two macro-PLUS programs implemented in CODE V software.

A surface deformation of $\lambda/10$, an offset of 1 µm in the X, Y and Z direction and a tilt of 9.28×10^{-4} arcmin with respect to X, Y and Z direction, for the primary mirror and 22×10^{-4} arcmin for the secondary mirror have been applied. In particular, a Monte Carlo simulations around these values has been carried out. Then the compensators are used as defined in the previous section in order to optimise the system performances.

Figure 5.3 shows the effect of the compensator implemented with the bisection method on the perturbed system, showing an improvement in the performance, since the values of the OPD are smaller, as expected. While, Figure 5.4 shows the effect of the second compensator on the perturbed system. It can be observed that the results are not in line with the expectation, since the performances get slightly worse. Therefore, only the the bisection method is valid and its positive impact on the system will be further addressed in the discussion.

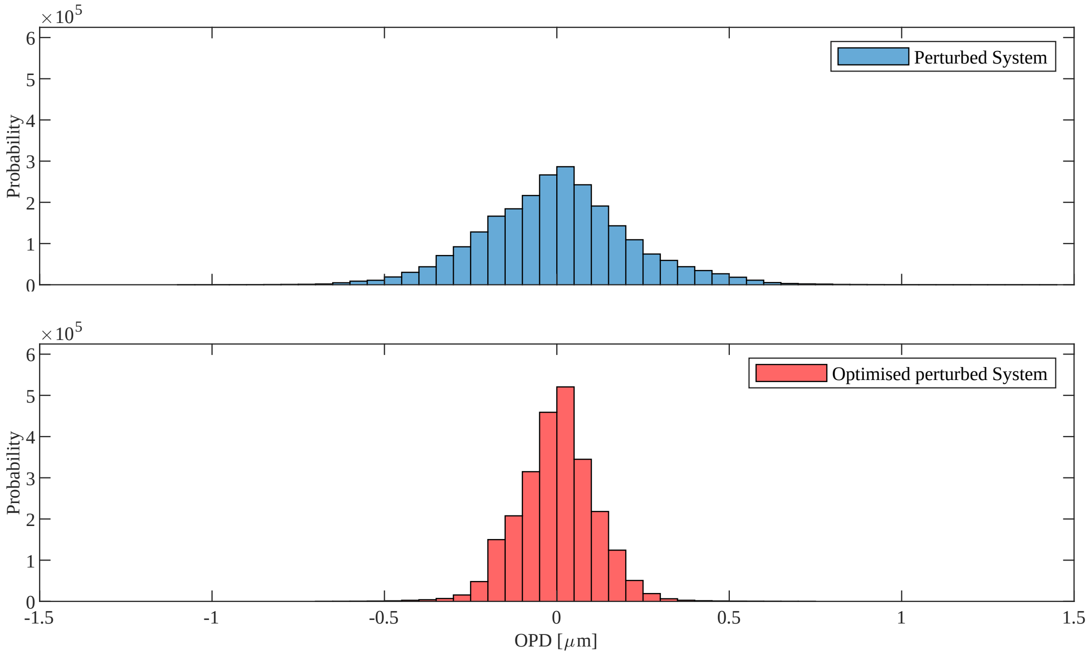

Figure 5.3: Histogram of the optical path difference of the perturbed system before and after the compensator implemented using the bisection method over 50 simulations.

Table 5.1 shows a comparison between the two compensators, where the CPU time is basically the same, while their effect on the OPD is significantly different.

		Maximum OPD [µm]	
	Elapsed time	**Perturbed**	**Corrected**
Bisection method	00:42:26	1.4039	0.7493
CODE V optimisation	00:42:52	1.2224	1.6481

Table 5.1: Comparison between the compensator with the bisection method and the the compensator with CODE V optimisation over 50 iterations and 49077 displaced rays. In particular the computational time is represented in the format HH:MM:SS and the maximum values of the optical path difference before and after the compensator effect in [µm].

Figure 5.5 gives an overview of statistical elements of the two populations of corrected (using the bisection compensator) and uncorrected values. As it can be seen, the correction actually strongly reduce the entity of disturbances acting on the screen, hence showing once again the quality of the implemented compensator.

The same improvements are visible for different metrics in Figure 5.6: in the first graph, the nulling ratio has been computed for each N_S simulation before and after the correction. Points that lay below the unit line are then an improvement and that what happens on the vast majority of the times. There are few points that lay close to the lime or immediately above: in that case, globally, the compensator is not able to significantly improve the situation.

Figure 5.6b shows instead the improvement value (normalised) for each point on the pupil screen. A fictitious value of the nulling ratio has been computed for each point and later the corrected

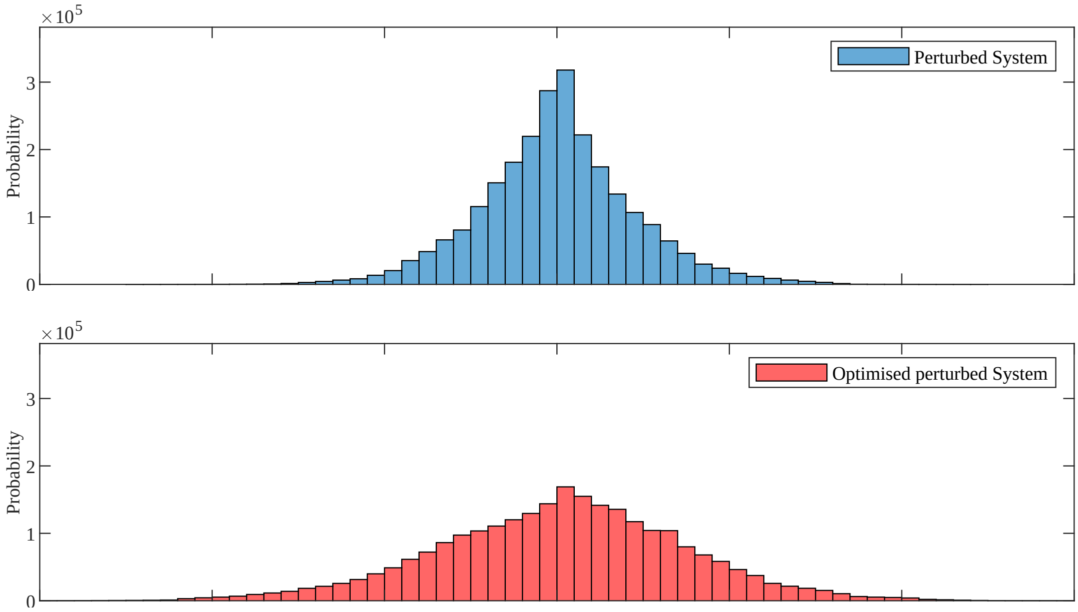

Figure 5.4: Histogram of the optical path difference of the perturbed system before and after the compensator implemented using CODE V optimisation over 50 simulations.

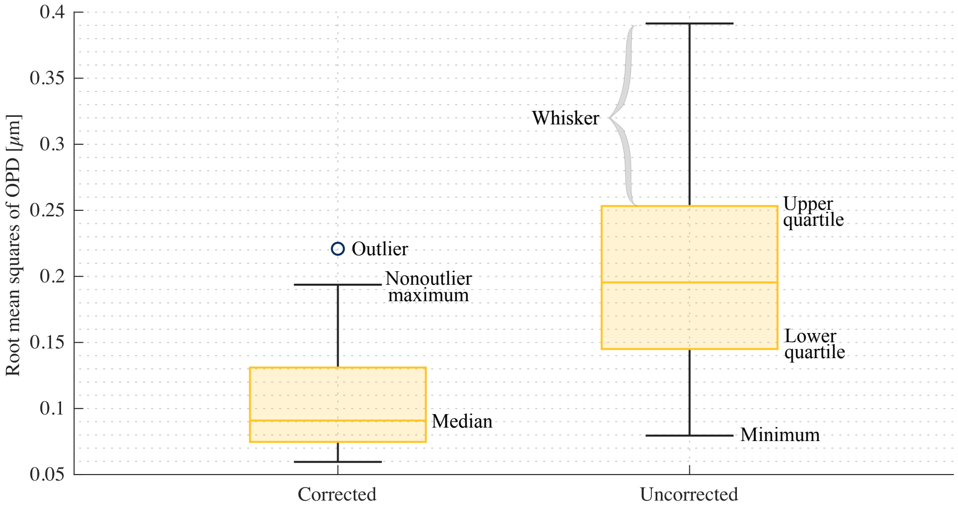

Figure 5.5: Statistical summary of the perturbed and corrected analysis (of the bisection compensator).

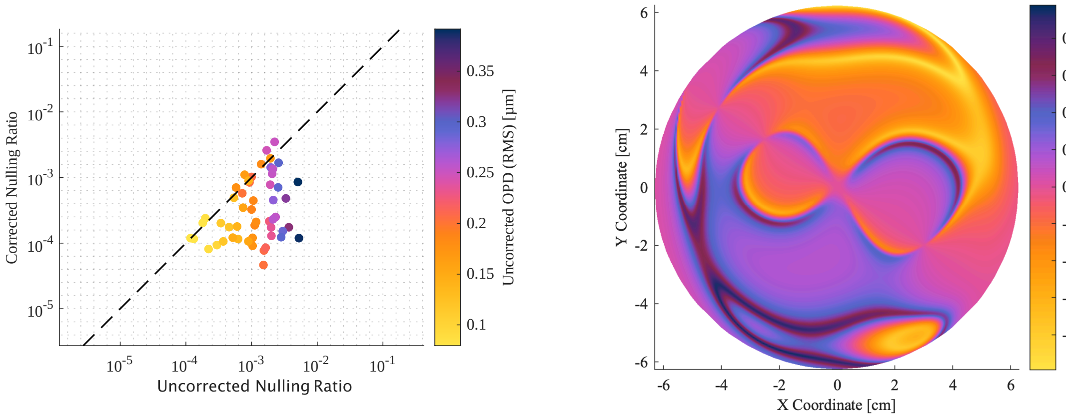

(a) Correlation of the correction

(b) Improvement scale

Figure 5.6: Improvements brought by the bisection compensator on the analysis. On the left: the resulting global nulling ratio for each simulation is plotted for the two cases. Each point that lies below the bisection line is an improvement over the unperturbed result. On the right: index of improvement of each point at the pupil screen: negative points are improved, while positive points got worse.

value has been subtracted to the uncorrected one in logarithmic scale: positive points show an improvement, while negative points show a global decreasing in quality. This value is deemed to be fictitious since the pupil plane cannot actually be perceived and ultimately the general value of the nulling ratio is rather resulting from a combination of all the considered values, therefore, from this point onward, the value will be referred as nulling ratio distribution.

As it can be seen, the pupil screen is mostly populated by positive values, therefore indicating a global improvement over the pupil plane, once more validating the working principle of the implemented compensator.

5.3 Interferogram analysis

To better visualise the results of the analysis in terms of valid metrics for interferometry, a new procedure is here implemented and presented: while up to this point, most of the metrics were analysed at the image screen, that is based on angular grid position, in the sense that the response function was computed as a function of the angular position on the sky $\boldsymbol{\vartheta}$, other considerations can be made to compute the response as a function of the pupil plane coordinates $\mathbf{x}$.

Figure 5.7 illustrates the process here considered: by considering (at least initially) that all the apertures except the first display a nominal response and that the first one is subjected to one of the different simulations computed with the use of CODE V, then, while considering Equation 2.8, instead of spacing over the different angular offsets, a map is obtained by each time fixing a single value of this parameter; in this case, then, the response function R is a function of the coordinates within the pupil planes that appear indirectly within the expression via the phase term $\Delta\Phi$:

$$R_{\boldsymbol{\vartheta}}(\mathbf{x}_{\text{pupil}}) = \frac{1}{2}\sum_{j=1}^{N} U_j \sum_{k=1}^{N} A_j A_k \cos\left(\frac{2\pi\,\boldsymbol{\vartheta}}{\lambda}(\mathbf{x}_j - \mathbf{x}_k) + \Delta\Phi_{jk}\right). \tag{5.1}$$

As a reminder, in Equation 5.1, the phase term $\Delta\Phi$ is a function of both the “nominal” phase (assigned to the designated arm j through phase retarders and optical delay lines in order to obtain the desired nulling target) and the undesired perturbance introduced by the optical system. In addition, disturbances introduced by external factors will also influence the results but are neglected in this analysis. In summary

$$\Delta\Phi_{jk} = (\Phi_j + \tilde{\varphi}_j(\mathbf{x}_{\text{pupil}}) + \tilde{\varphi}_{j,\text{external}}) - (\Phi_k + \tilde{\varphi}_k(\mathbf{x}_{\text{pupil}}) + \tilde{\varphi}_{k,\text{external}}), \tag{5.2}$$

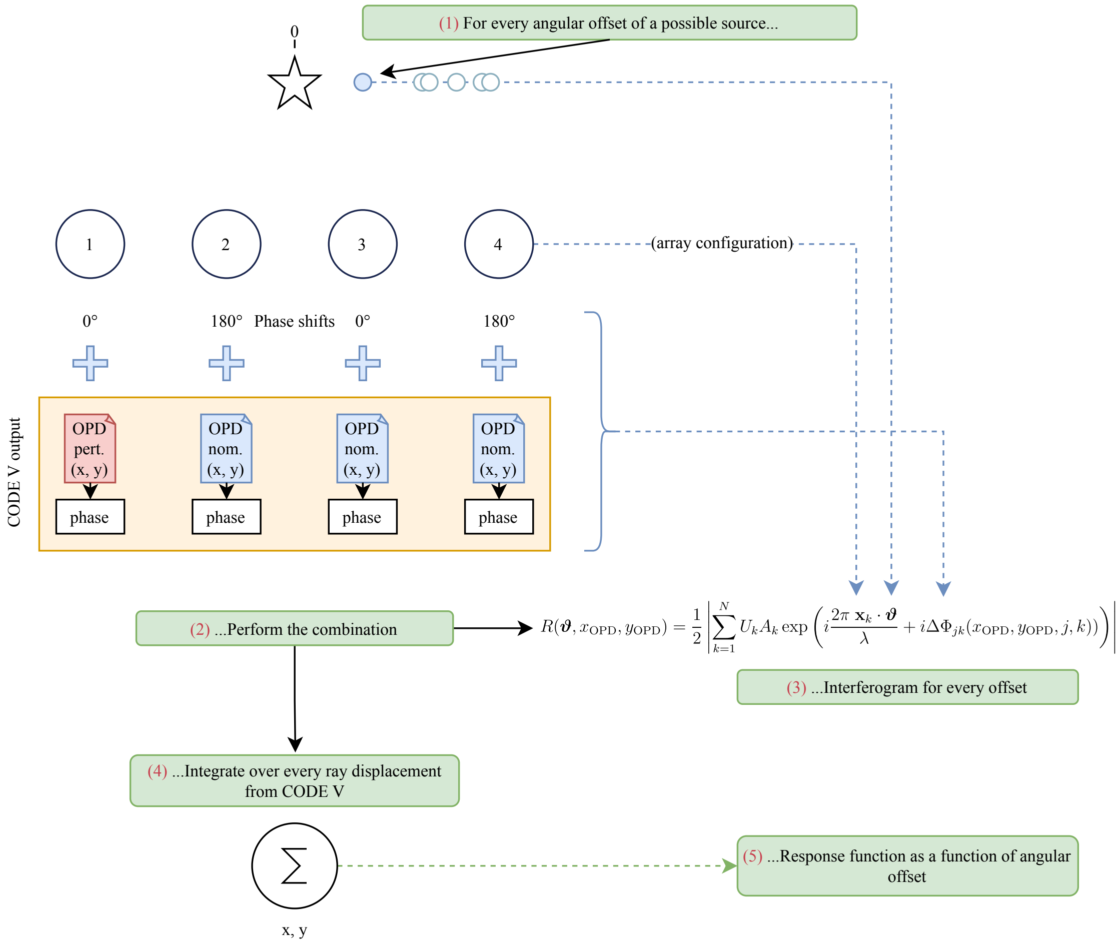

Figure 5.7: Block diagram of the algorithm used to compute the interferogram response and its integration: the response function is not computed anymore as a function of the angular position on the image screen $\boldsymbol{\vartheta}$ but as a function of the x, y coordinates on the pupil screen.

Where, in Equation 5.2, when $j = 1$, $\tilde{\varphi}_j(\mathbf{x}_{\mathrm{pupil}})$ comes from the perturbed simulations of CODE V; in all the other cases, it comes from the nominal results.

It is therefore possible, for every angular offset in the sky, to obtain the interferogram result for every point of the pupil screen, making use of the already developed analysis. While, in practice, a 2D array of points (since $\boldsymbol{\vartheta}$ is essentially a vector) could be used, given the symmetry of the problem, in order to simplify the analysis, in the remaining part of the section it will be assumed to swathe over linear positions of angular offsets.

Eventually, the response function for the entire sky is obtained by double integrating the maps obtained above over all the pupil coordinates:

$$RF(\boldsymbol{\vartheta}) = \iint\limits_{\mathbf{x}_{\mathrm{pupil}}} R_{\boldsymbol{\vartheta}}(\mathbf{x}_{\mathrm{pupil}})\, d\mathbf{x}. \tag{5.3}$$

This method, with respect to the computation of the transmission map making use of the independent coordinate $\boldsymbol{\vartheta}$, ensures that the found result is not the result of a simple use of a single perturbed value, but every computed result from CODE V concurs to the computation of the final result.

5.3.1 Single branch perturbation

In the rest of the current section, the considerations shown above will be applied to a linear array. Very similar considerations can clearly be obtained for any other configurations; therefore, for brevity, they will not be taken into account.

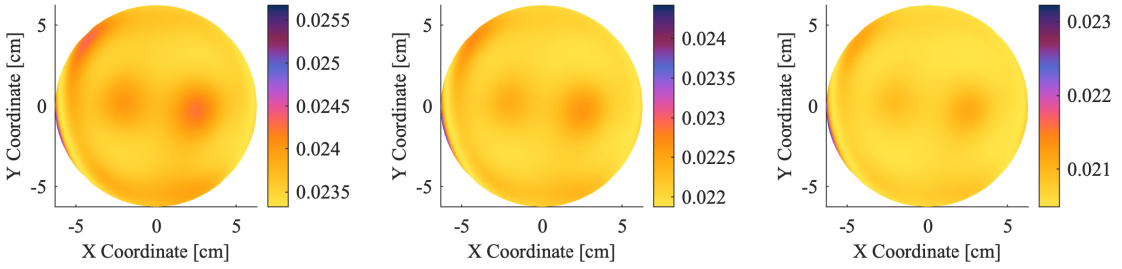

(a) -700 mas (b) 0 mas (c) 700 mas

Figure 5.8: Intensity response (in m^4) for every displaced ray of a Linear Array interferometer at pupil plane for different angular positions (where 0 mas represents the target point, i.e. the target star) on the screen. All these angular positions belong to the same simulation.

As anticipated in Figure 5.7, initially, the tool is validated by perturbing a single branch, by converting the OPD resulting from the ray tracing software into a phase by the means of Equation2.4. It is possible to investigate, over N_S simulations, N_ϑ angular offsets in the sky, leading to the necessity to compute $N_S \times N_\vartheta$ interferogram diagrams as a result.

Figure 5.8 presents, for a random simulation applied on the first branch, the resulting virtual interferogram at specific angular offsets. At first glance, the three images seem almost identical, displaying small variations on one side of the pupil plane and deformations induced by the surface deformations, with small variations in the scale from one to another.

Even if small, these variations are indeed enough to cause significant variations in the integrated function, as will be shown below. As can be noticed as well, the central point is the point having the smallest error—a consequence of the central point having no optical path difference by definition.

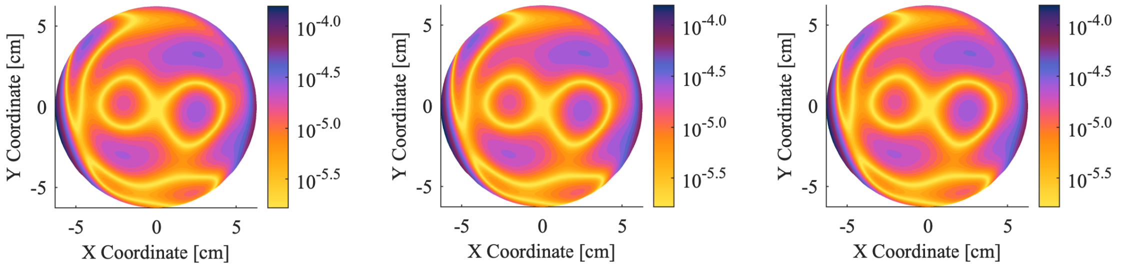

(a) 1$^{\mathrm{st}}$ simulation (b) 2$^{\mathrm{nd}}$ simulation (c) 3$^{\mathrm{rd}}$ simulation

Figure 5.9: Nulling ratio distribution for every displaced ray of a Linear Array interferometer at pupil plane for different angular positions on the screen.

Very similar considerations can be found in Figure 5.9, which instead depicts the nulling ratio for each point at the pupil plane. As a theoretical reminder, the nulling ratio does not depend on the angular position used to compute the intensity response, but only on the phase combinations and therefore the different simulations, providing, as a result, N_S different pupil diagram screens. In addition to that, the value should only be taken as a reference of the “quality” of the specific point as, ultimately, only a single value of the nulling ratio will result from the integration of the pupil screen response or the analysis of the image screen (which is only a theoretical concept).

That being considered, as can clearly be seen, the results display very small changes from one simulation to another. All of them display a region which is almost perfect, with nominal behaviour, and side regions with worse results.

Once statistical results are computed for each point, the results shown in Figure 5.10 are found; it is clearly shown that, over the N_S simulations, only the central point displays an almost-perfect nulling ratio, this last result confirmed by the median and worst nulling ratios for each point. In the same way, the most displaced rays, instead, can only produce low validity nulling ratios.

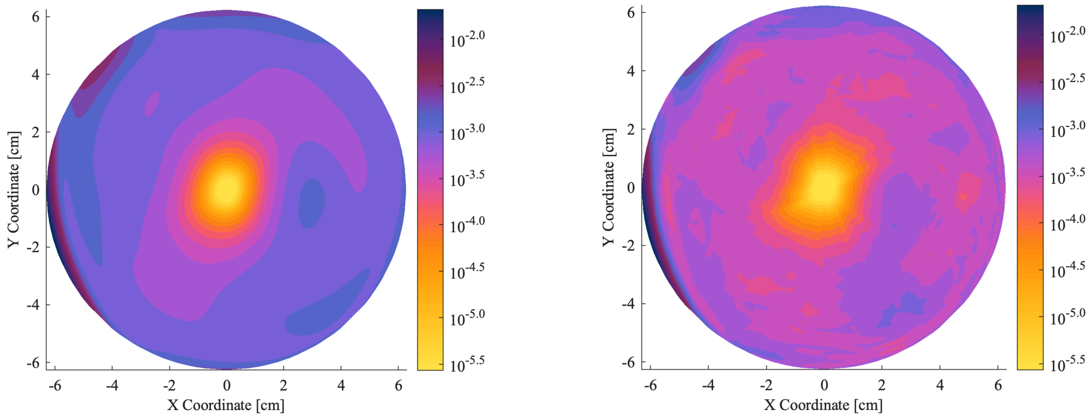

(a) Mean nulling ratio distribution

(b) Median nulling ratio distribution

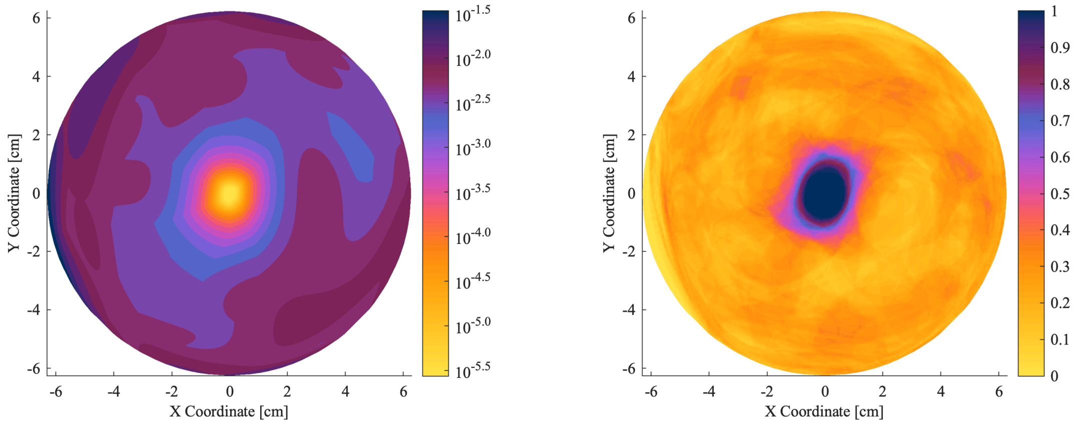

(c) Worst case nulling ratio distribution

(d) Probability of high nulling ratio distribution

Figure 5.10: Statistical distributions of different performance indices for the nulling ratio distribution over every displaced ray of a Linear Array interferometer at pupil plane for all cumulative angular positions on the screen.

As a summary of the reported information above, Figure 5.10d displays the probability of finding a "good" nulling ratio (that is, above 10^{-4}) for each specified point. Indeed, the result confirms once more that only the central point and the limited surrounding area provide such possible results. A smaller aperture would, effectively, increase, at least in relative size, the well-performing region, but it would ultimately reduce the observing power of the interferometry, as the aperture size rules the amount of light that reaches the combiner.

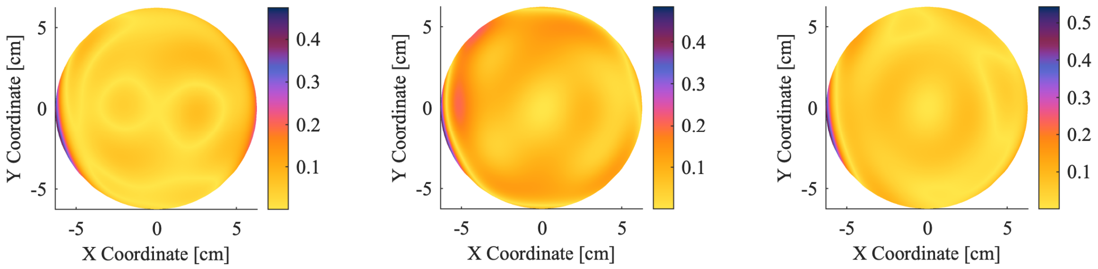

(a) 1st simulation

(b) 2nd simulation

(c) 3rd simulation

Figure 5.11: Modulation efficiency for every displaced ray of a Linear Array interferometer at pupil plane for different angular positions on the screen.

It is worth noticing that the compensator was able to avoid regions with non-working nulling ratio;

therefore, while 10^{-2} is not by any means a desirable result, its introduction allowed for a globally improved result.

The complementary metric to the nulling ratio is the modulation efficiency, shown in Figure 5.11. Once again, it does not depend on the angular position on the image screen, but only on the array size and as it can be seen it behaves like the "negative" of the nulling ratio, since it is maximum at the sides of the pupil screen. This does not allow to draw consequences on the possible position of the exoplanets, as the pupil screen cannot be measured, yet it shows once again how the deformations work.

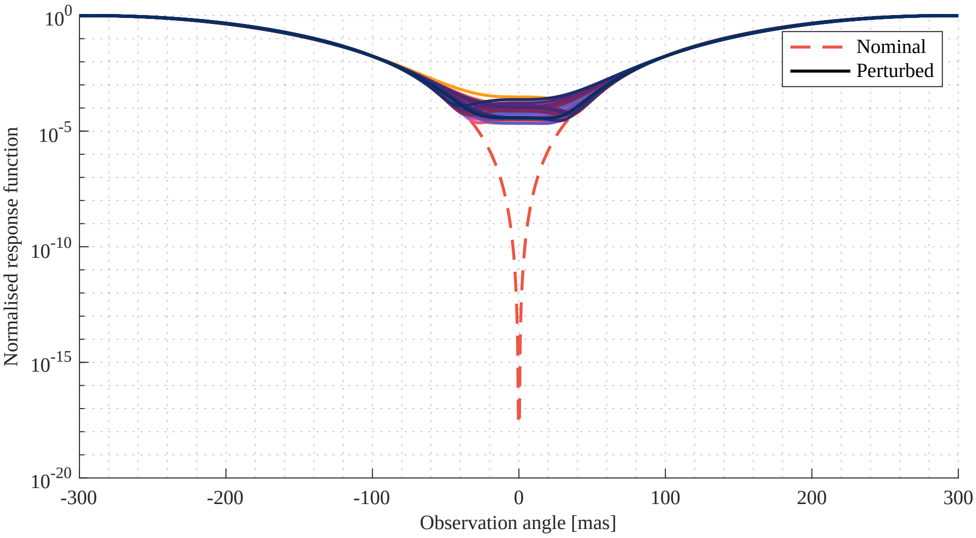

Figure 5.12: Comparison of the normalised integrated response function for the nominal and the perturbed system.

If the integration is performed, eventually the result shown in Figure 5.12 is shown, both for the nominal case (in dashed lines) and the perturbed systems, showing N_S overlapping lines. While for regions with bright fringes the lines tend to behave close to the ideal target, dark fringes significantly lose nulling power: in the best case scenario, the minimal perturbed line is found around 10^{-5} but can get as high as 10^{-3} (10^{-3} without compensator), which is clearly a strong loss in contrast, therefore showing how significant this loss can be for a real implementation.

5.3.2 Multiple branches perturbation

Results tend to become even less predictable once all the apertures are perturbed: starting from the pool of N_S simulations computed by the ray tracing software, for a specified number of N_{ms} perturbed simulations, each aperture is assigned one of the random simulations from the pool and the exact same procedure reported in Figure 5.7 is performed once more.

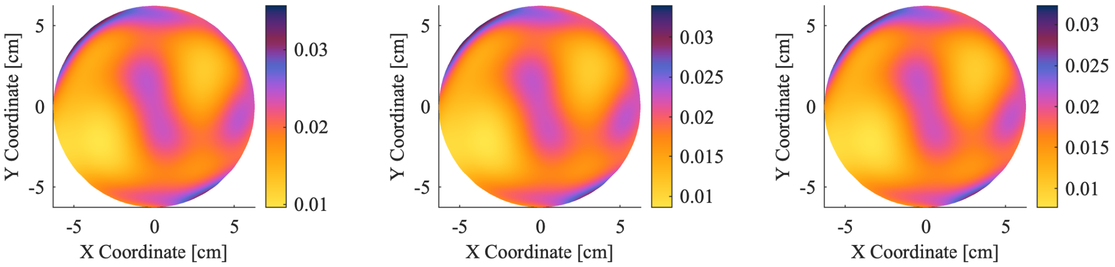

(a) -700 mas (b) 0 mas (c) 700 mas

Figure 5.13: Intensity response for every displaced ray of a Linear Array interferometer at pupil plane for different angular positions on the screen.

The virtual interferometric response, before integration, is shown in Figure 5.13: compared to what was shown previously for a single branch, the variations are covering a higher part of the diagram, given the higher amount of perturbations taken into account. The central point is not any more the point displaying the best behaviour.

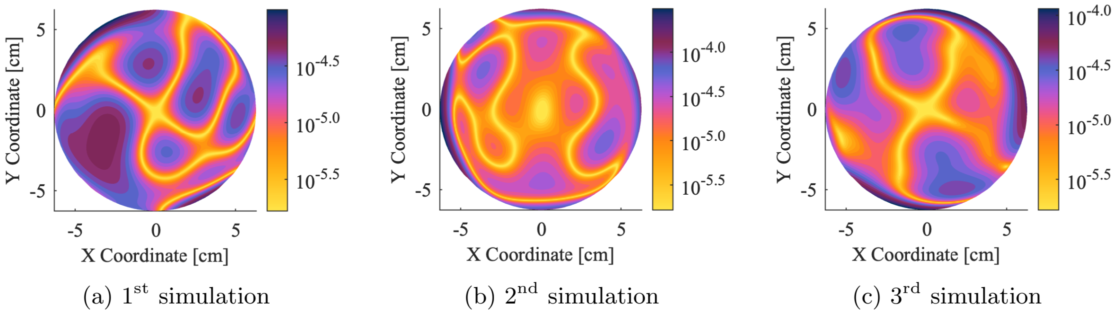

(a) 1st simulation (b) 2nd simulation (c) 3rd simulation

Figure 5.14: Nulling ratio distribution for every displaced ray of a Linear Array interferometer at pupil plane for different angular positions on the screen.

Concerning the nulling power, while in Figure 5.9 all the diagrams looked almost the same, when considering multiple apertures, diagrams show different results as shown in Figure 5.14.

Each of the N_{ms} simulations now yields a different result, mostly a consequence of how simulations are taken into account: for once, Figure 5.14b is significantly more perturbed than Figure 5.14a. The latter, in fact, shows a larger and spreader bright region (i.e. better nulling ratio), while the former has a wide dark region which is significant in indicating worse results.

The larger entity of multiple-branches perturbations is shown also in Figure 5.15, especially from Figure 5.15d: the size of the target nulling ratio region is significantly smaller than what was seen for a single branch perturbation, therefore pointing targets may become even more stringent than what was anticipated before.

The integrated response function (from Figure 5.16) summarises what has been shown by individual plots, displaying again the loss of the perturbed N_{ms} simulations over the nominal behaviour. While, with respect to the single branch perturbations, the result seems similar, it can be ultimately seen that now the worst case scenario is above the 10^{-3} limit previously mentioned.

As a conclusion, then, the changes in the interferometric response can visualise part of the performances of the system: while for the single perturbed arm there seems to be a certain tolerance to the error, with a larger region that present almost-nominal results, the same cannot be said about multiple-perturbed arms, which instead produce undesired results. Based on these results, then, it is also possible to design corrective elements to reduce the impacts of perturbations on the system through the fine-tuning of the compensators.

5.4 Overview of statistical analysis

Up to this point, considerations on the combination of different branches have led to the visualisation of how the nulling behaviour and the response function are changed by such perturbations. This Section aims to visualise how the remaining performance parameters that can be associated to a nulling interferometer change.

In order to analyse such changes in the system, for each simulation, each of which has N_P points, the root-mean-square value of the property under analysis (transmission maps, PSFs and exoplanet yields) will be taken as a measure of the perturbation of the phase, thus leading to N_S cumulative curves or surfaces that can be studied through statistical analysis.

5.4.1 Transmission maps

The transmission map is a key element of the interferometer, since it shows which regions of the sky are mapped to a nulling region and which ones are instead mapped to a constructive

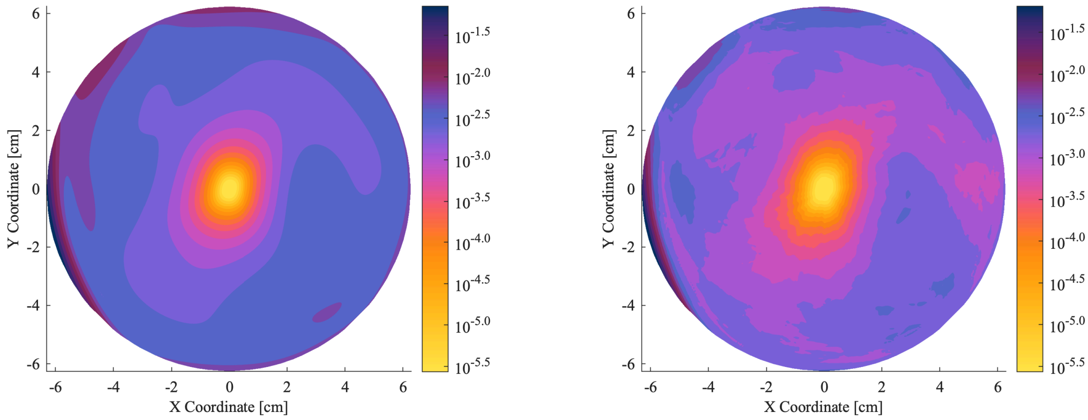

(a) Mean nulling ratio distribution

(b) Median nulling ratio distribution

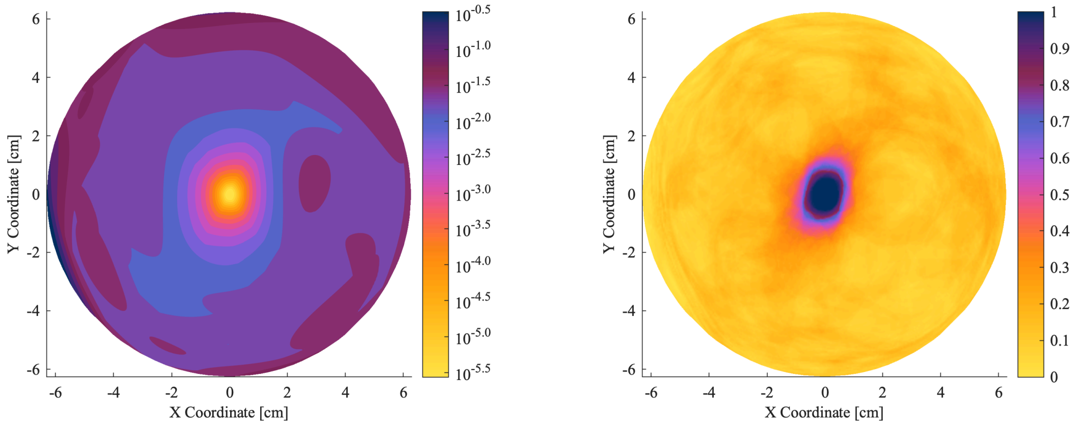

(c) Worst case nulling ratio distribution

(d) Probability of high nulling ratio distribution

Figure 5.15: Statistical distributions of different performance indices for the nulling ratio distribution over every displaced ray of a Linear Array interferometer at pupil plane for all cumulative angular positions on the screen in the case where all the interferometry branches were perturbed.

behaviour. This is fundamental to displaying the response of the interferometer to differently placed exoplanets.

Once again, the transmission map is computed by evaluating Equation 5.1 as a function of the vectorial variable $\boldsymbol{\vartheta}$ (since computed at the virtual image plane), producing the familiar fringe pattern expected by the considered configuration. Nominal results were presented in Section 1.6.2.

What happens, however, if the configuration is no longer ideal and how significant are the changes in the response? A quick answer can be provided by Figure 5.17a which computes the standard deviation for each point of the transmission map: the regions that display the highest variation are those close to the change of concavity of the curve. The regions where normally the highest nulling or the highest constructive points are found are instead significantly less affected by perturbations (by at least one order of magnitude).

Another way to see specifically how the central point, being the target position of the harbouring star, is affected by perturbations is shown by Figure 5.17b, which shows the cumulative distribution probability of a difference value at the origin point smaller than a specific value. Indeed, this graph shows that, for differences up to 0.01% (since the plot was normalised), the probability is around 70%. This is a significant result that, in accordance with Figure 5.17a, states that the centre region is less affected by big perturbations, with only small values differences found here.

The same conclusion can be drawn by looking at the principal component analysis, reported in Figure 5.17c. Given a matrix made by N_{ϑ} points (which is a reshaped vector of the transmission

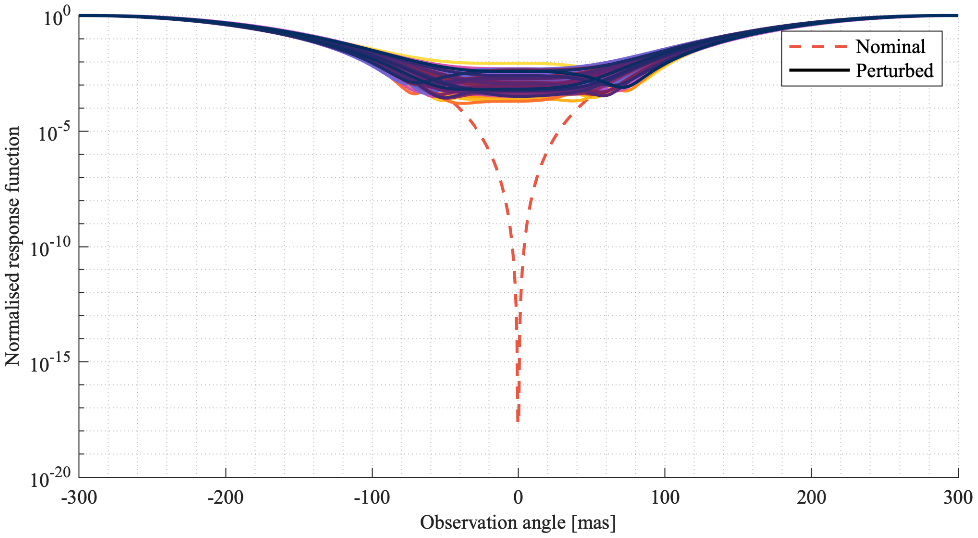

Figure 5.16: Comparison of the normalised integrated response function for the nominal and the perturbed system.

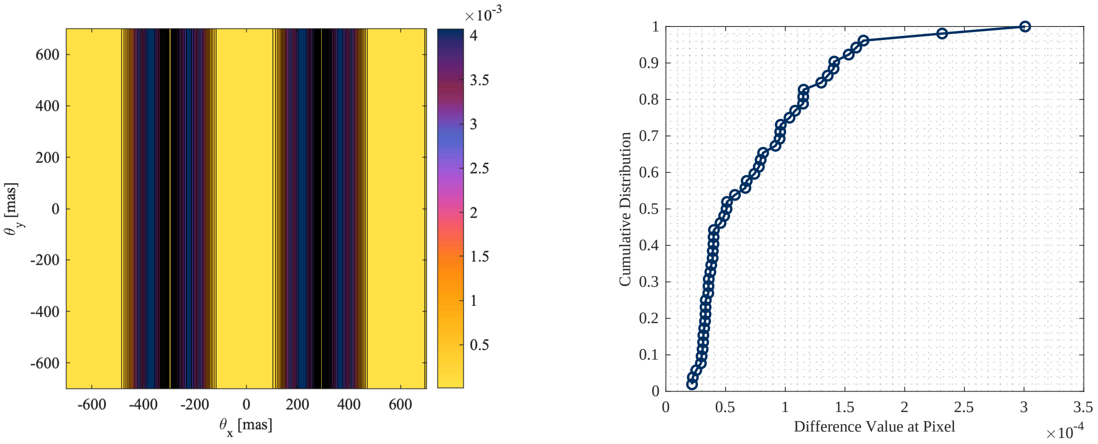

(a) Standard deviation

(b) Cumulative distribution function

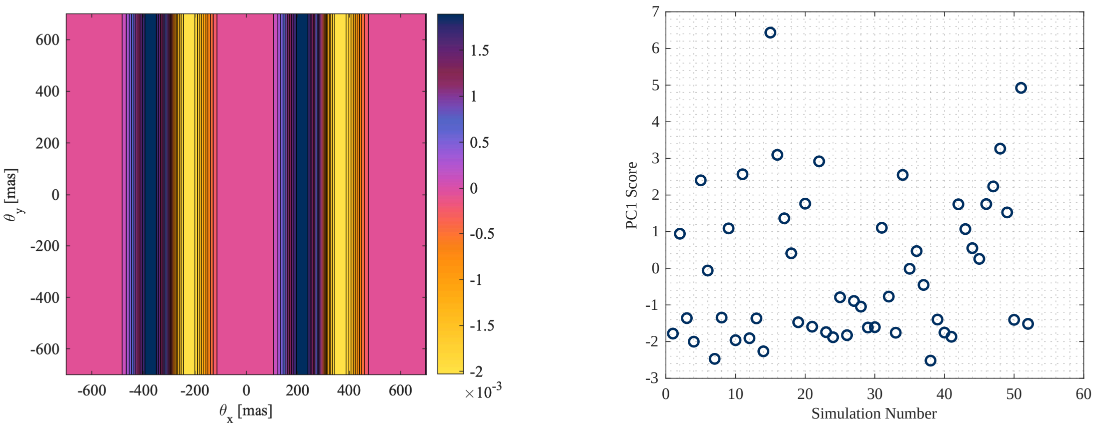

(c) Principal component analysis

(d) First principal component scores

Figure 5.17: Analysis on the N_s simulations in terms of performances of the interferometer, based on the root-mean-square values, on the transmission map.

map points from Equation 5.1) due to N_S simulations and by subtracting the mean value to it,

$$\tilde{\mathbf{X}} = \mathbf{X} - \bar{\mathbf{X}}, \tag{5.4}$$

and by computing the eigenvectors of the covariance matrix associated to these values,

$$\mathbf{C} = \frac{1}{N_S - 1}\tilde{\mathbf{X}}^T\tilde{\mathbf{X}} \qquad \Rightarrow \qquad \mathbf{C}\mathbf{v}_i = \lambda\mathbf{v}_i, \tag{5.5}$$

the resulting eigenvector matrix contains the principal components, shown in Figure 5.17c. Similarly to the standard deviation, again it is shown that regions mostly affected by the perturbations are the transition regions, leaving the nulling and constructive regions mostly unaffected.

The validity of the principal component analysis is given by the score associated to the first eigenvector,

$$\text{PC1}_{\text{score}} = \tilde{\mathbf{X}}\mathbf{v}_i, \tag{5.6}$$

and is reported in Figure 5.17d. Depending on the statistical ensemble, there could be interest in the sign, but most importantly having a non null score indicates a good participation in the considered aspect: in this case, it is abundantly clear that most of the simulations display a significant departure from the null indication; while such departure can be positive (e.g. in accordance with PC1) or negative (in the opposite direction of PC1), for this specific case of random perturbations, it does not hold any particular consideration.

5.4.2 Potential exoplanets yield

The previous sections have shown how the perturbations affect the performances of the interferometer based on few important metrics that have shown the tendency to reduce the contrast and therefore the nulling ability of the instrument. The key metric, however, is undeniably the exoplanets yield of the instrument.

One of the best way to provide an evaluation on the validity of the instrument is to establish how much exoplanets it will be able to see and this is measurable thanks to the availability of statistical tools like P-POP[38] that generate synthetic populations of exoplanets based on found data (mostly from NASA's Kepler).

Out of N_u universes that have been generated by P-POP and N_S simulations due to perturbations, then, it is possible to obtain $N_u \times N_S$ different situations with different yields. In general, a planet can said to be seen if:

- Its angular distance from its harbouring star is smaller than the outer working angle, a value that depends on the diameter of the apertures and the amount of light they can collect, as well as the wavelength. This is usually the easiest requirement to satisfy, as even small apertures are large enough to capture all possible planets.
- Its angular distance from its harbouring star is larger than the inner working angle, a value that depends on the baseline and the wavelength; while it has been shown that this value is not coincident with the resolution, it still holds a significant relation with it and is highly reducing the possible catch, especially for the order of baselines that could fit a single spacecraft.
- Its ratio with respect to the star flux at the observation wavelength is larger than the nulling ratio. In general, most planets become observable even for small integration times (like 24 hours), but longer observation times could increase the yield, but generally reduce the number of observable planets during the spacecraft lifetime.

Clearly, this is only a limited first estimation of the possible exoplanets yield that neglects many effects, including noise sources, instabilities of nulling ratio, the transmission maps and many other confusion-making elements within the sky.

One of these situations (a random universe over a random simulation) is shown in Figure 5.18a: as it can be seen, only a partial number of possible exoplanets is possibly seen by the interferometer

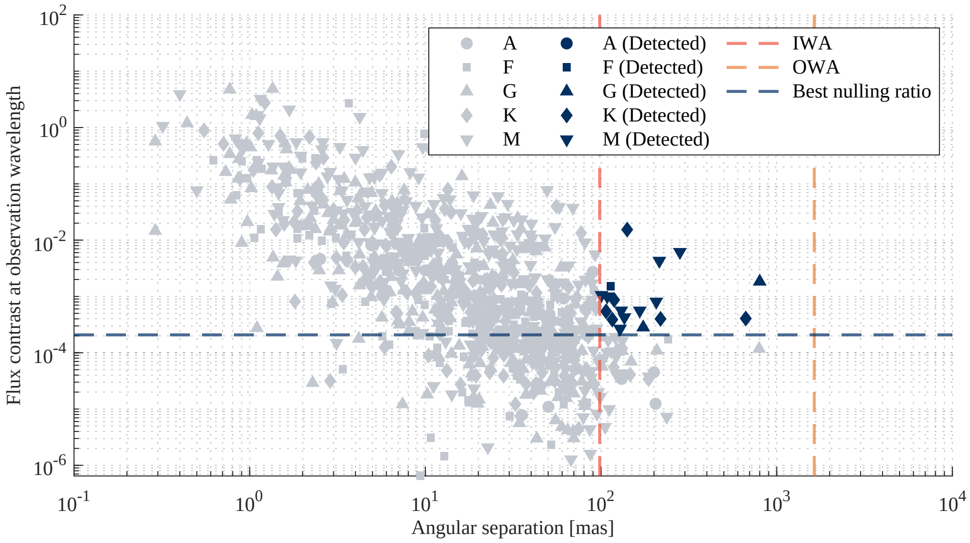

(a) Example yield of a random universe.

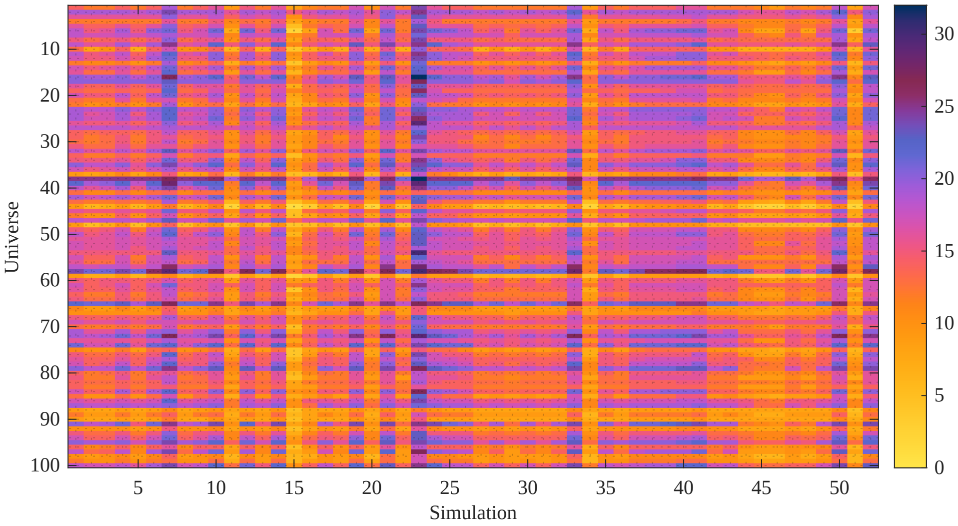

(b) Yield heatmap: number of detections for each universe and simulation.

Figure 5.18: Analysis of the possible yields of the system from the P-POP catalogue.

and the harder limitation seems to be linked to the inner working angle. As for many other engineering problems, it is therefore a matter of trading off for the better aspect, knowing all the possible limitations on sizes and optimisations. The integration time has been selected by looking at similar mission concepts[12].

While Figure 5.18a returns an immediate comprehension of the problem, the general solution is found by looking at the heat map in Figure 5.18b, which provides the sum for every universe and simulation. While there are some unlucky simulations and universes, on average, the amount of detections reflects the expected one from similar concepts[12],[71].

5.5 Perturbed comparison for multiple arrays

To prove the generality of the results that have been shown for a single configuration, this section applies the same methods to five different arrays presented by Lay[53], focusing on metrics of interest like modulation efficiency and nulling ratio using the root-mean-square value of the perturbations. The results will be compared with respect to the nominal value to see the performance loss within the system. In particular, the five nominal systems have been studied in F. De Bortoli Master's Thesis[26]. As an additional consideration, only perturbations within each branch are here considered, but clearly, in a real assembly, the way elements are placed one to the other can and will still introduce other disturbances that are here neglected.

Figure 5.19a displays a violin plot for the modulation efficiency. The violin plot allows to see both the distribution and the frequency of each interval, along with the nominal point, displayed in red. It is interesting to see that, while all the arrays display a significant loss in terms of quality, the modulation efficiency, which itself depends mostly on the phase combinations, is similar for all the arrays. The results are then expected: despite the changing in the array dimensions, then, what matters are the root-mean-square values of the perturbations which are, in fact, always the same for all the different arrays, hence causing a significant, but constant shift for all the considered arrays.

Once again, the second Linear DCB displays the best result, in line with the other nominal values, yet it actually displayed the largest loss in absolute values (around 60% loss), while the other arrays only loose around 40%). It is therefore significant that similar perturbation can cause such high losses to the system.

Figure 5.19b displays instead the nulling ratio distribution with respect to the nominal value, which is nominally dependent on the baselines as well, hence behaving differently depending on the different available combinations. For this reason, then, ideally, both the 3:1 X-Array and the first Linear DCB array are actually both similarly behaving ideally, with the former being the best possible choice. Once the system is perturbed, however, this is not true any more as the distribution cause an standardization of the results which condense to higher intervals, without any particular preference.

In conclusion, then, while the nominal analysis did presents the different strengths of each design, once a perturbation is performed, none of the considered arrays display a significant resistance to the errors, hence the choice of the array to produce may be shifted in favour of other parameters, like the mechanical complexity or the dry weight.

Figure 5.20 provides a summary for every different array and for every simulations, that once again show that all the very different configurations are actually behaving in the same way–despite the nominal differences. For this reason, then, it is fundamental to reduce as much as possible the effects of the perturbations that can highly reduce the quality of interferometry.

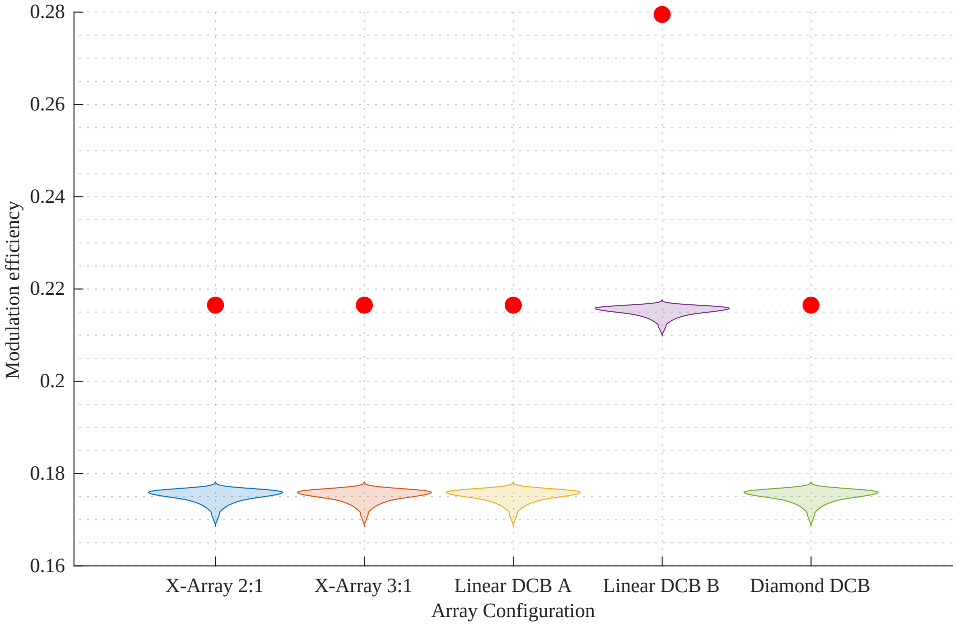

(a) Modulation efficiency.

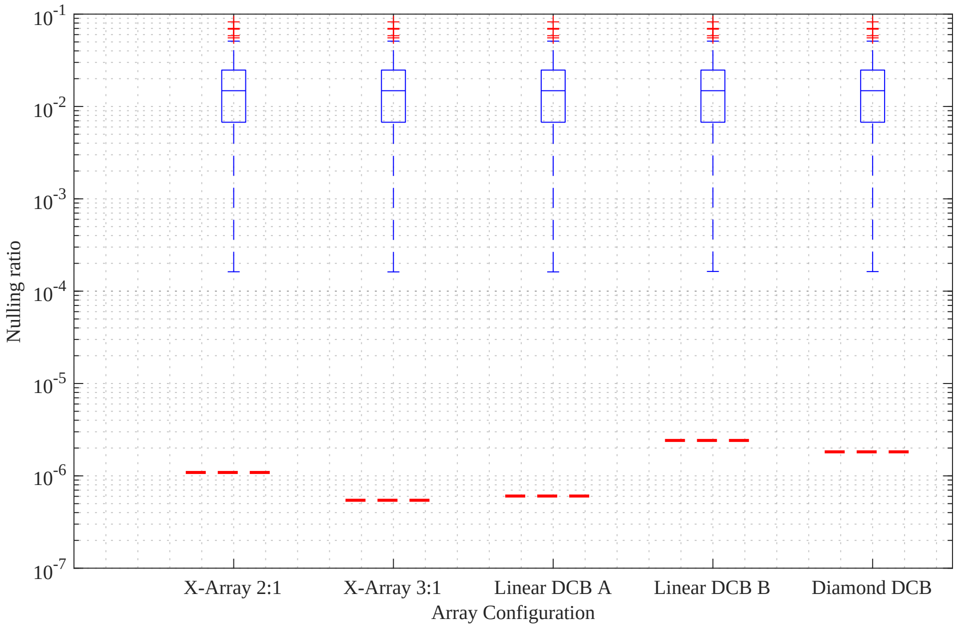

(b) Nulling ratio.

Figure 5.19: Comparison of how the perturbations act on different arrays, in terms of modulation efficiency (visualised with a violin plot) and nulling ratio (with a box plot). The red dashed line and points represent the nominal behaviour.

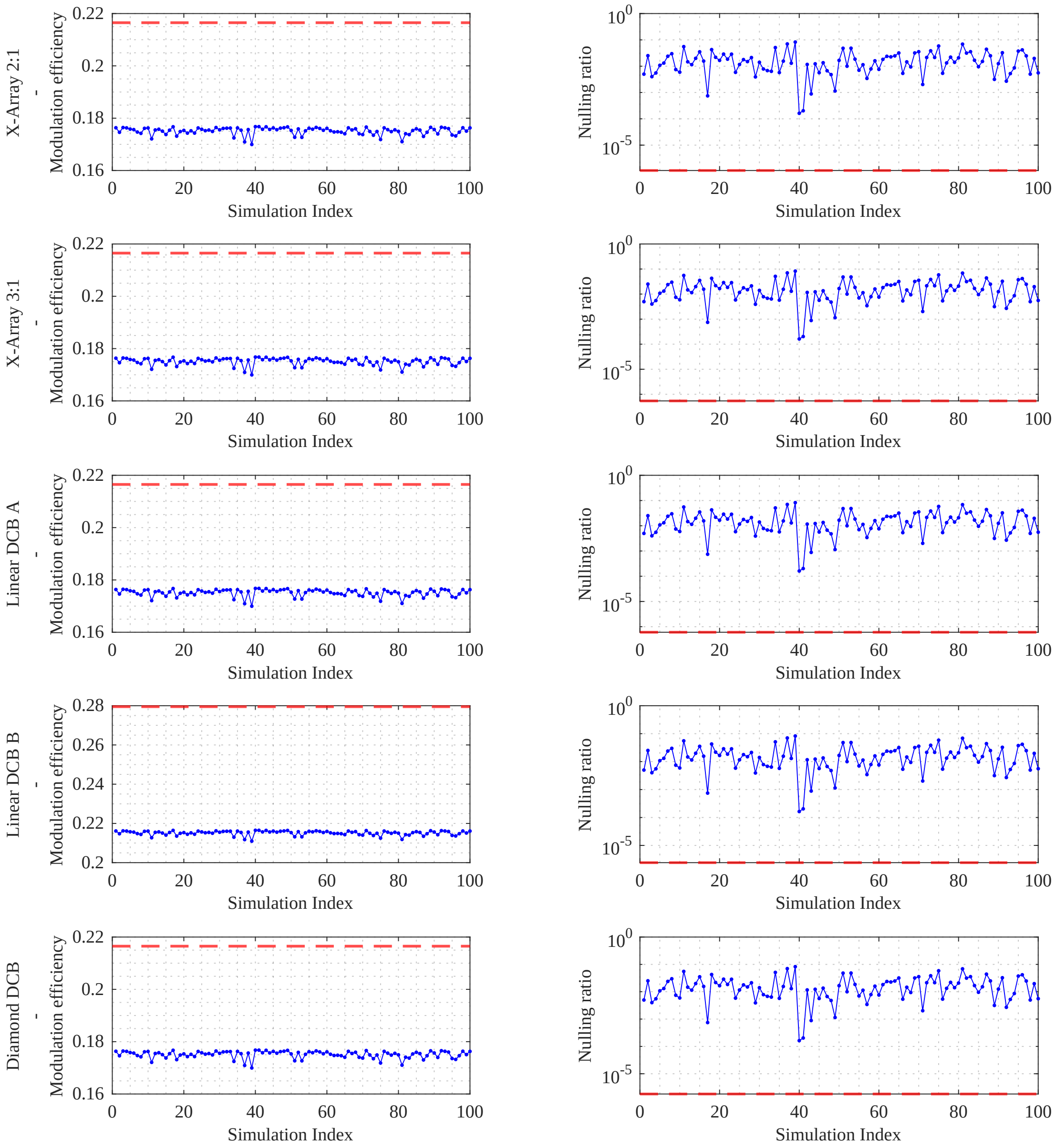

(a) Modulation efficiency.

(b) Nulling ratio.

Figure 5.20: Comparison of how the perturbations act on different arrays, in terms of modulation efficiency and nulling ratio for all the different simulations. The red dashed line represents the nominal behaviour.

Conclusion

The goal of this Master's thesis was to advancing the understanding and design of nulling interferometers for detecting exoplanets. The potential and challenges of nulling interferometry as a viable and promising method for the direct detection of exoplanets were explored. Beginning with a comprehensive review of its historical context and evolution, and culminating in a detailed optical and mechanical analysis, this presented work provides an in depth-analysis of the technique from both a theoretical and engineering prospective.

The review presented in Chapter one illustrates the clear scientific advantages of nulling interferometers, particularly in the infrared regime where planetary emission is strongest relative to the host star. From Bracewell's initial concept to the advanced designs proposed for future space-based missions like Darwin and the Terrestrial Planet Finder Interferometer, nulling has matured significantly.

Chapter two outlined the optical fundamentals critical to nulling performances. Key parameters such as optical path difference and phase shifts were shown, highlighting the fact that the design must rigorously control these factors to achieve a high null depth, which is essential for suppressing stellar light and isolating the faint planetary signal.

The optical design was then developed in Chapter three using CODE V software, providing a practical approach to understanding the subsystem behaviour. Through carefully sizing, modelling and optimisation, including the surface deformation and misalignment analysis, the optical train was validated. This analysis laid the basis for implementing a functional delay line, essential to have the desired phase shifts at the beam combiner.

Chapter four transitioned to the mechanical realisation of the nulling interferometer. Mass estimation, CAD modelling realised using NX software and tolerance analysis ensured that the physical design could support the stringent optical requirements while remaining feasible in terms of deployment. The trade-offs between two different configurations, namely the telescopic and foldable secondary mirror ones, were examined and then compared with regard to compactness, stability and ease of alignment.

Finally, Chapter five introduced the compensator system designed to mitigate real-world perturbations and enhance interferometric performance. Two compensator strategies were implemented in CODE V: one utilising the bisection method and the other employing optimisations commands. Interferogram analyses under both single and multiple branch perturbations were then presented. The final statistical analysis including transmission maps, and detection yields showed that the interferometer, when optimized and compensated, can achieve levels of performance suitable for detecting terrestrial exoplanets.

While this work has addressed several key design challenges, certain limitations remain. Notably, real-time control systems, long-term thermal stability, and vibration isolation were not discussed and represent essential components for a functional space-based system.

Nonetheless, this thesis presents several contributions: a comprehensive design workflow combining optical and mechanical subsystems; a refined approach to compensator implementation; performance metrics that reflect realistic perturbation scenarios. These developments serve as a valuable reference for future work in the field.

Looking ahead, the results of this thesis can contribute to ongoing and future mission concepts. As humanity seeks to answer fundamental questions about the existence of life beyond our solar system, nulling interferometry remains one of the most promising techniques. With continued development and interdisciplinary effort it will further contribute to the direct detection and characterization of habitable, Earth-like worlds orbiting distant stars.

Chapter A

Overview of macro-PLUS programs in CODE V

A.1 Optical path

Below is the code used to retrieve the optical path written in the CODE V macro-PLUS language:

```
IN data_points49077
^el == 49077;
^data_string == " 'dddd.ddddddddd' 'dddd.dddddd' 'dddd.dddddd'"
OPE NEW U^file op.txt

FOR ^iter 1 ^el
    XDE ss (^COORD_X(^iter))
    YDE ss (^COORD_Y(^iter))
    ^opt_path(^iter) == (op R1 Ss..i Z1 W1)
    ^xdet(^iter) == (x r1 f1 si)
    ^ydet(^iter) == (y r1 f1 si)
    wri U^file Q^data_string ^opt_path(^iter) ^xdet(^iter) ^ydet(^iter)
END FOR

CLO U^file
XDE ss (0)
YDE ss (0)
```

Its purpose is to perform ray tracing at specific decentered input points and record the optical path length, as well as the detector coordinates, for each ray. This is done across a dataset of 49077 points (e.g., from a circular input grid), and the results are written to a file.

A set of input data points forming a circle having the same radius as the telescope aperture is previously generated in MATLAB and saved in the file `data_points49077.seq`. The file is then read to initialise the data points. Furthermore, `^data_string` defines the output formatting for each line in the result file.

A loop iterates over all the points:

- For each point, the X and Y coordinates are extracted.
- These values are used to set the system decentre (XDE, YDE).
- CODE V is then used to compute:
  - Optical Path (op)
  - X coordinate at the detector (x)
  - Y coordinate at the detector (y)
- Each set of values is saved to a text file.

A.2 Perturbations

Below is the code used to apply the perturbations to the system written in the CODE V macro-PLUS language:

```
in normal_distribution
^el == 50;
in NOMINAL_opt
^OP_target == @OpticalPath

FOR ^iter 1 ^el
    ^dec2 == 1e-4; ! cm
    ^dec3 == 1e-4; ! cm
    ^dec4 == 1e-4; ! cm
    ^tilt2 == 0.5e-4; ! deg
    ^tilt3 == 0.5e-4; ! deg
    ^tilt4 == 0.5e-4; ! deg

    THI so (1e20)
    THI Ss (315)
    THI S2 (-315 + ^var(@transf_number)*^dec2)
    THI S3 (350 + ^var(@transf_number)*^dec3)
    THI S4 (-50 + ^var(@transf_number)*^dec4)
    THI Si (0)

    RDY So (1e20)
    RDY Ss (1e20)
    RDY S2 (-600 + ^var(@transf_number)*^dec2)
    RDY S3 (30 + ^var(@transf_number)*^dec3)
    RDY S4 (1e20)
    RDY Si (1e20)

    XDE So (0)
    XDE Ss (0)
    XDE S2 (0 + ^var(@transf_number)*^dec2)
    XDE S3 (0 + ^var(@transf_number)*^dec3)
    XDE S4 (0 + ^var(@transf_number)*^dec4)
    XDE Si (0)

    YDE So (0)
    YDE Ss (0)
    YDE S2 (0 + ^var(@transf_number)*^dec2)
    YDE S3 (0 + ^var(@transf_number)*^dec3)
    YDE S4 (0 + ^var(@transf_number)*^dec4)
    YDE Si (-50)

    ZDE So (0)
    ZDE Ss (0)
    ZDE S2 (0 + ^var(@transf_number)*^dec2)
    ZDE S3 (0 + ^var(@transf_number)*^dec3)
    ZDE S4 (0 + ^var(@transf_number)*^dec4)
    ZDE Si (50)

    ADE So (0)
    ADE Ss (0)
    ADE S2 (0 + ^var(@transf_number)*^tilt2)
    ADE S3 (0 + ^var(@transf_number)*^tilt3)
    ADE S4 (45 + ^var(@transf_number)*^tilt4)
    ADE Si (90)

    BDE So (0)
    BDE Ss (0)
    BDE S2 (0 + ^var(@transf_number)*^tilt2)
```

```
    BDE S3 (0 + ^var(@transf_number)*^tilt3)
    BDE S4 (0 + ^var(@transf_number)*^tilt4)
    BDE Si (0)

    CDE So (0)
    CDE Ss (0)
    CDE S2 (0 + ^var(@transf_number)*^tilt2)
    CDE S3 (0 + ^var(@transf_number)*^tilt3)
    CDE S4 (0 + ^var(@transf_number)*^tilt4)
    CDE Si (0)

    in tolerwfe

    XDE ss (^COORD_X(1))
    YDE ss (^COORD_Y(1))

    in op_computation

    in NOMINAL_opt
    in nominalWF
END FOR
```

This macro-PLUS program automates a Monte Carlo-style tolerance analysis. It perturbs various optical parameters and logs the effect on a defined performance metric across multiple iterations.

A macro `normal_distribution.seq` is loaded, where the values of a normal distribution of 100000 values, with standard deviation equal to 0.3 and mean value equal to 0, has been obtained using a MATLAB script and then used to apply the tolerances to the system.

Then the number of iterations is defined, in this case the value is set to 50. A `for` loop is then implemented where several parameters of the optical system are modified based on a random perturbation via `^var(@transf_number)`. This function plays a specific role: it generates a pseudo-random integer between 1 and 100000, and returns that number as its output.

Parameters being perturbed:

- THI: Thickness

  Surfaces S2, S3, S4 thicknesses are perturbed from their nominal values.
- RDY: Y-radius of curvature

  Y-curvatures of S2, S3 are perturbed. Others are left as constants.
- XDE/YDE/ZDE: Decentering in space

  X/Y/Z positions for S2–S4 are perturbed, simulating misalignment.
- ADE/BDE/CDE: Tilt angles (alpha, beta, gamma)

  Angular perturbations applied to surfaces S2–S4.

Then, surface deformations are applied to the system with the macro `tolerwfe.seq`, resulting in a wavefront error. This macro-PLUS program simulates random wavefront errors (WFEs) using Zernike polynomials[33], and applies those deformations as surface phase errors on specified optical surfaces (S2, S3, and S4).

The optical path is then computed. Finally before restarting the cycle, the system is set to its nominal configuration, putting to zero all the perturbations previously applied.

A.3 Compensator

The macro-PLUS program implemented for the compensator has the same structure as the one for the perturbations. The only difference relays on the fact that in this case, after the perturbations are applied the macro where the compensator is implemented is added in a code line inside the `for` loop.

Below, the two macro-PLUS programs for the two different compensators, namely the one based on the bisection method and the one based on the CODE V optimisation, explained in Chapter 5.

A.3.1 Bisection method compensator

```
^delta1  == 0.01        ! initial step in degrees
^delta3  == 0.01        ! initial step in degrees
^delta2  == 0.001       ! initial step in cm
^delta4  == 0.001       ! initial step in cm
^tol     == 1e-5        ! stop when step is small
^maxIter == 1000

^step1    == ^delta1
^step2    == ^delta2
^step3    == ^delta3
^step4    == ^delta4
^dir1     == 1         ! +1 or \textendash 1
^dir2     == 1         ! +1 or \textendash 1
^dir3     == 1         ! +1 or \textendash 1
^dir4     == 1         ! +1 or \textendash 1
^iter     == 0

^ADE0    == (ADE S3)
^XDE0    == (XDE S3)
^BDE0    == (BDE S3)
^YDE0    == (YDE S3)
^CDE0    == (CDE S3)
^ZDE0    == (ZDE S3)

^OPD0    == @OpticalPath - ^OP_target

UNT
  ^iter == ^iter + 1

  ADE S3 ((ADE S3) + ^dir1*^step1)
  ^OPD1 == @OpticalPath - ^OP_target

  IF (^OPD1 < ^OPD0 AND ^step1 > ^tol)
    ! success: accept, keep direction
    ^ADE0 == (ADE S3)
    ^OPD0 == ^OPD1
  ELS
    ! failure: undo, reverse & halve step
    ADE S3 ((ADE S3) - ^dir1*^step1)
    ^dir1  == -^dir1
    ^step1 == ^step1 / 2
  END IF

  XDE S3 ((XDE S3) + ^dir2*^step2)
  ^OPD1 == @OpticalPath - ^OP_target

  IF (^OPD1 < ^OPD0 AND ^step2 > ^tol)
    ! success: accept, keep direction
    ^XDE0 == (XDE S3)
    ^OPD0 == ^OPD1
  ELS
    ! failure: undo, reverse & halve step
    XDE S3 ((XDE S3) - ^dir2*^step2)
    ^dir2  == -^dir2
    ^step2 == ^step2 / 2
  END IF
```

```
  BDE S3 ((BDE S3) + ^dir3*^step3)
  ^OPD1 == @OpticalPath - ^OP_target

  IF (^OPD1 < ^OPD0 AND ^step3 > ^tol)
    ! success: accept, keep direction
    ^BDE0 == (BDE S3)
    ^OPD0 == ^OPD1
  ELS
    ! failure: undo, reverse & halve step
    BDE S3 ((BDE S3) - ^dir3*^step3)
    ^dir3  == -^dir3
    ^step3 == ^step3 / 2
  END IF

  YDE S3 ((YDE S3) + ^dir4*^step4)
  ^OPD1 == @OpticalPath - ^OP_target

  IF (^OPD1 < ^OPD0 AND ^step4 > ^tol)
    ! success: accept, keep direction
    ^YDE0 == (YDE S3)
    ^OPD0 == ^OPD1
  ELS
    ! failure: undo, reverse & halve step
    YDE S3 ((YDE S3) - ^dir4*^step4)
    ^dir4  == -^dir4
    ^step4 == ^step4 / 2
  END IF

END UNT ((^step1 < ^tol AND ^step2 < ^tol AND ^step3 < ^tol AND ^step4 < ^
    tol) OR ^iter > ^maxIter)
```

Firstly, the initial steps, the tolerance and the maximum number of iterations are defined. Then, after the initialisations, the initial OPD error is computed.

The next step is the main optimisation loop, which runs until all the step are smaller than the previously defined `^tol` or `^iter` exceeds `^maxIter`. Within each iteration:

- the script adjusts each of the four parameters independentlyh and in sequence: ADE, XDE, BDE and YDE.
- for each:

  - apply step in current direction

  - evaluate new OPD (`^OPD1`)

  - compare to previous one (`^OPD0`)

  if improved (smaller) and the step is still bigger than `^tol`, then the change is accepted and the direction and the step are kept. Otherwise the step in undone, the direction is reversed and the step size is halved

A.3.2 CODE V optimisation compensator

```
frz sa

YDC S3 0
ZDC S3 0

ADC S3 0
BDC S3 0
CDC S3 100

^dec == 1e-4
^tilt == 1e-5
```

```
AFC Y

aut;
MXT 1
MNT 0.5
MNE 0.3
MNA 0.010000
MAE 0.000250

XDE S3 > ((XDE S3) - ^dec)
XDE S3 < ((XDE S3) + ^dec)

YDE S3 > ((YDE S3) - ^dec)
YDE S3 < ((YDE S3) + ^dec)

ZDE S3 > ((ZDE S3) - ^dec)
ZDE S3 < ((ZDE S3) + ^dec)

ADE S3 > ((ADE S3) - ^tilt)
ADE S3 < ((ADE S3) + ^tilt)

BDE S3 > ((BDE S3) - ^tilt)
BDE S3 < ((BDE S3) + ^tilt)

CDE S3 > ((CDE S3) - ^tilt)
CDE S3 < ((CDE S3) + ^tilt)

go

^micro == 1e-4
^nano == 1e-7
^pico == 1e-10

^deg == 1e-5

XDE S3 ((XDE S3) - (modf((XDE S3), ^nano)))
YDE S3 ((YDE S3) - (modf((YDE S3), ^nano)))
ZDE S3 ((ZDE S3) - (modf((ZDE S3), ^nano)))
ADE S3 ((ADE S3) - (modf((ADE S3), ^deg)))
BDE S3 ((BDE S3) - (modf((BDE S3), ^deg)))
CDE S3 ((CDE S3) - (modf((CDE S3), ^deg)))
```

The script automates an optimization process of the optical system, focusing on manipulating a specific surface (S3) to refine its alignment or positioning within a defined set of mechanical tolerances. Firstly, all the variables are freezed for every surface in the system. Then, the secondary mirror (S3) is granted of 6 degrees of freedom (DOFs) which are active variables in the optimisation cycle.

The actuators range are then defined both for the positional and angular resolution. The system is then set to afocal mode, resulting in a collimated output beams.

Mechanical limits are then imposed, in particular:

- MXT: Maximum center thickness.
- MNT: Minimum center thickness.
- MNE: Minimum edge thickness.
- MNA: Minimum axial air space.
- MAE: Minimum edge air space.

Minimum and maximum bounds on how much surface S3 can be moved or tilted during optimisation are defined, which ensures that changes stays within the defined actuator resolution.

Finally, the rounding precision level are established. The final values obtained from the optimisation process are rounded to the nearest multiple precision value, making the output mechanically realisable and ensuring actuator compatibility.

Bibliography

[1] Olivier Absil. 'Nulling Interferometry with IRSI-Darwin: Detection and Characterization of Earth-like Exoplanets'. 2001.

[2] Olivier Absil. 'Astrophysical studies of extrasolar planetary systems using infrared interferometric techniques'. PhD thesis. University of Liège, 2006. URL: `https://theses.hal.science/tel-00124720v1/file/Absil06_thesis.pdf`.

[3] Olivier Absil. 'Astrophysical studies of extrasolar planetary systems using infrared interferometric techniques'. In: ().

[4] J. R. P. Angel and N. J. Woolf. 'An Imaging Nulling Interferometer to Study Extrasolar Planets'. In: *The Astrophysical Journal* 475.1 (20th Jan. 1997), pp. 373–379. ISSN: 0004-637X, 1538-4357. DOI: `10.1086/303529`. URL: `https://iopscience.iop.org/article/10.1086/303529` (visited on 28/09/2024).

[5] *Ariane 6 user manual*. URL: `https://ariane.group/app/uploads/sites/4/2024/10/Mua-6_Issue-2_Revision-0_March-2021.pdf`.

[6] Antonin H. Bouchez et al. 'The Giant Magellan Telescope adaptive optics program'. In: SPIE Astronomical Telescopes + Instrumentation. Ed. by Enrico Marchetti, Laird M. Close and Jean-Pierre Véran. Montréal, Quebec, Canada, 21st July 2014, 91480W. DOI: `10.1117/12.2057613`. URL: `http://proceedings.spiedigitallibrary.org/proceeding.aspx?doi=10.1117/12.2057613` (visited on 07/02/2025).

[7] J. Bouwmeester et al. 'TN2- ESA nulling interferometry - Technology review and trade-off analysis'. In: 2024.

[8] M. M. Colavita et al. 'The Keck Interferometer'. In: *Publications of the Astronomical Society of the Pacific* 125.932 (Oct. 2013), pp. 1226–1264. ISSN: 00046280, 15383873. DOI: `10.1086/673475`. URL: `http://iopscience.iop.org/article/10.1086/673475` (visited on 12/03/2025).

[9] Consortium by TU Delft, KU Leuven and Centre Spatial de Liège. *TN2- ESA nulling interferometry - Technology review and trade-off analysis*. 2024.

[10] Luigi d'Arcio et al. 'Search for extraterrestrial planets: the DARWIN mission'. In: *International Conference on Space Optics — ICSO 2006*. International Conference on Space Optics 2006. Ed. by Errico Armandillo, Josiane Costeraste and Nikos Karafolas. Noordwijk, Netherlands: SPIE, 2006, p. 121. ISBN: 978-1-5106-1623-3 978-1-5106-1624-0. DOI: `10.1117/12.2308153`. URL: `https://www.spiedigitallibrary.org/conference-proceedings-of-spie/10567/2308153/Search-for-extraterrestrial-planets-the-DARWIN-mission/10.1117/12.2308153.full` (visited on 24/02/2025).

[11] W. C. Danchi et al. 'The Importance of Phase in Nulling Interferometry and a Three-Telescope Closure-Phase Nulling Interferometer Concept'. In: *The Astrophysical Journal* 645.2 (10th July 2006), pp. 1554–1559. ISSN: 0004-637X, 1538-4357. DOI: `10.1086/504511`. URL: `https://iopscience.iop.org/article/10.1086/504511` (visited on 23/02/2025).

[12] Colin Dandumont. 'Exoplanet detection yield with nulling interferometry'. PhD thesis. University of Liège.

[13] Colin Dandumont et al. 'Exoplanet detection yield of a space-based Bracewell interferometer from small to medium satellites'. In: *Journal of Astronomical Telescopes, Instruments, and Systems* 6.3 (23rd Sept. 2020). ISSN: 2329-4124. DOI: `10.1117/1.JATIS.6.3.035004`. URL: `https://www.spiedigitallibrary.org/journals/Journal-of-Astronomical-Telescopes-Instruments-and-Systems/volume-6/issue-03/035004/Exoplanet-detection-yield-of-a-space-based-Bracewell-interferometer-from/10.1117/1.JATIS.6.3.035004.full` (visited on 23/02/2025).

[14] Felix A. Dannert et al. 'Large Interferometer For Exoplanets (LIFE): II. Signal simulation, signal extraction, and fundamental exoplanet parameters from single-epoch observations'. In: *Astronomy & Astrophysics* 664 (Aug. 2022), A22. ISSN: 0004-6361, 1432-0746. DOI: `10.1051/0004-6361/202141958`. URL: `https://www.aanda.org/10.1051/0004-6361/202141958` (visited on 06/02/2025).

[15] D Defrere et al. 'Update on the LBTI: a versatile high-contrast and high-resolution infrared imager for a 23-m telescope'. In: *Haute Provence Observatory Colloquium*. 2013.

[16] D. Defrère et al. 'Nulling interferometry: performance comparison between space and ground-based sites for exozodiacal disc detection'. In: *Astronomy & Astrophysics* 490.1 (Oct. 2008), pp. 435–445. ISSN: 0004-6361, 1432-0746. DOI: `10.1051/0004-6361:200810248`. URL: `http://www.aanda.org/10.1051/0004-6361:200810248` (visited on 23/02/2025).

[17] Denis Defrère. 'Characterizing extrasolar planetary systems using infrared interferometry'. PhD thesis. University of Liège, 2009.

[18] Denis Defrère et al. 'L-band nulling interferometry at the VLTI with Asgard/NOTT: status and plans'. In: *Optical and Infrared Interferometry and Imaging IX*. Optical and Infrared Interferometry and Imaging IX. Ed. by Stephanie Sallum, Joel Sanchez-Bermudez and Jens Kammerer. Yokohama, Japan: SPIE, 28th Aug. 2024, p. 14. ISBN: 978-1-5106-7513-1 978-1-5106-7514-8. DOI: `10.1117/12.3019922`. URL: `https://www.spiedigitallibrary.org/conference-proceedings-of-spie/13095/3019922/L-band-nulling-interferometry-at-the-VLTI-with-Asgard-NOTT/10.1117/12.3019922.full` (visited on 12/03/2025).

[19] Frank Eisenhauer, John D. Monnier and Oliver Pfuhl. 'Advances in Optical/Infrared Interferometry'. In: *Annual Review of Astronomy and Astrophysics* 61.1 (18th Aug. 2023), pp. 237–285. ISSN: 0066-4146, 1545-4282. DOI: `10.1146/annurev-astro-121622-045019`. URL: `https://www.annualreviews.org/content/journals/10.1146/annurev-astro-121622-045019` (visited on 25/02/2025).

[20] cedrat technologies Esa. 'Actuators for Space Applications: State of the Art and New Technologies'. In: (2014).

[21] European Space Agency. *Darwin factsheet*. Science & Exploration. URL: `https://www.esa.int/Science_Exploration/Space_Science/Darwin_factsheet`.

[22] European Space Agency. *Exoplanets in the spotlight*. URL: `https://www.esa.int/Science_Exploration/Space_Science/Exoplanets/Exoplanets_in_the_spotlight`.

[23] *European Space Observatory (ESO). The Very Large Telescope Interferometer*. URL: `https://www.eso.org/sci/facilities/paranal/telescopes/vlti.html`.

[24] Europeans Southern Observqtory. *ELT Instruments: METIS*. URL: `https://elt.eso.org/instrument/METIS/` (visited on 12/03/2025).

[25] *Flexure-Guided OEM Piezo Actuator*. URL: `https://www.nanoactuators.com/Nano-Actuator_Datasheet/P601_Nano-Precision-Actuator.pdf`.

[26] Francesco De Bortoli. 'Development of an advanced modelling tool for a four apertures nulling interferometer'. Université de Liège, 2025.

[27] C V M Fridlund. 'Darwin – The Infrared Space Interferometry Mission'. In: (2000).

[28] C.V.M Fridlund. 'The Darwin mission'. In: *Advances in Space Research* 34.3 (Jan. 2004), pp. 613–617. ISSN: 02731177. DOI: `10.1016/j.asr.2003.05.031`. URL: `https://linkinghub.elsevier.com/retrieve/pii/S0273117703011955` (visited on 24/02/2025).

[29] Jonathan P. Gardner et al. 'The James Webb Space Telescope'. In: *Space Science Reviews* 123.4 (Apr. 2006), pp. 485–606. ISSN: 0038-6308, 1572-9672. DOI: `10.1007/s11214-006-8315-7`. URL: `https://link.springer.com/10.1007/s11214-006-8315-7` (visited on 07/02/2025).

[30] Germain Garreau et al. 'Asgard/NOTT: L-band nulling interferometry at the VLTI. II. Warm optical design and injection system'. In: *Journal of Astronomical Telescopes, Instruments, and Systems* 10.1 (15th Feb. 2024). ISSN: 2329-4124. DOI: `10.1117/1.JATIS.10.1.015002`. URL: `https://www.spiedigitallibrary.org/journals/Journal-of-Astronomical-Telescopes-Instruments-and-Systems/volume-10/issue-01/015002/Asgard-NOTT--L-band-nulling-interferometry-at-the-VLTI/10.1117/1.JATIS.10.1.015002.full` (visited on 12/03/2025).

[31] Adrian M. Glauser et al. 'The Large Interferometer For Exoplanets (LIFE): a space mission for mid-infrared nulling interferometry'. In: *Optical and Infrared Interferometry and Imaging IX*. Optical and Infrared Interferometry and Imaging IX. Ed. by Stephanie Sallum, Joel Sanchez-Bermudez and Jens Kammerer. Yokohama, Japan: SPIE, 28th Aug. 2024, p. 48. ISBN: 978-1-5106-7513-1 978-1-5106-7514-8. DOI: `10.1117/12.3019090`. URL: `https://www.spiedigitallibrary.org/conference-proceedings-of-spie/13095/3019090/The-Large-Interferometer-For-Exoplanets-LIFE--a-space-mission/10.1117/12.3019090.full` (visited on 25/02/2025).

[32] A. Glindemann et al. 'The VLTI — A Status Report'. In: *Astrophysics and Space Science* 286.1 (2003), pp. 35–44. ISSN: 0004640X. DOI: `10.1023/A:1026145709077`. URL: `http://link.springer.com/10.1023/A:1026145709077` (visited on 24/02/2025).

[33] Eugene Hecht. *Optics*. 5 edition. Global edition. Boston: Pearson Education, Inc, 2017. 1 p. ISBN: 978-0-13-397722-6 978-1-292-09696-4.

[34] P. M. Hinz et al. 'Overview of LBTI: a multipurpose facility for high spatial resolution observations'. In: SPIE Astronomical Telescopes + Instrumentation. Ed. by Fabien Malbet, Michelle J. Creech-Eakman and Peter G. Tuthill. Edinburgh, United Kingdom, 4th Aug. 2016, p. 990704. DOI: `10.1117/12.2233795`. URL: `http://proceedings.spiedigitallibrary.org/proceeding.aspx?doi=10.1117/12.2233795` (visited on 24/02/2025).

[35] Philip M. Hinz et al. 'Status of the LBT interferometer'. In: SPIE Astronomical Telescopes + Instrumentation. Marseille, France, 14th July 2008, p. 701328. DOI: `10.1117/12.790211`. URL: `http://proceedings.spiedigitallibrary.org/proceeding.aspx?doi=10.1117/12.790211` (visited on 24/02/2025).

[36] *James Webb Telescope*. URL: `https://science.nasa.gov/mission/webb/#SMSS`.

[37] Niels Christian Jessen, Hans Ulrik Nørgaard-Nielsen and Jørgen Schroll. 'CFRP lightweight structures for extremely large telescopes'. In: *Composite Structures* 82.2 (Jan. 2008), pp. 310–316. ISSN: 02638223. DOI: `10.1016/j.compstruct.2007.01.011`. URL: `https://linkinghub.elsevier.com/retrieve/pii/S0263822307000153` (visited on 16/05/2025).

[38] J. Kammerer, S. P. Quanz and E. Fontanet. 'P-pop user documentation'. In: *Astronomy & Astrophysics* (2021).

[39] Hannu Karttunen et al., eds. *Fundamental Astronomy*. Berlin, Heidelberg: Springer Berlin Heidelberg, 2017. ISBN: 978-3-662-53044-3 978-3-662-53045-0. DOI: `10.1007/978-3-662-53045-0`. URL: `http://link.springer.com/10.1007/978-3-662-53045-0` (visited on 06/02/2025).

[40] *Keck Telescope and Facility Instrument Guide*. URL: `https://www2.keck.hawaii.edu/observing/kecktelgde/ktelinstupdate.pdf`.

[41] P Kern et al. 'Single mode beam combination for interferometry'. In: *Bulletin de la Société Royale des Sciences de Liège* (2005).

[42] Hagyong Kihm and Yun-Woo Lee. 'Optimization and Tolerance Scheme for a Mirror Mount Design Based on Optomechanical Performance'. In: *Journal of the Korean Physical Society* 57.3 (15th Sept. 2010), pp. 440–445. ISSN: 0374-4884. DOI: `10.3938/jkps.57.440`. URL: `http://www.jkps.or.kr/journal/DOIx.php?id=10.3938/jkps.57.440` (visited on 08/04/2025).

[43] Chris Kitchin. *Exoplanets*. Astronomers' Universe. New York, NY: Springer New York, 2012. ISBN: 978-1-4614-0643-3 978-1-4614-0644-0. DOI: `10.1007/978-1-4614-0644-0`. URL: `http://link.springer.com/10.1007/978-1-4614-0644-0` (visited on 06/02/2025).

[44] Chris Kitchin. *Exoplanets. Finding, Exploring, and Understaning Alien Wordlds*. Springer, 2012.

[45] B. S. Konrad et al. 'Large Interferometer For Exoplanets (LIFE): III. Spectral resolution, wavelength range, and sensitivity requirements based on atmospheric retrieval analyses of an exo-Earth'. In: *Astronomy & Astrophysics* 664 (Aug. 2022), A23. ISSN: 0004-6361, 1432-0746. DOI: `10.1051/0004-6361/202141964`. URL: `https://www.aanda.org/10.1051/0004-6361/202141964` (visited on 12/03/2025).

[46] Stefan Kraus. 'Infrared Spectro-Interferometry of Massive Stars: Disks, Winds, Outflows, and Stellar Multiplicity'. PhD thesis. 2007.

[47] L. Labadie et al. 'Modal filtering for nulling interferometry: First single-mode conductive waveguides in the mid-infrared'. In: *Astronomy & Astrophysics* 450.3 (May 2006), pp. 1265–1266. ISSN: 0004-6361, 1432-0746. DOI: `10.1051/0004-6361:20053407`. URL: `http://www.aanda.org/10.1051/0004-6361:20053407` (visited on 06/03/2025).

[48] *Latest Data from NASA's Exoplanet Archive*. URL: `https://science.nasa.gov/exoplanets/discoveries-dashboar`.

[49] Romain Laugier, Nick Cvetojevic and Frantz Martinache. 'Kernel nullers for an arbitrary number of apertures'. In: *Astronomy & Astrophysics* 642 (Oct. 2020), A202. ISSN: 0004-6361, 1432-0746. DOI: `10.1051/0004-6361/202038866`. arXiv: `2008.07920[astro-ph]`. URL: `http://arxiv.org/abs/2008.07920` (visited on 23/02/2025).

[50] P R Lawson et al. 'Terrestrial Planet Finder Interferometer (TPF-I)'. In: (31st Mar. 2009).

[51] Peter R. Lawson. *Principles of Long Baseline Stellar Interferometry.*

[52] Oliver P Lay. 'Systematic errors in nulling interferometers'. In: *Optical Society of America* (2004).

[53] Oliver P Lay. 'Imaging properties of rotating nulling interferometers'. In: *Optical Society of America* (2005).

[54] A. Léger and T. Herbst. 'Darwin - Science Across Disciplines - A Proposal for the Cosmic Vision 2015-2025 ESA Plan'. In: (). URL: `https://arxiv.org/pdf/0707.3385`.

[55] S. Loiseau and S. Shaklan. 'Optical design, modelling and tolerancing of a Fizeau interferometerdedicated to astrometry'. In: *Astronomy and Astrophysics Supplement Series* 117.1 (May 1996), pp. 167–178. ISSN: 0365-0138, 1286-4846. DOI: `10.1051/aas:1996148`. URL: `http://aas.aanda.org/10.1051/aas:1996148` (visited on 08/04/2025).

[56] C. Lovis et al. 'Atmospheric characterization of Proxima b by coupling the SPHERE high-contrast imager to the ESPRESSO spectrograph'. In: *Astronomy & Astrophysics* 599 (Mar. 2017), A16. ISSN: 0004-6361, 1432-0746. DOI: `10.1051/0004-6361/201629682`. URL: `http://www.aanda.org/10.1051/0004-6361/201629682` (visited on 12/03/2025).

[57] Lucas Viseur. 'Development of a performance modeling tool for nulling interferometry'. Université de Liège, 2024.

[58] Frantz Martinache and Michael J. Ireland. 'Kernel-nulling for a robust direct interferometric detection of extrasolar planets'. In: *Astronomy & Astrophysics* 619 (Nov. 2018), A87. ISSN: 0004-6361, 1432-0746. DOI: `10.1051/0004-6361/201832847`. URL: `https://www.aanda.org/10.1051/0004-6361/201832847` (visited on 23/02/2025).

[59] John W. Mason. *Exoplanets. Detection, Formation, Porperties, Habitability.* Springer, 2008.

[60] *MEETOPTICS, Optical Delay lines.* URL: `https://www.meetoptics.com/academy/optical-delay`.

[61] Bertrand Mennesson and Jean Marie Mariotti. 'Array Configurations for a Space Infrared Nulling Interferometer Dedicated to the Search for Earthlike Extrasolar Planets'. In: *Icarus* 128.1 (July 1997), pp. 202–212. ISSN: 00191035. DOI: `10.1006/icar.1997.5731`. URL: `https://linkinghub.elsevier.com/retrieve/pii/S0019103597957316` (visited on 06/02/2025).

[62] Meyor and Queloz. 'A Jupiter-mass companion to a solar-type star'. In: *Nature* (1995).

[63] *Miniature Motorized Actuators - Nanometer-Precision Actuators: Piezoelectric and Motorized Linear Motion for Nanometer Accuracy Applications.* URL: `https://www.nanoactuators.com/nano-actuator.php`.

[64] *NASA. Keck Telescope.* URL: `https://en.wikipedia.org/wiki/W._M._Keck_Observatory#/media/File:Kecknasa.jpg`.

[65] *NASA. The Large Binocular Telescope Interferometer.* URL: `https://assets.science.nasa.gov/dynamicimage/assets/science/astro/exo-explore/2023/09/lbti20150120-16.png?w=1600&h=900&fit=clip&crop=faces%2Cfocalpoint`.

[66] Jerry Nelson and Gary H. Sanders. 'The status of the Thirty Meter Telescope project'. In: SPIE Astronomical Telescopes + Instrumentation. Ed. by Larry M. Stepp and Roberto Gilmozzi. Marseille, France, 27th Aug. 2008, 70121A. DOI: `10.1117/12.788238`. URL: `http://proceedings.spiedigitallibrary.org/proceeding.aspx?doi=10.1117/12.788238` (visited on 07/02/2025).

[67] *P-753 LISA Linear Actuator and Stage*. URL: https://www.nanoactuators.com/Nano-Actuator_Datasheet/P753_Nano-Precision-Actuator.pdf.

[68] P. R. Lawson, O. P. Lay and alia. 'Terrestrial Planet Finder Interferometer (TPF-I) Whitepaper for the AAAC Exoplanet Task Force'. In: (2nd Apr. 2007).

[69] Michael Perryman. *The Exoplanet handbook*. Cambridge, 2011.

[70] G. L. Pilbratt et al. '*Herschel* Space Observatory: An ESA facility for far-infrared and submillimetre astronomy'. In: *Astronomy and Astrophysics* 518 (July 2010), p. L1. ISSN: 0004-6361, 1432-0746. DOI: 10.1051/0004-6361/201014759. URL: http://www.aanda.org/10.1051/0004-6361/201014759 (visited on 07/02/2025).

[71] S. P. Quanz et al. 'Large Interferometer For Exoplanets (LIFE): I. Improved exoplanet detection yield estimates for a large mid-infrared space-interferometer mission'. In: *Astronomy & Astrophysics* 664 (Aug. 2022), A21. ISSN: 0004-6361, 1432-0746. DOI: 10.1051/0004-6361/202140366. URL: https://www.aanda.org/10.1051/0004-6361/202140366 (visited on 05/02/2025).

[72] Emanuele Alberto Slejko. 'A demisability analysis based on materials properties for space telescope mirrors'. In: *Journal of Space Safety Engineering* 10.2 (June 2023), pp. 208–216. ISSN: 24688967. DOI: 10.1016/j.jsse.2023.03.005. URL: https://linkinghub.elsevier.com/retrieve/pii/S2468896723000319 (visited on 16/05/2025).

[73] Keto Soosaar. 'DESIGN OF OPTICAL MIRROR STRUCTURES'. In: *A Division of Massachusetts Institute of Technology* (1971).

[74] *The Astrometry method*. URL: https://www.planetary.org/articles/wobbly-stars-the-astrometry-method.

[75] J.Y. Tien et al. 'Formation acquisition sensor for the terrestrial planet finder (TPF) mission'. In: *2004 IEEE Aerospace Conference Proceedings (IEEE Cat. No.04TH8720)*. 2004 IEEE Aerospace Conference Proceedings (IEEE Cat. No.04TH8720). Vol. 4. Big Sky, MT, USA: IEEE, 2004, pp. 2680–2690. ISBN: 978-0-7803-8155-1. DOI: 10.1109/AERO.2004.1368063. URL: http://ieeexplore.ieee.org/document/1368063/ (visited on 25/02/2025).

[76] John T. Trauger and Wesley A. Traub. 'A laboratory demonstration of the capability to image an Earth-like extrasolar planet'. In: *Nature* 446.7137 (Apr. 2007), pp. 771–773. ISSN: 0028-0836, 1476-4687. DOI: 10.1038/nature05729. URL: https://www.nature.com/articles/nature05729 (visited on 07/02/2025).

[77] L Viseur. 'Master thesis and internship[BR]- Master's thesis : Development of a performance modeling tool for nulling interferometry[BR]- Internship'. MA thesis. Université de Liège, 2024.

[78] Brent Ware and Curt Henry. 'Modeling the TPF interferometer'. In: SPIE Astronomical Telescopes + Instrumentation. Ed. by Simon C. Craig and Martin J. Cullum. USA, 16th Sept. 2004, p. 193. DOI: 10.1117/12.550265. URL: http://proceedings.spiedigitallibrary.org/proceeding.aspx?doi=10.1117/12.550265 (visited on 25/02/2025).

[79] M W Werner et al. 'The Spitzer space telescope mission'. In: (2004).

[80] James R. Wertz and Wiley J. Larson, eds. *Space mission analysis and design: SMAD III*. 3. ed., 10. print. Space technology library 8. Hawthorne, Calif: Microcosm Press [u.a.], 2008. 976 pp. ISBN: 978-1-881883-10-4 978-0-7923-5901-2.

[81] Xiaobin Zhang et al. 'Optical compensation for the perturbed three mirror anastigmatic telescope based on nodal aberration theory'. In: *Optics Express* 25.11 (29th May 2017), p. 12867. ISSN: 1094-4087. DOI: `10.1364/OE.25.012867`. URL: `https://opg.optica.org/abstract.cfm?URI=oe-25-11-12867` (visited on 09/05/2025).